Experiments on the Thermal, Electrical, and Plasmonic Properties of Nanostructured Materials

Kirby B. Myers

Dissertation submitted to the Faculty of the

Virginia Polytechnic Institute and State University

in partial fulfillment of the requirements for the degree of

Doctor of Philosophy

in

Physics

Hans D. Robinson, Chair

James R. Heflin

Nahum Arav

Levon V. Asryan

April 26, 2018

Blacksburg, Virginia

Keywords: Thermoelectrics, Thermoreflectance, Thermal Rectification, Plasmonics, Thin films, Nanospheres

Experiments on the Thermal, Electrical, and Plasmonic Properties of Nanostructured Materials

Kirby B. Myers

(ABSTRACT)

Nanofabrication techniques continue to advance and are rapidly becoming the primary route to enhancement for the electrical, thermal, and optical properties of materials. The work presented in this dissertation details fabrication and characterization techniques of thin films and nanoparticles for these purposes. The four primary areas of research presented here are thermoelectric enhancement through nanostructured thin films, an alternative frequency-domain thermoreflectance method for thin film thermal conductivity measurement, thermal rectification in nanodendritic porous silicon, and plasmonic enhancement in silver nanospheroids as a reverse photolithography technique.

Nanostructured thermoelectrics have been proposed to greatly increase thermopower efficiency and to bring thermoelectrics to mainstream power generation and cooling applications. In our work, thermoelectric thin films of SbTe, BiTe, and PbTe grown by atomic layer deposition and electrochemical atomic layer deposition were characterized for enhanced performance over corresponding bulk materials. Seebeck coefficient measurements were performed at temperatures ranging from 77 K to 380 K. Atomic composition was verified by energy-dispersive X-ray spectroscopy and structures were imaged by scanning electron microscopy. All thin films measured were ultimately found to have a comparable or smaller Seebeck coefficient to corresponding materials made by conventional techniques, likely due to issues with the growth process.

Frequency-domain thermoreflectance offers a minimally invasive optical pump-probe technique for measuring thermal conductivity. Like time-domain thermoreflectance, the version of frequency-domain thermoreflectance demonstrated here relies on a non-zero thermo-optic coefficient in the sample, but uses moderate cost continuous wave lasers modulated at kHz or MHz frequencies rather than a more expensive ultrafast laser system. The longer timescales of these frequency ranges enables this technique to take measurements of films with thicknesses ranging from 100 nm to 10 μm, complimentary to time-domain thermoreflectance. This method differentiates itself

from other frequency-domain methods in that it is also capable of simultaneous independent measurements of both the in plane and out of plane values of the thermal conductivity in anisotropic samples through relative reflective magnitude, rather than phase, measurements. We validated this alternate technique by measuring the thermal conductivity of Al_2O_3 and soda-lime and found agreement both with literature values and with separate measurements obtained with a conventional time-domain thermoreflectance setup.

Thermal rectification has the potential to enhance microcircuit performance, improve thermoelectric efficiency, and enable the creation of thermal logic circuits. Passive thermal rectification has been proposed to occur in geometrically asymmetric nanostructures when heat conduction is dominated by ballistic phonons. Here, nanodendritic structures with branch widths of $\approx$ 10 nm and lengths of $\approx$ 20 nm connected to $\approx$ 50 μm long trunks were electrochemically etched from $<111>$ silicon wafers. Thermal rectification measurements were performed at temperatures ranging from 80 K to 250 K by symmetric thermal conductivity measurements. No thermal rectification was ultimately found in these samples within the margin of thermal conductivity measurement error 1%. This result is consistent with another study which found thermal rectification with greater conduction in the direction opposite to what ballistic phonon heat conduction theories predicted.

Plasmonic resonance concentrates incident photon energy and enables channeling of that energy into sub-wavelength volumes where it can be used for nanoscale applications. We demonstrated that surface plasmon polaritons induced in silver nanosphereoid films by 532 nm light defunctionalize previously photocleaved ligands adsorbed onto the films, to yield a reverse photolithographic technique. In this method, gold nanosphere conjugation were conjugated to a photocleaved ligand, however conjugation could be inhibited by exposing the cleaved ligand to 532 nm light and consequently yield a reversal technique. This defunctionalizion effect did not occur on gold films or nanoparticles conjugated with the ligand in IR spectroscopy, and was observed to have a reduced

effect in silver films relative to silver nanospheroid film. As silver nanospheroid films and gold nanospheres of the size used in this study are known to have plasmon resonance in the green wavelengths, while gold and silver continuous films do not, this defunctionalization likely results from plasmonic effects.

Experiments on the Thermal, Electrical, and Plasmonic Properties of Nanostructured Materials

Kirby B. Myers

(GENERAL AUDIENCE ABSTRACT)

The increasing trend toward smaller and more efficient electronic devices requires continuous refinement of manufacturing and materials technology. From communication devices to temperature management, miniaturization in electronic components allows for greater versatility in applications. In battery powered devices, increasing efficiency both extends operational lifetime and reduces operational costs in terms of kilowatt hours as well as carbon footprint resulting from powering the devices. Through the application of miniaturization, conventional fabrication techniques are rapidly approaching the physical limits of their applicability, and newer techniques must be developed. Nanofabrication methods involve working with materials at scales where quantum mechanical effects can dominate over classical effects. Some examples of these effects are unique heat and electrical conduction properties in, effectively, one or two dimensional materials as in the case of quantum dots or thin films. This size regime not only allows for construction at smaller scales, but also enables the manipulation of quantum mechanical effects to produce different types of devices which were not possible to make previously. For example, materials can be built up one atomic layer at a time, enabling the creation of a material with perfect atomic ordering, as opposed to common methods which yield many imperfections. This dissertation details fabrication and characterization techniques of nanoscale devices focusing on thermoelectrics, thin film thermal conductivity, thermal rectification, and plasmonic enhancement.

Thermoelectrics are devices that use temperature differences across the device to produce electric power or, conversely, create a temperature difference across the device when electrically driven. Theoretical studies have proposed that the efficiency of thermoelectric materials can be greatly increased through nanofabrication. Here, thin film thermoelectric devices made from commonly employed bulk materials such as SbTe, BiTe, and PbTe produced by atomic layer deposition and electrochemical atomic layer deposition, were characterized to test these theories. Ultimately, no notable enhancement was found in our samples over conventionally produced materials, but this may have been due to difficulties in the fabrication process of the thin films.

Thermoreflectance is a purely optical technique for thermal conductivity (the measure of how well a material conducts heat) measurement which can measure thin film materials. Other benefits of the technique are its speed and that samples measured by it are not damaged, unlike other methods which effectively ruin the sample for any purpose beyond the measurement. Cost, however, is a major downside to conventional thermoreflectance, as it requires pricey ultrafast laser systems. Presented here is an alternative method of thermoreflectance which used much more economical diode lasers to achieve thermal conductivity measurements. This system costs approximately a tenth of what a conventional system would, while also being capable of measuring in-plane and cross-plane thermal conductivity simultaneously. The drawbacks of this method are thicker film requirements and the necessity of having well-defined control samples of similar thermal conductivity to the sample of interest.

Management of waste heat is one of the major design limitations in modern circuitry. Removal of waste heat is most often performed by adhering large surface area heat sinks to heat generating areas and/or mechanical fans to aid in heat radiation. One proposed method of reducing the amount of space required for heat management is through the development and implementation of thermal rectifiers, which are materials that conduct heat more efficiently in one direction than the opposite. The thermal rectification properties of nanodendritic porous silicon is explored here. This material is made by electrochemically etching silicon wafers such that the surface is formed into an array of pine-tree-like structures on the nanoscale. While it was proposed that these structures would manifest thermal rectification under the right conditions, no rectification was observed. This result is consistent with previous experimental work which observed preferential heat conduction in the opposite direction to that proposed by this theory, likely caused by a different effect.

Plasmonic enhancement enables absorption and manipulation of light energy in structures far

smaller than conventional techniques permit. In the case of photolithography, a go-to method of commercial microfabrication, the smallest feature size is a function of the wavelength of light used and is typically around 100 nm. Plasmonic techniques enable optical manipulation in structures of sizes down to a few nm. The plasmonic enhancement technique demonstrated here is a photolithography technique in which selective nanosphere-to-nanosphere binding occurs This technique offers another method of directed self-assembly, where nanoparticles can come together to form larger structures. A benefit of this method is that large quantities of nanoparticle assemblies can occur simultaneously, allowing for rapid production of assembled nanostructures.

Contents

List of Figures

List of Tables

Chapter 1

Introduction

1.1 Thermoelectrics

The work presented in this dissertation cover a seemingly disparate set of topics in condensed matter physics but ultimately stem from two topics: heat conduction in nanostructured materials and plasmonic enhancement in nanoparticles. The primary impetus for all of the thermal property studies presented here was either direct contribution to or complementation of thermoelectric enhancement through nanostructuring. The Seebeck measurements of thin films was performed to directly address thermoelectric enhancement, the kHz frequency-domain thermoreflectance system was originally designed to measure the thermal conductivity of thermoelectric films which were to be coated on macroporous silicon, and the thermal rectification of dendritic silicon was proposed to see application in heat guidance to increase the efficiency of thermoelectric devices. Note that the thermoreflectance work is currently in review by the International Journal of Thermophysics under the title of "Measuring thermal conductivity with magnitude-dependent frequency-domain thermoreflectance using modulated CW lasers." Also, some of the thermal rectification works presented here have been published in the 2014 MRS Fall Meeting Proceedings under the title of

”Thermal rectification of porous semiconductor materials.”

Power generation is an ever-present issue in today’s society, prompting an ongoing and seemingly endless drive in research for ever more efficient, economical, and eco-friendly means of power production. Among the lesser publicized modes of power production is the field of thermoelectrics which, as the name implies, involves the direct conversion of thermal energy to electrical potential energy. While far from new, thermoelectrics have remained relatively niche in application due to low efficiency, high cost of development inhibiting large scale usage, as well as the lack of applications where the necessarily high temperature differences are present. These limitations, however, allow thermoelectrics to shine in some applications where other technologies fall short. These include small power and limited volume applications and, most famously, in space probes. Another application of thermoelectric devices is heat removal, again on small scales as exemplified by electronic component cooling [27], where thermoelectrics eliminate the need for large fluid handling compression or evaporation systems. Although usually not thought of this way, thermocouples are devices which employ the thermoelectric effect to measure temperature. Indeed, the most alluring prospect of thermoelectrics is the duality of direct and mechanically simple manipulation of heat flow by electronics and, conversely, power generation by heat flow [129].

The physical concept that is at the core of all thermoelectrics is known as the Thermoelectric Effect and is a unification of two previously discovered effects, the Seebeck Effect and the Peltier Effect. First discovered by Thomas Seebeck in the early 1820’s [119], the Seebeck Effect described the generation of a magnetic field by two dissimilar joined metals heated to different temperatures. This magnetic field was later determined to result from an induced current in the metals. The magnitude of the voltage produced was proportional to the temperature difference across the junction, and this material constant of proportionality became known as the Seebeck coefficient. The Peltier Effect was later discovered in the 1830’s [98] by Jean Peltier who found that when current was applied to joined dissimilar metals, heat transport occurred at the junction. In 1851, William

Thomson, who later became known as Lord Kelvin, unified the Peltier and Seebeck effects with a relationship that also predicted a third effect, that would become known as the Thomson effect [128]. This effect describes the heating or cooling of a homogeneous material when supplied with current and a temperature gradient across the material. The cause of the Seebeck effect is charge carrier diffusion within a heat flow. Charge carriers within these materials also carry heat, so when temperature gradients form across the material, so does an electric potential. The Seebeck coefficient is consequently defined by the change in electrochemical potential (μ) with respect to temperature per unit charge:

$$\alpha = \frac{1}{\mathrm{e}} \frac{\partial_{\mathrm{x}} \mu}{\partial \mathrm{T}}. \tag{1.1}$$

Following the work of Thomson, interest in thermoelectric power generation and cooling grew greatly. In 1909 and 1911, Altenkirch published studies involving the theoretical limits to efficiency in thermoelectric power [2] and cooling [3], which showed that an ideal thermoelectric material should have a maximal Seebeck coefficient (α) and electrical conductivity (σ) while having a minimal thermal conductivity (κ). In the 1950's, Ioffe [49, 50] formalized this notion and developed a metric of the quality (the figure of merit Z) of a thermoelectric material still in use today. Due to the temperature dependence of all of the thermoelectric properties of materials, a dimensionless figure of merit is commonly used, where the figure of merit is multiplied by the absolute temperature of the material:

$$\mathrm{ZT} = \frac{\alpha^2 \sigma \mathrm{T}}{\kappa}. \tag{1.2}$$

In order for thermoelectric cooling to be economically viable for common applications, the efficiency of the entire device must surpass that of alternative cooling methods such as the ubiquitous

vapor compressor methods. The efficiency of thermoelectric devices is primarily dependent upon ZT, but the thermoelectric properties of any material will also be dependent upon the temperature difference across the material as well as the average temperature at which it operates. As thermoelectric devices are, fundamentally, a variety of heat engines, their efficiency is ultimately limited by Carnot efficiency ($\Delta T/T_h$) however in the instance of a thermoelectric device [123] the efficiency is

$$\eta = \left(\frac{\Delta T}{T_h}\right)\left(\frac{\sqrt{1+ZT}-1}{\sqrt{1+ZT}+\frac{T_c}{T_h}}\right). \tag{1.3}$$

Here, ZT is the figure of merit of the device rather than a single base material, ΔT is the temperature difference across the device, and T_h and T_c are the hot and cold side temperatures respectively. In the case of room temperature applications, an economically competitive thermoelectric device requires a ZT above 3 [36]. To achieve this, thermoelectric devices are nearly universally designed in packages consisting of pairs of thermoelectric materials with charge carriers of opposite sign connected electrically in series and thermally in parallel. These configurations are made from n-type and p-type materials, with for negative and positive charge carriers respectively, and are illustrated in Figure 1.1.

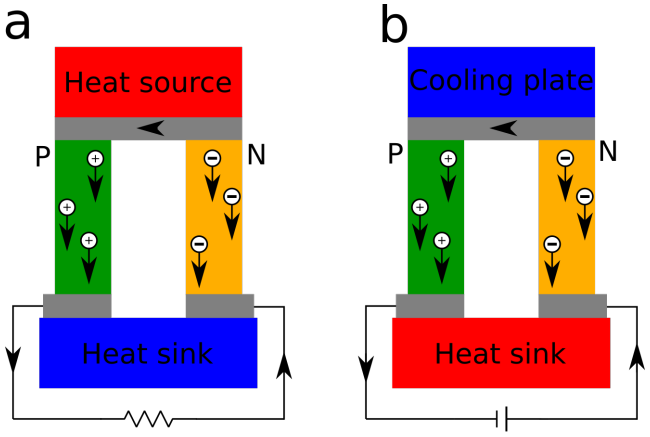

Figure 1.1: Base elements used in thermoelectric devices for (**a**) power generation and (**b**) cooling

A complete thermoelectric package consists of many of such base elements connected electrically in series and thermally in parallel, sandwiched between plates that are both electrically insulating and thermally conductive and are often a ceramic material.

Finding materials with maximal ZT around room temperature is the ultimate goal of much thermoelectric research, as such materials could have efficiencies high enough to make thermoelectric cooling an economical alternative to the current fluid compression systems which are much bulkier and prone to mechanical wear and breakdown. Other temperature regimes are also heavily investigated, as high temperature thermoelectrics have the greatest power yield while low temperature thermoelectrics are of particular interest to works involving cryogenics and space probes.

Prior to Ioffe's work in the 1950's, metals were most commonly researched for use as thermoelectric materials. Unfortunately, around room temperature most metals have Seebeck coefficients of $\approx 10\ \frac{\mu V}{K}$ leading to efficiencies less than 1% [12]. Most bulk thermoelectric materials used commercially today are made from semiconductor alloys and have a ZT$\approx$1 which corresponds to around 10% heat energy conversion efficiency at room temperature [99]. A plot of the figure of merit of a few commonly studied thermoelectric semiconductor materials is shown in Figure 1.2 (republished with permission of Taylor and Francis Group LLC Books, from The CRC Handbook of Thermoelectrics, David Rowe, 1994; permission conveyed through Copyright Clearance Center, Inc. [28]). More recent works, beginning in the 1990's, have seen great interest in nanostructured materials for use as thermoelectrics due to the promise of tunability of thermoelectric parameters by material growth processes. These studies, detailed in the following chapter, were the foundation of and impetus behind the thermoelectric studies of this dissertation.

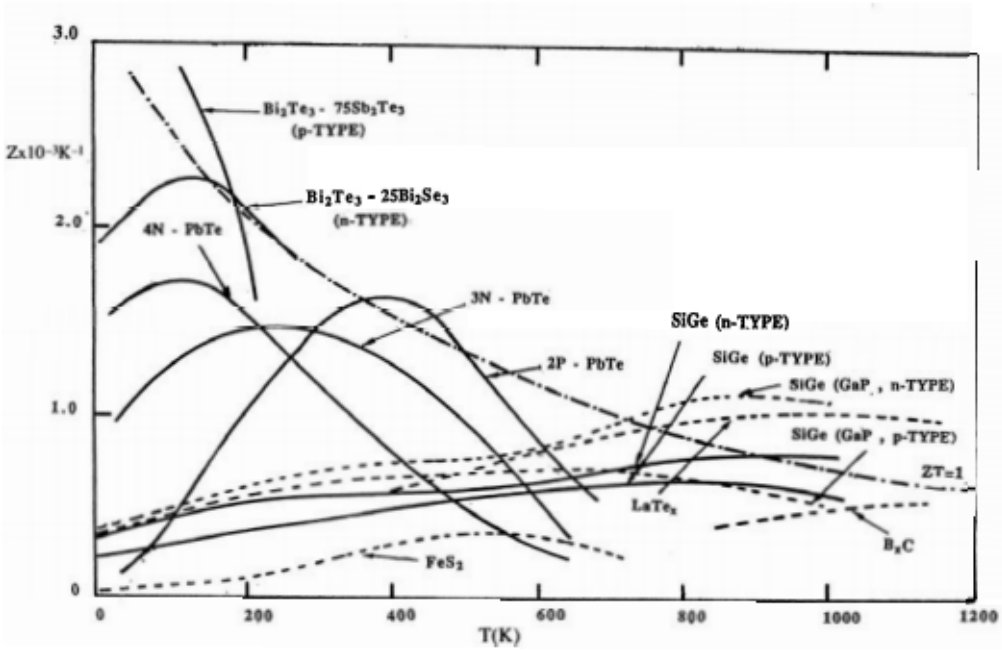

Figure 1.2: Figure of merit of selected bulk semiconductor thermoelectric materials.

1.2 Thermal Conduction

Reducing heat conduction while maintaining high electrical conduction has been one of the greatest challenges in the field of thermoelectrics. Heat conduction in solid materials is governed by charge carriers and phonons. Consequently, thermal conductivity is often represented as $\kappa = \kappa_{\mathrm{e}} + \kappa_{\mathrm{p}}$ where κ_{e} and κ_{p} are electronic and phononic thermal conductivity components. Charge carriers, such as electrons and holes, are highly mobile particles and consequently often dominate heat conduction in electrically conductive materials. Phonons, on the other hand, are quasiparticles representative of collective lattice vibrations. In the case of metals, thermal conductivity due to charge carriers and electrical conductivity are proportional to each other as stated by the Wiedemann-Franz law

$$\frac{\kappa}{\sigma} = \mathrm{LT}, \qquad \mathrm{L} = 244 \quad \frac{\mu\mathrm{W}\Omega}{\mathrm{K}}. \tag{1.4}$$

Due to this relationship, early work on thermoelectric optimization in metals involved finding metals with a maximal Seebeck coefficient in order to yield the greatest efficiency. The Wiedemann-Franz law has also been widely used to estimate the electronic thermal conductivity component of a material from electrical conductivity measurements [58], which are typically much easier to carry out. Though Equation (1.4) holds true for many metals over a wide temperature range, the theory does break down under certain conditions. Some high purity metals have exhibited temperature dependence in L [40], and semiconductors exhibit L dependence on several factors such as density of states and superlattice layer thickness [85]. Reduced dimensional nanostructures have also shown large divergence from the theory [64].

The foundation of generalized thermal conduction theory dates back to Fourier's ground breaking work in 1822 [34] and is Fourier's law, shown in Equation (1.5):

$$\vec{\mathrm{q}} = -\kappa\nabla\mathrm{T}. \tag{1.5}$$

Here $\vec{\mathrm{q}}$ is the heat flux density, κ is the thermal conductivity, and $\nabla\mathrm{T}$ is the temperature gradient across a material. Though it is an empirical law, Fourier's law is the basis of classical heat conduction theory and is valid for equilibrium heating in materials of constant thermal conductivity. The earliest and still most common method of thermal conductivity measurement, in bulk materials, is through the direct application of Equation (1.5) in a 1-dimensional form. In this case, constant heat is applied to one surface a material and the resultant, stabilized, temperature difference across the material is measured in order to calculate its thermal conductivity. The implementation of this technique is simple in principle, however maintaining equilibrium heating and accurately mea-

suring temperature becomes increasingly difficult with smaller sample dimensions, particularly so when approaching the nanoscale. Further, this law breaks down when heat conduction is not the result of mass heat carrier thermalization, such as in the case of certain reduced dimensional structures where individual heat carrier trajectories must be considered [20]. The fundamental principle of this technique was applied in the thermal rectification studies of this dissertation, where a lattice of nanostructures over tens of microns can be expected to exhibit an effective bulk thermal conductivity.

In order to measure heat conduction in individual reduced dimensional structures where Fourier's law is still applicable, transient heating techniques are commonly employed. For non-equilibrium heating, the time-dependent temperature field throughout a heated material can be derived from Fourier's law and is known as the heat equation

$$\frac{\delta \mathrm{u}}{\delta \mathrm{t}} - \frac{\kappa}{\mathrm{c_p}\rho}\nabla^2 \mathrm{u} = 0. \tag{1.6}$$

Here u is the temperature field, κ is the thermal conductivity, $\mathrm{c_p}$ is the specific heat capacity, and ρ is the material density. The fraction $\frac{\kappa}{\mathrm{c_p}\rho}$ is commonly known as the thermal diffusivity and is a measure material's time dependent temperature change. The primary benefit in application of the heat equation over Fourier's law is that the heat equation enables measurements of dynamic systems which are much easier to establish, experimentally, than systems in equilibrium. This enables transient measurement techniques which readily measure thin film thermal properties such as the 3Ω method [14, 72], time domain thermoreflectance [16, 17, 18], frequency domain thermoreflectance [117, 141], as well as the alternative the frequency domain thermoreflectance method demonstrated in this dissertation.

1.3 Plasmonics

Plasmons are the collective oscillations of free electrons in conducting materials which result from stimulation by light under appropriate conditions. These excitations can form in bulk materials (as three-dimensional bulk plasmons), on surfaces (as two-dimensional surface plasmon polaritons [SPP]), as well as on nanostructures (as zero-dimensional localized surface plasmons [LSP]). While a more detailed theoretical foundation of these types of plasmons is detailed in the final chapter, some key points are as follows. Bulk plasmons can be excited in a material only at a single frequency known as the plasmon frequency, ω_{p} defined by

$$\omega_{\mathrm{p}} = \sqrt{\frac{\mathrm{n_e e^2}}{\varepsilon_0 \mathrm{m}^*}}. \tag{1.7}$$

Here, $\mathrm{n_e}$ is the electron number density, e is the electron charge, ε_0 is the vacuum permittivity, and m^* is the effective electron mass. A cartoon depicting bulk plasmon excitation is shown in Figure 1.3.

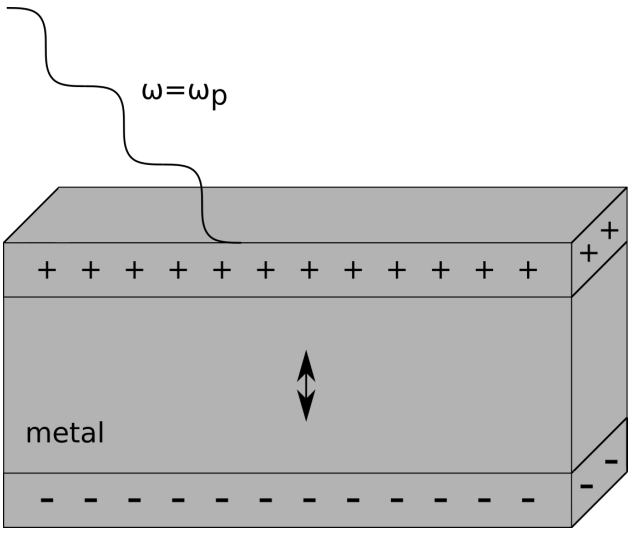

Figure 1.3: Depiction of bulk plasmon excitation.

SPPs can be excited only when the incident light's momentum is adjusted, such as by a diffraction grating or prism coupling, and propagate along the metal/dielectric interface. The SPP excitation conditions are dependent on the method of momentum adjustment, though they still are a function of metal's bulk plasmon frequency. A cartoon depicting SPP excitation is shown in Figure 1.4.

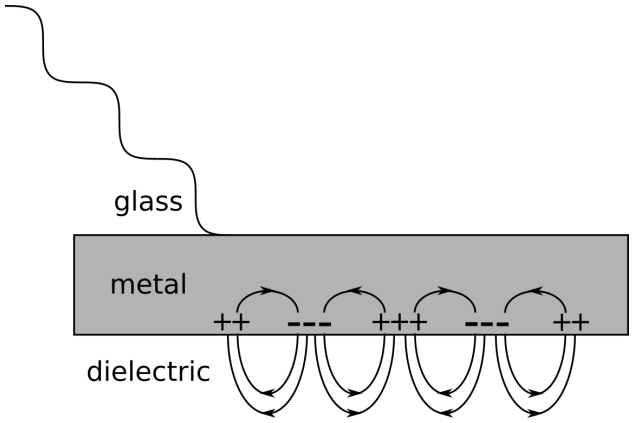

Figure 1.4: Depiction of surface plasmon excitation.

LSPs can be excited by a range of wavelengths and most commonly manifest on metallic nanoparticles such as nanospheres. In order for LSPs to occur, the nanostructure size must be much smaller than the wavelength of excitation light. Further, the metal nanosphere's complex, frequency dependent, permittivity (ε_1) and the dielectric nanosphere medium's permittivity (ε_2) must be balanced such that $\varepsilon_1 + 2\varepsilon_2$ is minimized. A cartoon depicting LSP excitation is shown in Figure 1.5.

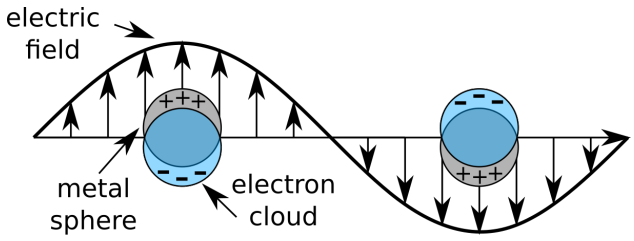

Figure 1.5: Depiction of localized surface plasmon excitation.

While the excitation conditions of bulk and SPP are quite limited, the relative ease of nanosphere plasmon excitation resulted in their commercial use, though not understanding, since antiquity.

Perhaps the most famous example of this is the Lycurgus cup, a 4th century Roman stained glass cup, in which gold and silver nanoparticles absorb some visible wavelengths, via LSP resonance, which results in a bright red color of light transmitted through the glass. Other grandiose stained glass works, popularized in medieval churches, also employed metallic nanoparticles to produce many vibrant colors.

Modern plasmon theory began in the early 1900's with what has become called "Wood's anomalies." Woods observed that when polarized light reflected off of metal diffraction gratings at certain angles of incidence, unexpected dark bands formed in the resultant spectra [137]. It was not until the 1950's that this effect was attributed to plasma oscillations in a groundbreaking work by Pines and Bohm [100]. Following the bloom of plasmonics research in the 1950's and 1960's, new plasmonic applications were developed.

The applications of plasmonics are many and varied. Surface-enhanced Raman spectroscopy [32] (SERS) is a plasmonic technique which improves upon conventional Raman spectroscopy [62, 105]. In Raman spectroscopy, inelastic scattering of monochromatic light results in a shift in photon energy, which can then be used to determine the presence of a particular molecule or bond by yielding information on particular vibrational modes in the system. Surface plasmon resonance intensifies the absorbed light and consequently increases vibrational mode excitation rates, resulting in a larger observable signal. A major limitation of Raman spectroscopy is that the very low inelastic scattering rate, relative to the elastic scattering rate, makes it difficult to observe the former and limits the sensitivity of the system. SERS employs SPPs to greatly enhance the sensitivity of the measurement by adsorbing the molecules of interest to a rough or nanostructured metal surface which is then excited to produce SPPs. As the SPPs occur on surfaces in contact with the molecules, the Raman scattering modes of the molecules occur at a greater rate enabling much greater sensitivity and allowing for detection of single molecules [59, 89].

Another application of plasmonics is in photovoltaic devices. One limiting factor in most com-

monly used photovoltaic devices is the low absorbance of near-bandgap light, and one way to mitigate this is would be to increase the effective optical path length inside the cell around that region. Three methods of interest have shown promise [4] in doing so; using nanospheres to enable preferential scattering directions in the absorbing layer [115], using LSP resonance with nanoparticles at near-bandgap wavelengths to increase absorbtivity [106], and using SPP grating couplers to couple the light into SPP modes that propagate in plane with the absorbance layer [31]. Another benefit to implementation of plasmonics in these examples is that the total volume of the absorbance layer can be reduced without reducing absorbing efficiency, which, in principle, makes the photovoltaic devices require fewer resources to produce and could drive down cost.

The ever-increasing demand for smaller and faster electronics presents another opportunity for plamonic applications. Information transport rates through conventional electronics is currently being limited substantially by metallic interconnects, often copper wires, as they are limited by electron transfer rates through the material. Optical interconnects are able to transfer data much faster, using instead the speed of light in the interconnect medium, but require much larger physical components in order to couple to electronics than in the metallic interconnect case [95]. Devices such as plasmonic waveguides [74], couplers [88], as well as modulators [83] show promise in the development of subwavelength light control in plasmonic circuitry.

In this dissertation, the plasmonic enhancement is demonstrated to inhibit nanosphere adsorption onto previously photocleaved ligands, enabling reverse lithographic patterning of nanospheres. While the plasmonic enhancement studies detailed in this work have no direct relation to the field of thermoelectrics, they were driven as a natural extension of some of the methods developed for the thermoelectric studies. Many of the electrochemistry principles involved in nanodendritic silicon etching were carried over to nanoparticle synthesis, and the reverse lithography system used in nanosphere photopatterning was made by modifying the frequency-domain thermoreflectance system. The effect which prevents nanosphere conjugation to the photocleaved ligand was observed

by happenstance by See [118]. The exploration of this effect, and its potential applications, led to the plasmonic studies presented here.

Chapter 2

Thermoelectric Characterization of Thin Film Multilayer Structures

2.1 Thermoelectric Effect Optimization

The primary goal of thermoelectrics (TE) research is to produce devices with maximal TE efficiency. In order to do so for any given operating temperatures, one must find a material with a maximal figure of merit. Staying true to Equation (1.2), one must consequently maximize the Seebeck coefficient α as well as the electrical conductivity σ while minimizing the thermal conductivity κ. Such a materials are often referred to as being a phonon-glass electron crystal structures. A central problem of designing such a material arises from the interdependence of α, σ, and κ. In this chapter, Sections 2.1 and 2.2 are background review while Sections 2.3 and 2.4 present the novel work of this study.

The kinetic definition of α is the energy difference between the average energy of mobile carriers and the Fermi energy [99]. If the carrier concentration in a material is increased, the Fermi en-

ergy, average carrier energy, and consequently the electrical conductivity will also increase. The downside to this method is that increasing carrier concentration will increase the Fermi energy at a greater rate than it will the average carrier energy [1] which consequently decreases α and has a net effect of ultimately reducing ZT. The thermal conductivity (κ) used in the figure of merit equation (1.2) is often expressed as the sum of two thermal conductive processes, charge carrier thermal conduction (κ_e) and lattice phonon thermal conduction (κ_p). Attempts at increasing σ, such as increasing carrier concentration, will also increase κ_e as is shown in the Wiedemann-Franz Law (1.4) in the case of metals, however analogous effects occur in other materials as well, which limits increases to ZT.

These issues seem to indicate that the only parameter which is not interdependent in the figure of merit equation is κ_p, however even lattice phonon thermal conductivity is not wholly independent. One commonly applied method to increasing κ_p is to introduce defects into the lattice to scatter phonons, but this also effectively reduces charge carrier mobility and electrical conductivity [99]. Skutterudite [91] and clathrate [90] materials, which have cage-like unit cells that can be filled with ions intersitially, are actively researched as they offer a means of separating σ and κ. In such materials, heat carrying phonons are scattered by the vibrations of the ions trapped within the unit cells of the material while the crystalline structure permits relatively high electrical conductivity. These materials have been found to have ZT values approaching unity at elevated temperatures [91] (>600 K) and consequently are of particular interest for high temperature applications.

In the early 90's theoretical work led primarily by Dresselhaus [45] [44] [47] showed the potential for high figure of merit materials made of composites consisting of reduced dimensional structures. Central to this concept is high electrical conductivity thin films of typically 1 nm thickness or less, in which the phonon's mean free path is greater than the film thickness which inhibits thermal transport. This process is discussed in depth in the Thermal Rectification Studies of Etched Silicon Nanostructures chapter, Chapter 4, below. A bulk device made from thin film multilayers

could then yield high TE enhancement. An example construction of such a device would involve stacking layers of a high conductivity material and a wide cap semiconductor, then connecting the ends of high conductivity layers together. This method effectively confines electron transport to the 2D high conduction planes and avoids 3D phonon scattering. Dresselhaus' theoretical work, along with early experimental confirmation of TE enhancement materials with reduced dimensional structures [46] ushered in a wave of research into reduced dimensional TE structures [70].

Though much theoretical work has been done on thin film thermoelectrics, relatively little experimental work has followed in recent years. Substantial difficulties in synthesis of high quality thin film thermoelectics on a scale capable of yielding macro scale effects has been a limiting factor and has driven much work on to other nanostructured materials such as nanocomposite bulk materials [29]. The primary motivation of nanostructuring in thermoelectrics is to weaken the correlation between electrical and thermal conductivity, this topic is further discussed in Section 2.2. Two related methods which are capable, in principle, of producing desirable TE thin films are atomic layer deposition (ALD) and electrochemical atomic layer deposition (eALD).

ALD works via self-limiting deposition of gaseous chemicals. The operating principle is that a gaseous compound (or precursor) is deposited onto the substrate until all available binding sites are filled, such that a monolayer of the compound is left on the surface. Next, the excess gas is purged, typically with an inert gas. Then a different reactive gas is deposited onto the previous layer, also in a self-limiting manner, followed by another purge. The process is repeated until the desired number of layers is achieved. An example of an ALD cycle is shown schematically in Figure 2.1.

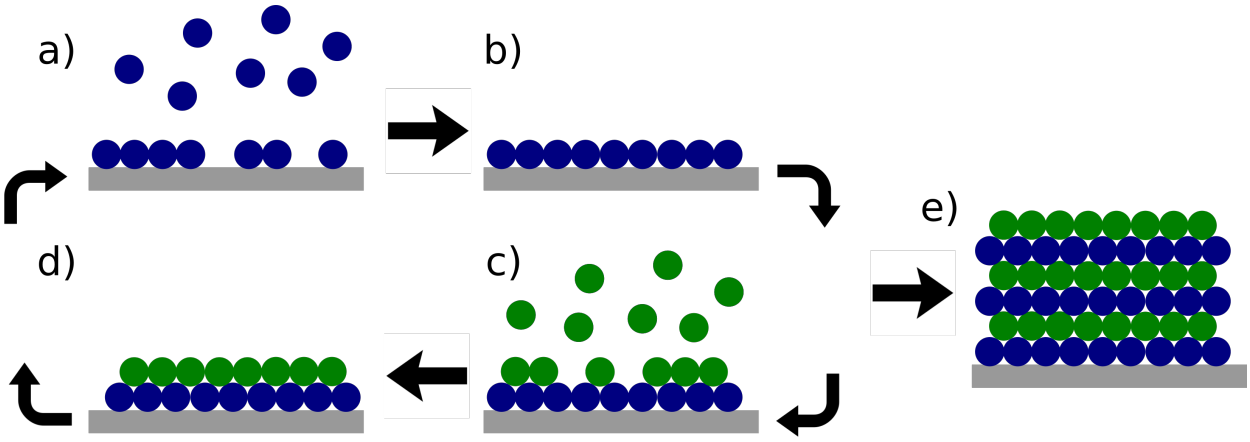

Figure 2.1: Atomic layer deposition (ALD). a) Deposition of first precursor. b) Purge of precursor after deposition, c) Deposition of second precursor. d) purge of second precursor after deposition. e) Repetition of a-d yields a material of desired thickness.

One of the great advantages of ALD over other methods, such as MOCVD, is that due to the self-limiting nature of the deposition and the separation of the reactive constituents forming the layer, conformal deposition over almost any surface topography can be achieved. Another benefit is highly precise thickness control, at the level of a fraction of a monolayer. A comprehensive review of the ALD technique was made by Steven George [38]. The uniformity and thickness control qualities of ALD have made it a prime candidate for use in thin film thermoelectrics where the film thickness needs to be smaller than the phonon mean free path.

A related method also capable, in principle, of achieving this result is electrochemical atomic layer deposition (eALD). eALD operates on the same self limiting deposition cycle idea as ALD, but eALD uses chemicals in liquid form, rather than gas, and drives the reaction with an external bias voltage. A commonly employed method in eALD is under potential deposition, in which the external bias voltage is set such that it is insufficient to allow bulk growth of the precursor solution while still promoting binding with the surface, resulting in monolayer deposition [41]. The primary advantage of eALD over ALD is that, due to eALD taking place in a liquid phase, the temperature at which deposition occurs is typically much lower than in ALD [126]. One common issue with

eALD, however, is precursor contamination. Cleanly and reliably removing all of the previous precursor prior to the following precursor deposition stage is difficult due to the liquid phase, but not insurmountable. Schematically, eALD is very similar to the ALD process of Figure 2.1, with the primary difference being that the constituents of each layer have opposing charge sign and the sign of electrial bias switches correspondingly between layder growth steps.

Relatively few works have been performed in (e)ALD grown thermoelectrics [140] [131] making it an exciting area for cutting-edge research. Creating a complete TE device via monolayer growth is a very time consuming and resource intensive effort in the lab, so it is not feasible to produce complete devices for each iteration of the research refinement process. Instead, thin films consisting of 100's of monolayers are much more reasonable to produce for characterization. This necessitates characterization technologies which can perform Seebeck coefficient, thermal conductivity, and electrical conductivity measurements at the temperature regimes of interest on thin film samples. In the work presented here, thin films grown on silicon wafers were produced by our collaborators at MicroXact and characterized.

2.2 Thermoelectric Materials

To optimize TE efficiency, materials with high electrical conductivity, low thermal conductivity, and high Seebeck coefficient at the intended temperature range of operation must be used. Semiconductor and metal alloys have been the most commonly produced high ZT materials since the 1950's (see Figure 1.2), primarily consisting of various compound combinations consisting of Bi, Te, Pb, Sb, Si, Ge, Ga, and Ag. The various alloy combinations yield a sizable range of tunability of TE properties, though common characteristics of these materials include heavy atoms, which lowers thermal conductivity, and a relatively large effective mass at the Fermi level, which increases the Seebeck coefficient. The primary limitations of the alloying approach however is

charge carrier scattering at grain boundaries and high phonon conduction [132].

Thin film nanostructuring of thermoelectic materials enables the potential of phonon heat conduction attenuation through carrier mismatching in superlattices, while maintaining high electrical conductivity. A superlattice structure consists of a periodic order two or more periodic substructures. Through controlled growth of superlattice structures, the grain boundary effects which limit alloy techniques can be mitigated.

The materials studied in this work were superlattices consisting of thin films multilayers of commonly employed bulk semiconductor and metal compounds. The specific materials studied here were PbSe, PbTe, Sb_2Te_3, and Bi_2,Te_3 superlattices grown by ALD or eALD on Si, Ge, or Al_2O_3 substrates. In these materials, thin films of each constituent element were deposited in sequence, i.e. a PbSe sample consisted of stacked layers of Pb and Se. As all TE material properties are temperature dependent, different materials will have different ZT values in different temperature regimes. The materials we studied had maximal ZT values in cryogenic ($\approx 70\ \mathrm{K}$) to room temperature ($\approx 300\ \mathrm{K}$).

One issue with the principle of this method is commercial viability. Growing superlattices one atomic layer at a time is a very time intensive process, particularly when the thicknesses desired for commercial are on the order of 100's of microns at the smallest. To circumvent this issue, the final aim of the research was to develop high ZT thin films which could then be grown on macroporous silicon. Silicon with square well pores were to have the thin films grown on the walls until the wells were filled, resulting in materials of wafer thicknesses with most of the volume consisting of thin film thermoelectrics.

2.3 Seebeck Coefficient Characterization Methods

In order for a Seebeck measurement to be successful, heat flow must be carefully controlled over a wide range of temperatures. To do this we used a cryostat system which enabled us to perform the measurements in vacuum and, through the usage of resistive heating elements, direct heat flow for measurements ranging from 77 K - 380 K. The basic premise of Seebeck coefficient measurement is simple, establish a temperature gradient across the sample and measure the resultant voltage difference. In practice, however, several complications inherent to thin films make this process substantially more complicated. One such complication stems from asymmetry inherent to the films.

Heat and electron conduction in the superlatice structures are anisotropic due to uniform multilayer structuring and reduced dimensionality. Two measurement configurations were designed and implemented to quantify the differences between cross-plane and in-plane Seebeck coefficients and they are illustrated in Figure 2.2.

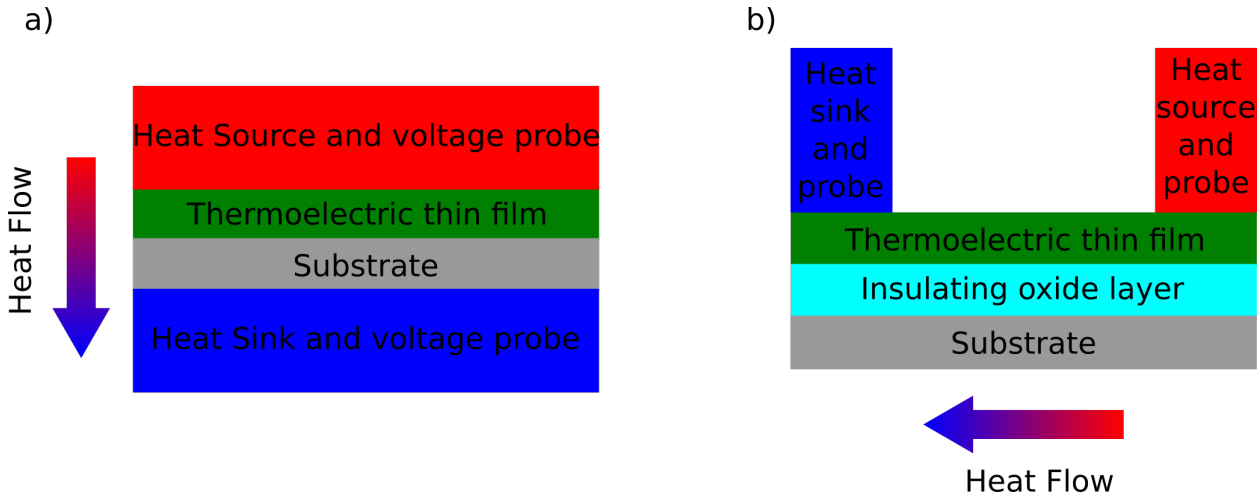

Figure 2.2: Seebeck measurement configurations. a) cross-plane configuration. b) in-plane configuration.

Special consideration must be given to the substrates on which the thin films are grown as they are,

more often than not, semiconductor materials. This presents an additional difficulty in measuring the Seebeck coefficient of the film alone due to the ease of electron flow between film and substrate. In the case of cross-plane measurements, the films were grown directly onto conducting substrates of known Seebeck coefficients that were accounted for in post analysis as detailed later in Equation (2.1). In-plane measurements were able to be taken directly when the films were grown on an electrically insulating oxide layer, as the oxide effectively electrically isolates the film from the substrate. Cross-plane measurements could not benefit from the oxide isolation method as the establishment of reliable electrical contact on the underside of the thin film without going through the substrate proved difficult.

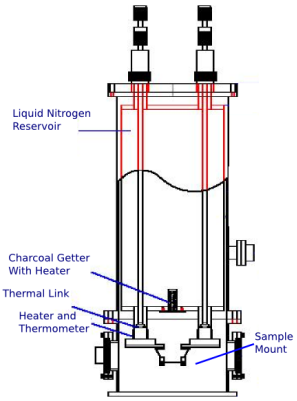

(a) Cryostat

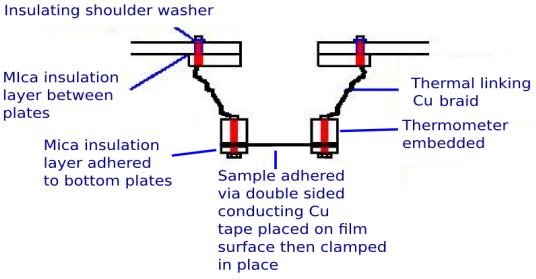

(b) In-plane mount

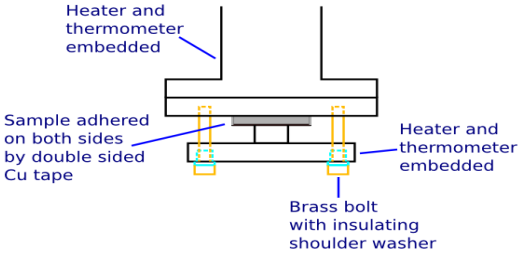

(c) Cross-plane mount

Figure 2.3: Seebeck coefficient measurement system

The experimental implementation of these principles introduced additional complications in heat

and electrical management for both of the measurement configurations. It was critical to maintain optimal thermal and electrical contact to the sample for reliable Seebeck effect measurement and, consequently, several sample adhesion methods were tested. Double-sided Copper tape was ultimately chosen for providing thermal and electrical contact due to its ability to form a strong connection which lasted through several vacuum and cooling cycles. The cryostat had two cold heads to which the sample mounts were attached. Each cold head also contained a resistive heater element which was used to establish the baseline operating temperature of the Seebeck measurement. To prevent the Seebeck voltages inherently formed across the cryostat walls and the two cold heads from interfering with the sample measurement, mica was used along with insulating shoulder washers to insulate the sample mount pieces from the cryostat as shown in Figure 2.3. A single grounding line connected one of the sample mount pieces and the cryostat to prevent the sample from electrically floating. Photographs of the system in the two measurement configurations are shown in Figure 2.4.

In the in-plane configuration, samples were cleaved into a rectangular shape, $\approx$ 15 mm by 25 mm, and the film side of the samples were adhered by copper tape to the heater/probe blocks. Once the sample was adhered, two screws on each block were carefully tightened to clamp the sample in place without crushing it (see Figure 2.3(b)). Thermometers were mounted into both of the mount pieces with thermal grease and voltage probe lines were soldered to the pieces. Tinned copper braids were used to connect the sample mount pieces to the cryostat post mounting pieces. This allowed added flexibility which prevented thermal strains from breaking connections to the sample over heating cycles.

(a) Cryostat

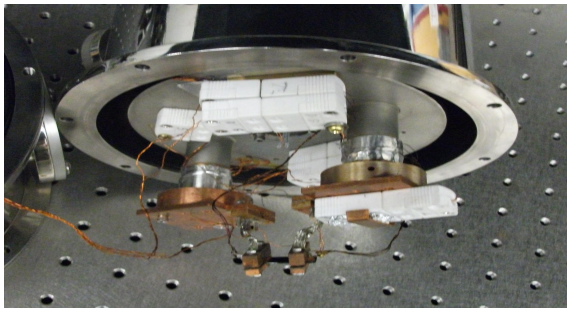

(b) In-plane configuration

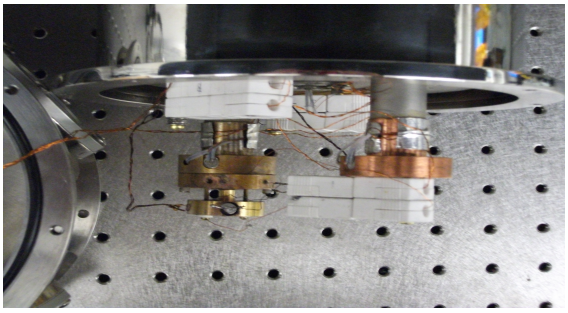

(c) Cross-plane configuration

Figure 2.4: Seebeck coefficient measurement configurations

The cross-plane measurement configuration, shown in Figure 2.3(c), involved adhering the sample directly to a cryostat post and a sample mount piece via double sided copper tape. Heaters and thermometers were located in both the cryostat post and the sample mount piece. The sample mount piece, itself, was then bolted to the cryostat post with insulating shoulder washers to thermally and electrically insulate the sample mount piece from the cryostat. The sinusoidal heating

method described below was used in this configuration as well.

To extract the Seebeck coefficient of the film when performing a cross-plane measurement, the film thickness and thermal conductivity must be known and the substrate thickness, thermal conductivity, and Seebeck coefficient must also be taken into consideration in the following way:

$$\begin{aligned} \alpha_{\mathrm{f}} &= \frac{1}{\kappa_{\mathrm{s}} - \kappa}[\alpha_{\mathrm{m}}(\kappa_{\mathrm{s}} - \kappa_{\mathrm{f}}) - \alpha_{\mathrm{s}}(\kappa - \kappa_{\mathrm{f}})], \\ \kappa &= \mathrm{x}\left(\frac{\mathrm{x_f}}{\kappa_{\mathrm{f}}} + \frac{\mathrm{x_s}}{\kappa_{\mathrm{s}}}\right)^{-1}. \end{aligned} \tag{2.1}$$

Here α_{f}, α_{m}, and α_{s} are the film, measured, and substrate Seebeck coefficients respectively; $\mathrm{x_f}$, $\mathrm{x_s}$, and x are the film, substrate, and film-substrate system thicknesses respectively; κ_{f} and κ_{s} are the film and substrate thermal conductivities respectively. Note that this assumes negligible thermal resistance at the film-substrate junction.

Initial Seebeck measurement attempts involved using the heaters to form a static thermal gradient across the sample and then record the measured voltage of the stabilized system. This, however, proved to be a rather difficult means of measurement as the sample temperatures would take an exceedingly long amount of time to stabilize and thermal drifting, caused by the gradual warming of the cryostat, often obfuscated such measurements. Temperature measurements during dynamic heating gradients, however, lag behind the true sample temperature during heating/cooling periods due to the heat capacity of the sample/mount system. Consequently, voltage measurements could not be directly correlated with temperature measurements in non-equilibrium conditions. Ultimately, the method settled upon involved driving either a single heater sinusoidally with constant heat output or both heaters sinusoidally with an 180° phase between them. This caused periodicity in the thermal gradient and consequent voltage. An example of the sinusoidal heating method is illustrated in Figure 2.5.

By periodically heating either side of the sample, voltage measurements swept out a curve in which

the temperature difference across the sample was repeatably varied despite temperature drifting of the system as a whole. While the Seebeck effect is certainly dependent upon temperature, if the total temperature drift of the sample is kept relatively small over the course of the measurement then such effects on the measurement are minimized to negligibility. Temperature drift over the course of a single Seebeck measurement was often around 1 to 5 K. To extract the Seebeck coefficient measurement from this cyclic heating method, the measured voltage is plotted against the temperature difference across the sample and the resulting ellipse is linearly fit with the slope of the fit being the Seebeck coefficient. The semi-minor axis of this ellipse is representative of the lag between temperature measurements and true sample sample temperatures, with larger sample heat capacities leading to larger semi-minor axes.

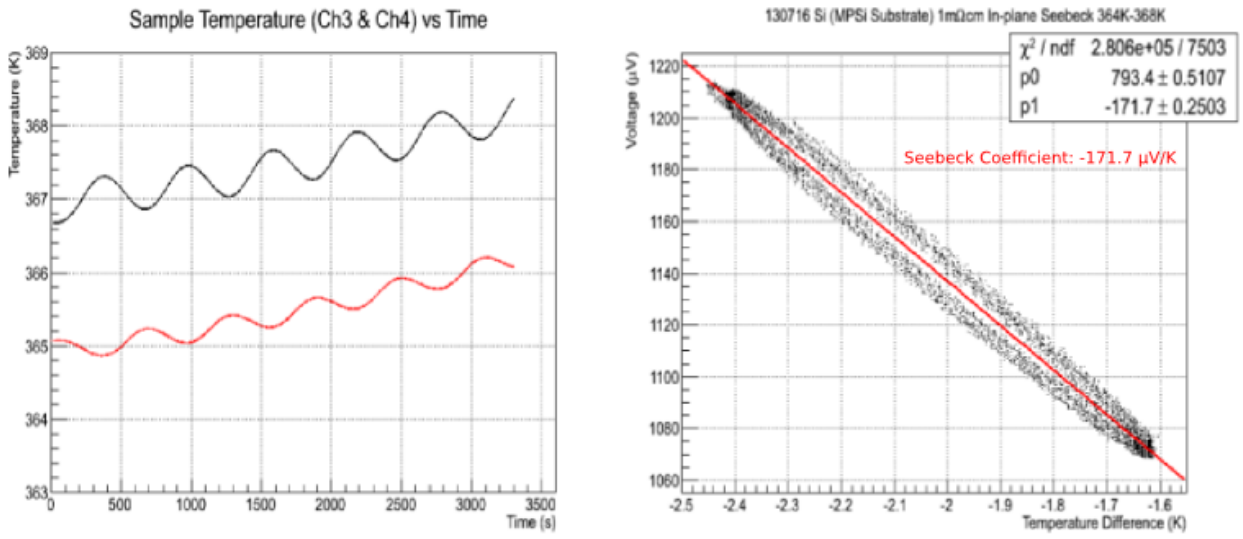

Figure 2.5: Sinusoid heating method of an in-plane Seebeck measurement

Heater control, temperature measurements, and voltage measurements were all managed by a Labview program for both the cross-plane and in-plane configurations. The final control program version used was PhoenixMK18.vi, which can be found along with this dissertation in the Virginia Tech ETD database.

Establishment of a baseline sample temperature about which sinusoidal heating would oscillate

was done by a proportional-integral (PI) controller subroutine. PI controllers are based on a feedback loop mechanism and are often used control systems which require continuous modulation. More commonly used are proportional-integral-derivative routines but as this system had a very slow response, the derivative component was not crucial and would require additional tuning to incorporate. Though many books have been written solely to describe PI and PID methods, it can be briefly described mathematically by

$$\mathrm{u(t)} = \mathrm{Pe(t)} + \mathrm{I}\int_0^{\mathrm{t}} \mathrm{e(t')dt'}. \tag{2.2}$$

Here $\mathrm{u(t)}$ is the time dependent control variable which is sent back into the system to correct for deviation from the setpoint, which is calculated from the error signal, i.e. $\mathrm{e(t)}$, the difference between the setpoint and the actual value. In the case of the temperature control scheme used here, $\mathrm{u(t)}$ is the voltage setting of the power supplies which drove the resistive heaters. P is the proportional factor which adjusts the output of the controller in linear response to the error and I is the integral factor which integrates over the history of the error and drive down the residual error caused by the proportional adjustments. Both P and I are constant values which depend on the system configuration as well as the thermal properties of the sample and are determined through heuristic methods such as the Ziegler-Nichols tuning method. Ultimately, fine tuning the values was done manually and is something of an art. Over several tuning trials, $\mathrm{P} = 10$ and $\mathrm{I} = 0.2$ were found to yield acceptably quick temperature control for samples with thermal properties like silicon when used in both in-plane and cross-plane configurations with 50 Ω heaters.

Prior to taking a Seebeck measurement, the sample was brought to the desired average temperature with the PI controller. After the sample was installed, the chamber was pumped down to $\approx$ 10 μTorr and then liquid nitrogen was added to cool the system. While still cooling but near the desired operating temperature, the PI controller was engaged. Once the sample temperature stabi-

lized at the setpoint, the Seebeck measurement cycle could begin by disengaging the PI controller and starting the sinusoidal heating controller.

The sinusoidal heating mode was controlled programically by setting power supply oscillation amplitude voltage, mean voltage, and oscillation period for either one or both of the sample heaters. The mean voltage setting was set to match the voltage which the PI controller found to stabilize at the desired setpoint, while optimal oscillation amplitude voltage and period varied somewhat from sample to sample and depending on average sample temperature. Typical oscillation amplitudes were around 2 V and oscillation periods were around 600 s for both in-plane and cross-plane configurations.

2.4 Seebeck Measurement Results

Over the course of the work fifty Seebeck measurement runs were taken over dozens of samples. The Seebeck measurement system and method was refined continuously throughout the work and was used as a diagnostic tool in the development of the ALD and eALD growth techniques of TE thin film superlattices. Ultimately, the growth techniques were never perfected and problems in developing cohesive superlattices persisted.

The original goal of the synthesis efforts was to produce superlattices of variable constituent layer thickness consisting of high quality TE materials. For example, a PbTe/PbSe superlattice with layers consisting of PbTe and PbSe thin films was intended to be developed by eALD. The primary benefit being that through the implementation of ALD and/or eALD, controlled atomic monolayer growth would greatly reduce the grain boundary and other defect effects that limit TE efficiency in bulk alloy methods. Over the course of the study however, difficulties in the synthesis process prevented reliable growth of even non-superlattice thin films, such as PbSe, and consequently superlattice structuring efforts also failed in all cases. Though well ordered superlattice struc-

tures were never produced, TE enhancement over bulk materials was still expected to be yielded by well ordered (e)ALD growth processes and so Seebeck measurements were performed on the non-superlattice samples as well. Some example in-plane and cross-plane configuration Seebeck measurement results are shown in Figure 2.6.

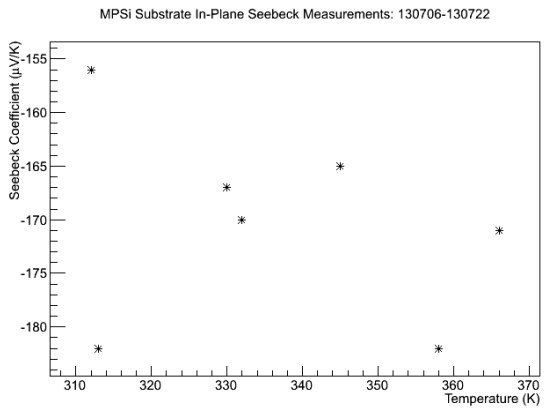

(a) Silicon substrate in-plane Seebeck measurements Seebeck measurements

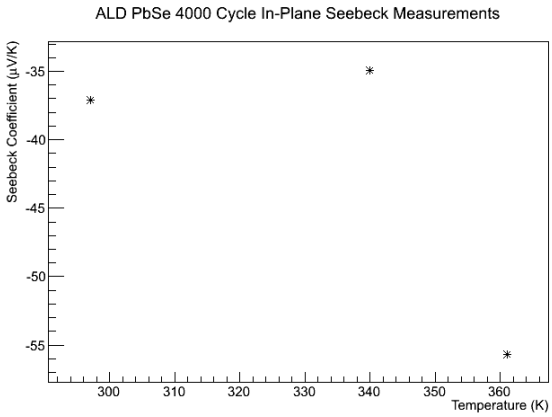

(b) eALD grown (4000 cycle) PbSe on SiO_2 in-plane Seebeck measurements

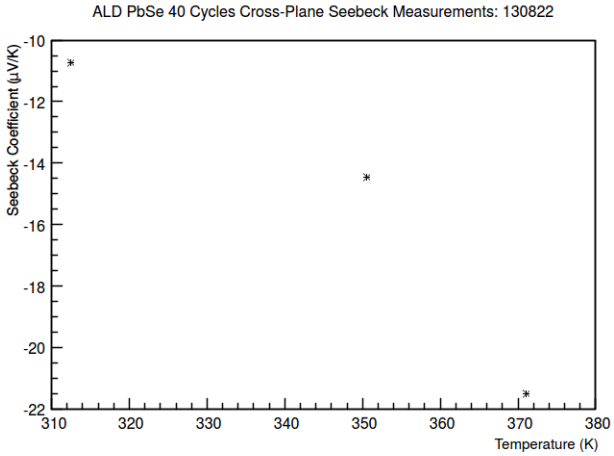

(c) eALD grown (40 cycle) PbSe on Si cross-plane Seebeck measurements

Figure 2.6: Sample In-Plane and Cross-Plane Seebeck Data

The above film measurements are representative of all of the various film measurements taken with this system in that Seebeck coefficients were found to be somewhat close to but still smaller than conventional, unstructured, films made by evaporation techniques [97]. For comparison, bulk

alloyed PbSe has a Seebeck coefficient of -150 $\frac{\mu V}{K}$ to -175 $\frac{\mu V}{K}$ in the temperature range of 300 K to 360 K [9]. A probable cause for the samples failing to yield high Seebeck coefficients lies in their synthesis, as the films were found to be not be homogeneous and of much smaller thicknesses than expected. One of the best films delivered for measurement, PbSe grown by 4000 cycle eALD on SiO_2 over a Si substrate (Figure 2.6b), is shown in Figure 2.7.

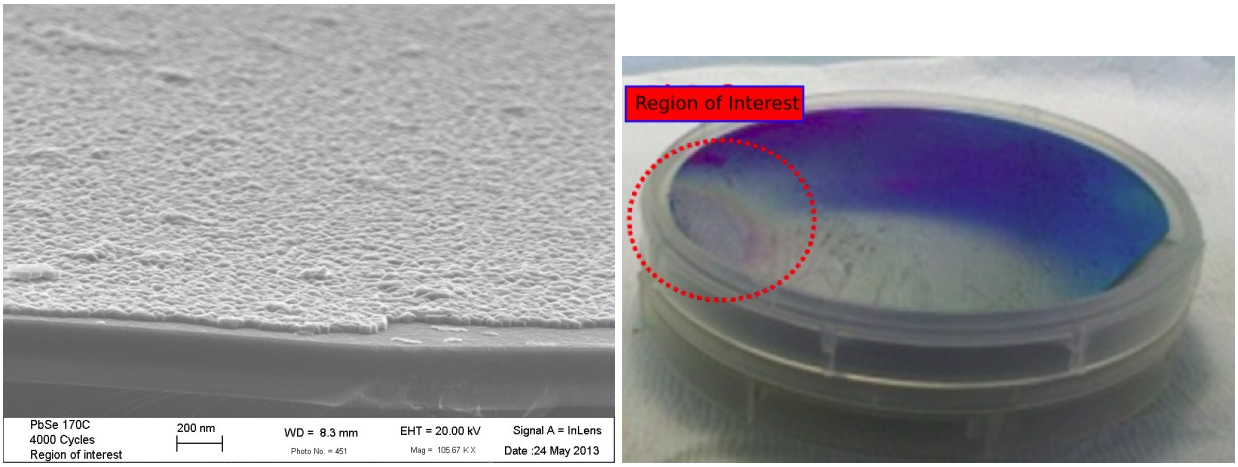

(a) SEM image of 4000 cycle eALD grown 42 nm thick PbSe film on 266 nm thick SiO_2

(b) Photo of wafer with 4000 cycle eALD grown PbSe film

Figure 2.7: Images of the eALD grown PbSe film measured in Figure 2.6b

In the case of a 4000 cycle PbSe eALD growth, one should expect 4000 Pb and Se multilayers, which should yield a much thicker film than the one shown in Figure 2.7a. Further, the eALD growth process occurs by changing baths that the sample wafer is submerged in, so films should be uniform over the entire wafer, which is clearly not the case as shown in Figure 2.7b. Energy-dispersive X-ray spectroscopy (EDS) was also performed on the samples to ensure that the films consisted of the intended elements in the intended ratios. Usually, relative elemental concentrations were close to expected ratios in the films delivered for measurement. One may then assume that some error in the synthesis processes resulted spotty areas of thin films without stacked layers, but rather a more randomized mixture similar to what would be produced by evaporation. Regardless of the cause, well ordered structures were never produced and all of the films measured were

found to have similar or smaller Seebeck coefficients than their respective evaporation produced counterparts.

Chapter 3

Thermal Conductivity Characterization by Frequency Domain Thermoreflectance

3.1 Thermoreflectance Background

The material presented in this chapter closely follows a manuscript under review by the International Journal of Thermophysics under the title of "Measuring thermal conductivity with magnitude-dependent frequency-domain thermoreflectance using modulated CW lasers." Thermal management at ever decreasing size scales is an issue of great importance, both in research and industrial applications. For example, thermal conductivity measurements on small length scales are of critical importance to developments in thermoelectrics [122, 132], reduced-dimensional electronics [63, 87, 124], and in interface studies [6, 25, 37, 56, 73]. Time-domain thermoreflectance (TDTR) has become a go-to method for thermal characterization of thin film samples. It requires minimally invasive sample preparation before relatively rapid thermal property measurements can be carried out. One drawback to this method, however, is the cost of the instruments and, in particular, the necessary ultrafast laser which often costs $100,000 - $140,000. Typical TDTR systems

can cost upwards of $150,000 as a result. To make such measurements more economical, the frequency-domain thermoreflectance (FDTR) system we have employed uses a continuous wave (CW) diode-pumped solid-state laser which costs $5,000. The system present in this chapter cost ≈$25,000 in total. This technique can measure the thermal conductivity in samples that are on the order of 100 nm - 10 μm thick, whereas time-domain methods can be sensitive to films of nanometer thicknesses or less. Consequently, this thickness range is complimentary to those measured by TDTR techniques. In this chapter, Sections 3.1 and 3.2 are background review while Sections 3.3 and 3.4 present the experimental results of this study.

The earliest photothermal displacement measurement techniques [92, 93, 112], which became the foundation of thermoreflectance methods, were based on measuring the displacement of a probe beam resulting from thermoelastic deformation of the sample surface when subject to, typically, a CW pump beam modulated at MHz frequency. Through the use of these methods, a greater understanding of pulsed laser heating on increasingly small scales became possible and ultimately lead to the development of what is now known as TDTR techniques. The first thermal diffusivity measurements [96, 139] were demonstrated with a picosecond pulse length pump laser modulated at MHz frequencies. The ultrafast lasers in TDTR makes nanometer scale spatial resolution of thermal properties possible, and consequently the method has become widespread [16, 17, 18]. Other FDTR methods have been employed using ultrafast lasers [117, 141] in which TDTR systems were modified to run frequency sweeping measurements with fixed time delay. A notable work by Schmidt [116] proposed the use of CW lasers in FDTR and demonstrated FDTR with an ultrafast laser system. The present work differs from Schmidt's proposal in that here we used a magnitude-based measurement in relation to a control sample, as opposed to the phase-based modeling approach proposed by Schmidt. The advantage of our approach is that precise knowledge and modeling of the laser beam profiles and the surface reflective layer is not necessary. An older work by Lepoutre [68] used a similar CW laser system as ours to obtain quantitative thermal diffusivity

measurements of isotropic samples and qualitative measurements of anisotropic samples, though that system operated on probe beam spatial displacement sweeps rather than FDTR.

Thermal conductivity measurements with CW lasers at lower (sub MHz) frequencies have also been accomplished through a photothermal displacement method [57, 69], in which the sample surface is optically heated and the resulting deformation is measured by observing the change in deflection angle of a probe beam tightly focused on the surface. Another common thermal conductivity measurement technique is the 3ω method [14, 72], though it is best suited to electrically resistive samples [60] and requires lithographic patterning on the sample surface. As for thermoreflectance measurements such as the one we demonstrate here, they are based on a non-zero thermo-optic coefficient of thin reflective metallic layers deposited on the sample, which leads to a temperature dependence of the reflectivity. Modulating the power delivered to the sample, the time-dependence of the surface temperature can be measured with thermoreflectance, and the thermal conductivity can be extracted through appropriate physical modeling. Since both heat delivery and temperature measurements are accomplished optically, the only modification of the sample that is required is the deposition of a thin unstructured metal film on the surface.

3.2 Frequency-domain Thermoreflectance Theory

To interpret the data generated by the measurement, we need to develop a physical model of the technique, shown schematically in Fig. 3.1. This model is based on the following assumptions: First, Gaussian beam profile (TEM_{00}) lasers are used for heating (pump) and reflectivity measurements (probe). We will initially take the diameter of the probe beam spot to be much smaller than the pump beam spot and concentric with it on the sample surface. Second, the sample is homogeneous, smooth, and of thickness much greater than the thermal diffusion length (Eq. 3.14). Third, the sample surface is coated in a high thermo-optic coefficient reflective film taken to be thin

enough that lateral heat conduction through the film has no effect on sample temperature distribution and there is no significant lag time associated with heat transmission through the film. The choice of reflective thermo-optic material is dependent upon temperature range and wavelength of the probe laser.

The temperature field of a homogeneous sample can be represented by $\mathrm{u(x,y,z;t)} = \mathrm{T} - \mathrm{T_0}$ where $\mathrm{T_0}$ is the background temperature under steady state conditions. u satisfies the heat equation:

$$\kappa_{\parallel}(\mathrm{u_{xx}} + \mathrm{u_{yy}}) + \kappa_{\perp}\mathrm{u_{zz}} = \mathrm{c_p}\rho\mathrm{u_t}. \tag{3.1}$$

Here $\kappa_{\perp}, \kappa_{\parallel}$ are the perpendicular (cross-plane) and parallel (in-plane) thermal conductivities of the sample relative to the sample surface, $\mathrm{c_p}$ is the specific heat, ρ is the density of the sample, and the subscripts x, y, z, and t indicate partial derivatives. The heat equation is applicable to thermoreflectance systems so long as the regions being probed are larger than the ballistic thermal transport regieme, as defined by the phonon mean free path which is on the order of 10 nm or less at room temperature in most materials.

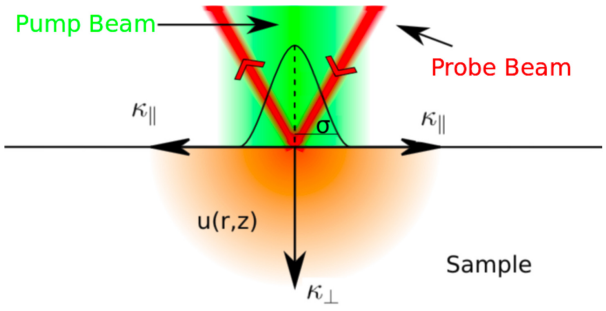

Figure 3.1: Schematic side view showing the pump and probe beam, both from CW lasers, as they respectively generate and measure the temperature field $\mathrm{u(r,z)}$ in the sample, which has lateral and vertical thermal conductivities $\kappa_{\parallel}$ and $\kappa_{\perp}$.

By recognizing that the time dependence of the temperature field will behave as $\mathrm{u(x,y,z;t)} = \mathrm{u(x,y,z)e^{i\omega t}}$, we can then work with the temperature field primarily in terms of spatial components

and modulation frequency, allowing the temperature field to be expressed as $\mathrm{u}(\mathrm{x},\mathrm{y},\mathrm{z};\boldsymbol{\omega})$, and then setting the boundary conditions as:

$$\mathrm{u_z}(\mathrm{x},\mathrm{y},0;\boldsymbol{\omega}) = -\frac{\mathrm{q}(\mathrm{x},\mathrm{y})}{\boldsymbol{\kappa_\perp}}. \tag{3.2}$$

$$\mathrm{u}(\mathrm{x},\mathrm{y},\infty;\boldsymbol{\omega}) = 0, \tag{3.3}$$

Here $\mathrm{q}(\mathrm{x},\mathrm{y})$ is the surface density of the heat deposited on the sample at angular modulation frequency $\boldsymbol{\omega}$. In the case of the Gaussian intensity profile heating,

$$\mathrm{q}(\mathrm{x},\mathrm{y};\mathrm{t}) = \frac{2\mathrm{Q}}{\boldsymbol{\pi\sigma^2}}\mathrm{e}^{-\frac{2(\mathrm{r}^2)}{\sigma^2}}\mathrm{e}^{\mathrm{i}\boldsymbol{\omega}\mathrm{t}}. \tag{3.4}$$

Here Q is the total heat absorbed by the sample and $\mathrm{r} = \sqrt{\mathrm{x}^2+\mathrm{y}^2}$ is the distance from the z-axis. The equation set by the boundary conditions can be solved by separation of variables when expressed in cylindrical coordinates, $(\mathrm{r},\boldsymbol{\phi},\mathrm{z})$ so that $\mathrm{u}(\mathrm{r},\boldsymbol{\phi},\mathrm{z}) = \sum_{\mathrm{k}} \mathrm{R_k}(\mathrm{r})\mathrm{Z_k}(\mathrm{z})$ with

$$\mathrm{R_k}(\mathrm{r}) = \mathrm{k}\mathrm{C_k}\mathrm{J_0}(\mathrm{kr}), \tag{3.5}$$

$$\mathrm{Z_k}(\mathrm{z}) = \exp\Big(-\mathrm{z}\sqrt{\tfrac{\mathrm{i}\boldsymbol{\omega}\mathrm{c_p}\boldsymbol{\rho}}{\boldsymbol{\kappa_\perp}} + \tfrac{\boldsymbol{\kappa_\parallel}}{\boldsymbol{\kappa_\perp}}\mathrm{k}^2}\Big). \tag{3.6}$$

Here $\mathrm{J_0}(\mathrm{kr})$ is a 0^{th} order Bessel function of the first kind, k indexes the particular solution and $\mathrm{C_k}$ can be found through matching to the boundary conditions. The full solution to the problem is found by integrating the particular temperature fields over all indices k. As the measurements are only sensitive to temperature changes at the surface, only the case of $\mathrm{z} = 0$ is of interest. Applying these simplifications yields the full solution:

$$\mathrm{u}(\mathrm{r},0;\boldsymbol{\omega}) = \frac{1}{\sqrt{\boldsymbol{\kappa_\perp}\boldsymbol{\kappa_\parallel}}}\int_0^\infty \frac{\mathscr{H}_0\{\mathrm{q}(\mathrm{r})\}}{\sqrt{\frac{\mathrm{i}\boldsymbol{\omega}\mathrm{c_p}\boldsymbol{\rho}}{\boldsymbol{\kappa_\parallel}} + \mathrm{k}^2}}\mathrm{k}\mathrm{J_0}(\mathrm{kr})\mathrm{dk}. \tag{3.7}$$

Here $\mathscr{H}_0$ is the 0^{th} order Hankel transform. In the case of the Gaussian intensity profile heating, this becomes, on non-dimensionalized form:

$$\mathrm{u}(\tilde{\mathrm{r}},0;\boldsymbol{\gamma}) = \frac{\mathrm{Q}}{\pi\sigma}\sqrt{\frac{2}{\kappa_{\parallel}\kappa_{\perp}}}\int_0^{\infty}\frac{\mathrm{e}^{-\tilde{\mathrm{k}}^2}}{\sqrt{\mathrm{i}\boldsymbol{\gamma}+\tilde{\mathrm{k}}^2}}\tilde{\mathrm{k}}\mathrm{J}_0(\tilde{\mathrm{k}}\tilde{\mathrm{r}})\mathrm{d}\tilde{\mathrm{k}}, \tag{3.8}$$
$$\tilde{\mathrm{k}} = \frac{\sigma}{\sqrt{8}}\mathrm{k} \qquad \tilde{\mathrm{r}} = \frac{\sqrt{8}}{\sigma}\mathrm{r} \qquad \boldsymbol{\gamma} = \frac{\omega \mathrm{c_p}\rho\sigma^2}{8\kappa_{\parallel}}.$$

Here, $\boldsymbol{\gamma}$ is a dimensionless pump modulation frequency used for convenience, and $\tilde{\mathrm{k}}$ and $\tilde{\mathrm{r}}$ are dimensionless versions of k and r. This result was also found by Cahill [15] in an analogous method. Because of the finite extent of the probe beam, our technique does not observe the temperature field directly at a localized point, but rather as a weighted average over the probe spot area which further complicates the problem. This can be expressed as a convolution integral that needs to be evaluated numerically. However, in the limit of a small probe beam spot that is perfectly aligned with the center of the pump beam, we can take the signal to depend only on $\mathrm{u}(0,0)$, which does have a closed-form expression:

$$\begin{aligned}\mathrm{u}(0,0;\boldsymbol{\gamma}) &= \frac{\mathrm{Q}}{\sqrt{2\pi\sigma^2\kappa_{\perp}\kappa_{\parallel}}}\mathrm{e}^{\mathrm{i}\boldsymbol{\gamma}}\mathrm{erfc}\sqrt{\mathrm{i}\boldsymbol{\gamma}}. \\ &= \frac{\mathrm{Q}}{\sqrt{2\pi\sigma^2\kappa_{\perp}\kappa_{\parallel}}}\mathrm{w}(-\sqrt{\frac{\boldsymbol{\gamma}}{\mathrm{i}}}),\end{aligned} \tag{3.9}$$

Here w is known as the Faddeeva function [135]. From Eq. 3.8 (as well as 3.9), it is apparent that, at least for isotropic samples, the magnitude of the temperature field scales inversely with thermal conductivity and that the frequency response, as expressed in the definition of $\boldsymbol{\gamma}$, scales inversely with thermal diffusivity ($\frac{\kappa}{\mathrm{c_p}\rho}$), while the functional form of the measured traces depend only on the shape and size of the laser beams. Therefore, by sweeping the modulation frequency of the heating laser and monitoring the resulting changes in surface temperature, thermal conductivity measurements can be obtained through the application of a model to the resultant trace.

In our experiment, this theory yields trends which are of the same general form as the observed traces, but the functional form of the theoretical traces are not sufficiently close to the observed data to enable direct fitting with measurement data. We believe the primary cause of this discrepancy is deviations in the actual beam intensity profiles from a simple Gaussian peak, though complications arising from the reflective surface layer deposited on the sample, pump-probe beam misalignment, or stray reflections could also be factors. Illustrating this issue, Fig. 3.2 plots a numerical evaluation of the pump and probe convolution for Gaussian TEM_{00}, Lorentzian, and Gaussian TEM_{01^*} beam profiles assuming perfect alignment ($\mathrm{d} = 0$) and literature values for thermal properties of a CaF_2 sample measured by the system described below. Our data obtained from CaF_2 is overlaid as a comparison.

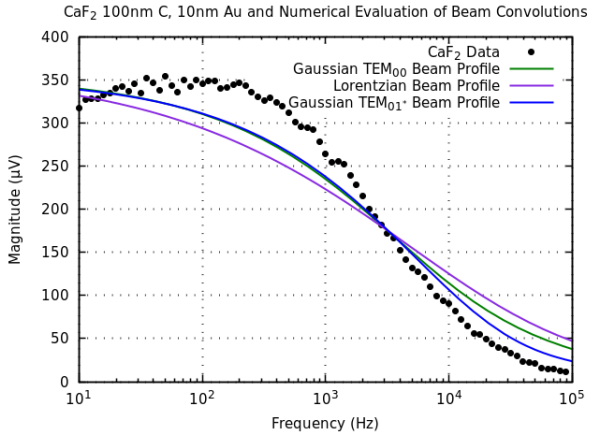

Figure 3.2: Theoretical traces derived from our model, numerical evaluation of pump-probe beam convolution vs. bulk CaF_2 sample measurement.

This problem can be side-stepped by performing an identical measurement on a control sample and then scaling the magnitude and frequency dependence of the resultant trace by factors α and β respectively until the control trace fits the sample of interest trace. Because both the control and sample of interest measurements use the same lasers and optical setup, precise modeling of the beam profiles becomes unnecessary. Symbolically, we have that:

$$
\begin{aligned}
&\mathrm{u_s}(0,0;\gamma_\mathrm{s}) = \alpha \mathrm{u_c}(0,0;\beta\gamma_\mathrm{c},) \\
&\rightarrow \frac{1}{\sqrt{\kappa_{\perp\mathrm{s}}\kappa_{\parallel\mathrm{s}}}} \frac{\mathrm{Q}}{\sqrt{2\pi\sigma^2}} \mathrm{e}^{\frac{\mathrm{i}\omega\sigma^2}{8}\frac{\mathrm{c_{p_s}}\rho_\mathrm{s}}{\kappa_{\parallel\mathrm{s}}}} \operatorname{erfc}\sqrt{\frac{\mathrm{i}\omega\sigma^2}{8}\frac{\mathrm{c_{p_s}}\rho_\mathrm{s}}{\kappa_{\parallel\mathrm{s}}}}, \\
&= \frac{\alpha}{\sqrt{\kappa_{\perp\mathrm{c}}\kappa_{\parallel\mathrm{c}}}} \frac{\mathrm{Q}}{\sqrt{2\pi\sigma^2}} \mathrm{e}^{\frac{\mathrm{i}\omega\sigma^2}{8}\frac{\beta\mathrm{c_{p_c}}\rho_\mathrm{c}}{\kappa_{\parallel\mathrm{c}}}} \operatorname{erfc}\sqrt{\frac{\mathrm{i}\omega\sigma^2}{8}\frac{\beta\mathrm{c_{p_c}}\rho_\mathrm{c}}{\kappa_{\parallel\mathrm{c}}}}.
\end{aligned}
\tag{3.10}
$$

Here the subscripts s and c indicate sample of interest and control sample properties, respectively. From this we can see that the scaling factor α is a ratio of the thermal conductivities, while β is a ratio of the thermal diffusivities of the control and sample of interest:

$$
\frac{\alpha}{\sqrt{\kappa_{\perp\mathrm{c}}\kappa_{\parallel\mathrm{c}}}} = \frac{1}{\sqrt{\kappa_{\perp\mathrm{s}}\kappa_{\parallel\mathrm{s}}}} \quad \text{and} \quad \frac{\beta\mathrm{c_{p_c}}\rho_\mathrm{c}}{\kappa_{\parallel\mathrm{c}}} = \frac{\mathrm{c_{p_s}}\rho_\mathrm{s}}{\kappa_{\parallel\mathrm{s}}}. \tag{3.11}
$$

This is reduced as follows to obtain the perpendicular and parallel thermal conductivity components of the sample of interest:

$$
\kappa_{\perp\mathrm{s}} = \frac{\beta\,\kappa_{\perp\mathrm{c}}\mathrm{c_{pc}}\rho_\mathrm{c}}{\alpha^2\mathrm{c_{ps}}\rho_\mathrm{s}} \quad \text{and} \quad \kappa_{\parallel\mathrm{s}} = \frac{\kappa_{\parallel\mathrm{c}}\mathrm{c_{ps}}\rho_\mathrm{s}}{\beta\,\mathrm{c_{pc}}\rho_\mathrm{c}}. \tag{3.12}
$$

In the case of materials which are isotropic with respect to thermal conductivity, this simplifies, yielding two simultaneous measurements of thermal conductivity:

$$
\kappa_\mathrm{s} = \frac{\kappa_\mathrm{c}}{\alpha} \quad \text{and} \quad \kappa_\mathrm{s} = \frac{\kappa_\mathrm{c}\mathrm{c_{p_s}}\rho_\mathrm{s}}{\beta\,\mathrm{c_{p_c}}\rho_\mathrm{c}}. \tag{3.13}
$$

Accordingly, the two methods of measuring thermal conductivity can be used to double check either obtained value for isotropic samples, or enable independent $\kappa_\parallel$ and $\kappa_\perp$ measurements to be taken during a single measurement run. Fig. 3.3 illustrates an example measurement of CaF_2 fit with a scaled control glass measurement.

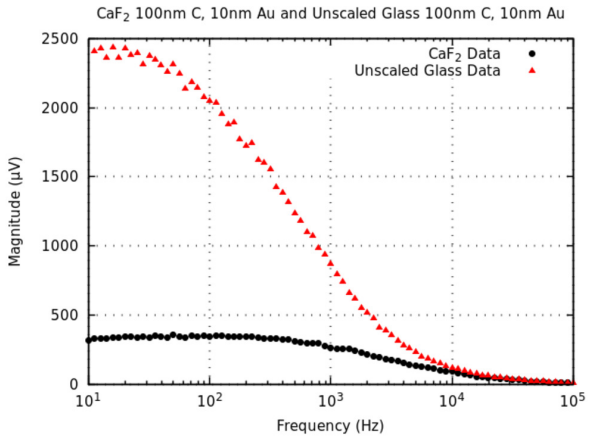

(a) Sample and control measurements

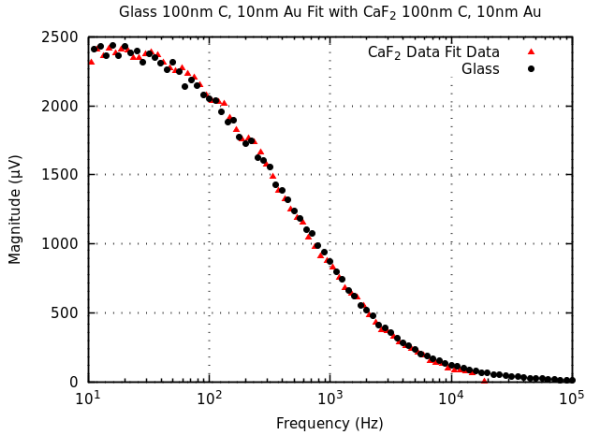

(b) Sample measurement and fit

Figure 3.3: An example of FDTR measurement and fitting. Here, a CaF_2 control sample was used to fit a soda-lime glass sample of interest with α=6.897 and β=6.

We note that the analysis uses the magnitude of the signal rather than the phase, because we found the phase in our setup to be a less reliable measure of thermal conductivity and a worse fit to theory.

The film thicknesses that can be readily measured by thermoreflectance systems is ultimately limited by the frequency-dependent thermal diffusion length L [92, 93, 114] of the sample:

$$\mathrm{L} = \sqrt{\frac{2\kappa}{\mathrm{c_p}\rho\,\omega}}. \tag{3.14}$$

L corresponds to the length at which the magnitude of the thermal wave initiated by the pump beam is attenuated by a factor of e^{-1}. The thermal diffusion lengths at the frequency extremes used in this study are as follows: Al_2O_3 L(10Hz)≈0.56 mm, L(100kHz)≈5.6 μm; CaF_2 L(10Hz)≈0.34 mm, L(100kHz)≈3.4 μm; soda-lime glass L(10Hz)≈0.13 mm, L(100kHz)≈1.3 μm. The measurements are not sensitive to material properties at depths that are large compared to L, nor can the thermal conductivity of films with thicknesses much less than L be easily measured. Therefore, samples with smaller thermal diffusivities subjected to pump modulation at higher frequencies will have the smallest thermal penetration depth and, consequently, finest spatial resolution. To keep signal response high, changes in modulation frequency ω must be balanced by changes in pump beam spot size σ in order to keep the γ factor of Eq. 3.8 near unity, where $\mathrm{du}/\mathrm{d}\omega$ is the greatest. Thus maximum system response occurs when Eq. 3.15 is satisfied:

$$\sigma = \sqrt{\frac{8\kappa_{\parallel}}{\omega \mathrm{c_p}\rho}}. \tag{3.15}$$

The system used in this paper was designed to be maximally sensitive to a fused silica sample of thickness of ≈ 1 μm around 50 kHz pump modulation. This minimum spatial resolution can be improved upon by increasing the frequency. In our case, we were limited to a maximum frequency of 100 kHz by our lock-in amplifier, but with other instrumentation, we could easily reach hundreds of MHz without a significant increase in cost. Such a system would be capable of measuring the

thermal properties of films with thicknesses in the range of tens of nanometers.

3.3 Experimental Setup

The pump laser in our experiment was a modulated CW diode-pumped solid-state laser emitting at 532 nm, while the probe beam was generated by a 632.8 nm HeNe laser. The complete thermoreflectance system used in this work is illustrated in Fig. 3.4. The probe wavelength was chosen because it is near a maximum of the thermo-optic coefficient spectrum of gold, a material which we could easily deposit on the samples. As lock-in detection was used in conjunction with a photomulitiplier tube, the reflected probe beam needed to be isolated from the reflected pump beam for detection. To separate the beams, the pump beam was reflected onto the center of the microscope objective focal plane by a dichroic mirror which permitted the probe beam to pass. The incident probe beam was reflected by a nonpolarizing beamsplitting cube which was slightly offset from the dichroic mirror, onto the microscope objective. This configuration caused the incident probe beam to be offset from the pump beam on the back plane of the microscope objective but still brought both beams to the focal point of the objective at the same point on the sample surface. Consequently, the reflected probe beam was equally and symmetrically offset from the pump beam upon exiting the microscope objective. This spatial offset of the reflected beams allowed the reflected probe beam to be separated using an aperture prior to the photomultiplier tube detector. Further, a dichroic filter was installed immediately before the detector to remove stray pump reflections from the signal.

To minimize error in thermal conductivity measurements, the measurement conditions of the control sample and the sample of interest must be as similar as possible. To achieve this, sample and beam alignment were performed using a CMOS camera, which was installed behind a removable mirror which directed the probe beam to the detector. Samples were mounted on a stage capable

of x,y,z translation and the pump and probe beam positions were controlled with kinematic mirror mounts. Once the sample was brought into focus, the removable mirror was reinstalled and the probe beam location was adjusted until the (unmodulated) measured signal was maximized. Then the mirror was removed again and the pump beam spot was moved until it was centered upon the probe beam spot on the sample. By following this alignment method, uncertainties induced by sample exchange were minimized.

To bring the system as close as possible to measuring the temperature at $\mathrm{r} = 0$, the pump beam was expanded by two achromatic doublet lenses such that the probe beam spot size was approximately half of the pump beam spot size. The spot size of the beams on the surface of the sample was set by the microscope objective used. To increase the signal to noise ratio of the frequency sweeping measurements, we sought to perform measurements in the regime of maximum temperature change with respect to frequency. The frequency response of the complex temperature field of Eq. 3.9 is defined by the γ parameter, and one can show that the first derivative of the magnitude of the temperature field with respect to γ is maximized when $\gamma \approx 1$. The minimum pump beam radius σ on the sample was ultimately limited by thermal damage to the reflective film layer while the maximum modulation frequency of our system was limited to less than 100 kHz by the lock-in amplifier we used in detection. Bearing these constraints in mind, the microscope objective was selected to yield magnification such that on the sample surface the pump beam spot size was ≈ 105 $\mu\mathrm{m}$ and the probe beam spot size was ≈ 58 $\mu\mathrm{m}$, in the case of CaF_2 this yields $\gamma \approx 1$ at 50 kHz. Our system was most sensitive to samples of thermal diffusivities ranging from around $1\mathrm{x}10^{-6}$ $\frac{\mathrm{m}^2}{\mathrm{s}}$ to $3\mathrm{x}10^{-5}$ $\frac{\mathrm{m}^2}{\mathrm{s}}$, corresponding approximately to fused silica and GaAs respectively. The range of modulation frequencies used in the measurements were between 10 Hz and 100 kHz. As stated previously, the upper limit of the frequency range was set by the maximum operating frequency of the lock-in used, but the lower limit is chosen such that the thermal diffusion length is kept substantially smaller than σ or in the case of thin samples keeping the thermal diffusion length less

than the sample thickness.

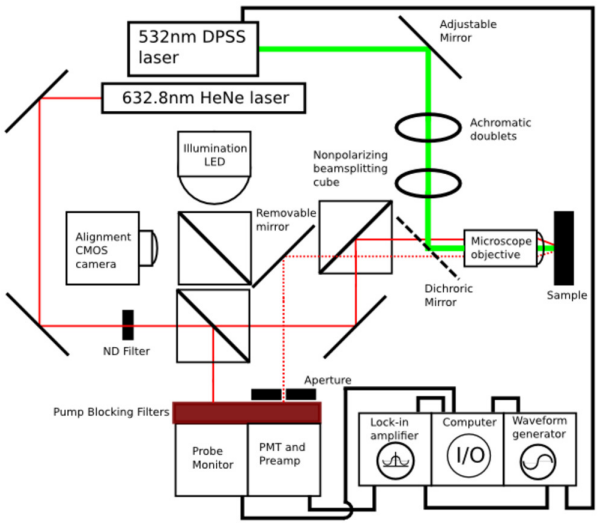

Figure 3.4: Diagram of the thermoreflectance system.

Measurements were performed by logarithmically stepping the pump beam modulation frequency and recording the resultant magnitude and phase measurements of the lock-in amplifier. For each new frequency setting, the lock-in sensitivity was automatically rescaled, and after a fixed settling time, data was recorded. This control was managed through the ThermReflectMK23.vi Labview program. In analysis, mean and error values were calculated for data taken for each frequency setting using ThermreflecAnalyzerMk3.py, though statistical error values for each frequency setting were found to be negligibly small. To prevent the probe beam from over-heating the sample, it was attenuated with a neutral density filter prior to incidence such that the probe beam power at the sample was 40 μW. The probe beam was also monitored by a Si photodiode detector in order to correct for probe power fluctuations which would occur during measurements. However, those fluctuations were found to be negligibly small ($\approx 0.2\%$).

To monitor changes in surface temperature of the sample, a thin metallic surface film with a high thermo-optic coefficient was needed. Changes in reflectivity of metals are well approximated as being linearly proportional to changes in the temperature of the metal when temperature differences

are less than tens of Kelvins [96, 130]. Further, to keep with the method developed here, heat conduction in the plane of the reflective film needed to be minimized. The reflective film layer was composed of gold deposited via e-beam evaporation. Gold was chosen due to its high thermo-optic coefficient with respect to the 632.8 nm probe beam [107], but it has the disadvantage of being a very good heat conductor. Therefore, to avoid having to take heat conduction through the gold film into account, the gold was deposited onto a 100 nm film of graphite-like carbon, which was first deposited on the sample via excimer laser ablation [77]. Simpler systems, such as carbon sputtering, could also be used for graphite-like carbon deposition, but we chose the excimer system as it was readily available in our lab. The graphite-like carbon layer has a thermal conductivity of $0.25\ \frac{\mathrm{W}}{\mathrm{m}\cdot\mathrm{K}}$ [120], which is more than 1000 times less than gold, and causes gold deposited on it to form discrete aggregates rather than a continuous film, as the scanning electron microscope image of one such sample shown in Fig. 3.5 demonstrates. This disrupts thermal conduction through the gold layer, minimizing its impact on the measurement, while still causing specular reflection of the beams. This scheme causes in-plane heat conduction in the transducer layer to take place only in the carbon layer.

In plane heat conduction in the carbon layer must be negligible, relative to the sample, in order for the theory to hold. The effect of in plane heat conduction in the carbon layer can be studied by comparing the thermal diffusion lengths and effective sheet thermal conductivities of the sample and carbon layer. The thermal diffusion length of the carbon layer at the frequency extremes used in this study are L(10 Hz)$\approx$74 μm and L(100 kHz)$\approx$0.74 μm, which are sufficiently long compared to the film thickness (100 nm) that it should have a negligible impact on heat conduction to the sample. Further, the effective sheet thermal conductivity of the layer is consequently limited by the layer thickness and is the product of the thermal conductivity and layer thickness. The effective sheet thermal conductivity of the carbon layer then is $\approx 25\ \frac{\mathrm{nW}}{\mathrm{K}}$. Comparing this with the case of CaF_2, where the thermal diffusion length is much smaller than the sample thickness and

thus determines the effective thermal thickness, we get $\approx 33\ \frac{\mu W}{K}$ at L(100kHz) which validates the assumption of limited thermal effect of the transducer layer on the sample with regards to in plane heat conduction.

To verify that cross plane heat conduction is minimally influenced by the carbon layer, we can compare the thermal diffusion time and heat pulse period. Thermal diffusion time here is also limited by either film thickness or thermal penetration depth and equals the square of the shorter of those two lengths divided by the thermal diffusivity. The thermal diffusion time in the carbon film is then $\approx$ 58 ns, which is much shorter than the minimum heating pulse period of 10 μs, corresponding to 100 kHz, used in these measurements. In effect, the heating pulse modulations occur at too slow of a rate to produce meaningful heat differences across the carbon film.

Consideration was given to ensuring minimal bulk heating of the samples. The combined 10 nm gold and 100 nm carbon films transducer was measured to have $\approx 10\%$ pump beam power transmission. The penetration depths, corresponding to a e^{-1} reduction of laser power, of the samples are much longer than the thicknesses of the samples and the samples measured here were transparent in visible wavelengths. The penetration depth of soda-lime glass at 532 nm is 233 mm [113] and though we were unable to find penetration depth measurements of Al_2O_3 and CaF_2 at 532 nm, published data indicate penetration depth of 20 m for CaF_2 at 2.7 μm [42] and 2 m for Al_2O_3 at 510 nm [102]. From this we can conclude that bulk sample heating was negligible.

We also measured the samples with an established TDTR system to verify our results. The TDTR system used a Ti-sapphire laser to generate femtosecond pulses at a frequency of 80 MHz. The pulses were split into two beams, the pump beam and the probe beam. The pump beam was modulated at a frequency of 10 MHz, using an electro-optic modulator. The modulated pump beam was then used to excite a $\approx$30-40 nm thick aluminum film that acted as the transducer for the experiment. The aluminum film was deposited by e-beam evaporation. Due to the high thermo-optic coefficient of aluminum at the pump wavelength, the initial temperature rise and

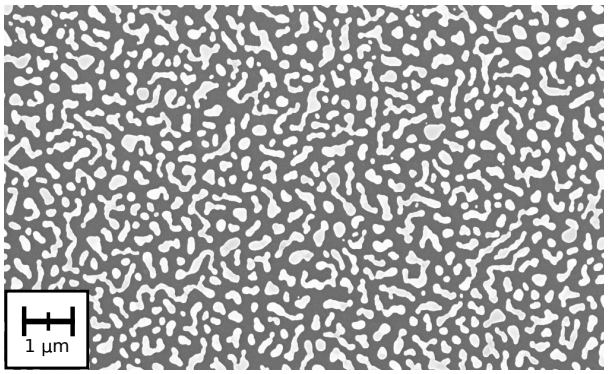

Figure 3.5: Scanning electron microscope image of the surface reflective layer. An Al_2O_3 sample is coated with 100 nm graphite-like carbon followed by 10 nm gold. The discrete island structure of the gold inhibits in-plane conductivity in the reflective layer.

its subsequent decay could be monitored using the time-delayed probe beam that arrived at the aluminum surface some time after the pump beam. The probe beam path was adjusted using a corner cube reflector mounted on a mechanical delay stage that travels ≈550 mm which translates to 3.5 ns of delay between the arrival of the pump and probe beams at the transducer surface. Intensity changes of the probe beam at the modulation frequency of the pump beam were measured by a lock-in amplifier using a photodiode detector. The lock-in amplifier recorded an in-phase, V_{in}, and out-of-phase, V_{out}, voltage as a function of time. The ratio of these two voltages, $\frac{V_{in}}{V_{out}}$, was then compared to a theoretical thermal model [15] that describes heat flow in layered media where the surface is heated by a periodic point source of heat. The parameters of thermal conductivity and interfacial thermal conductance of the sample were adjusted until a best fit was achieved between the experimental data and the theoretical model.

3.4 Results and Discussion

Thermal conductivities were measured through a comparison of data from a sample with known thermal properties and the sample of interest. Both the sample of interest and the control sam-

ple were prepared through reflective film deposition conducted at the same time. For the data presented here, CaF_2 was used as the control material. Both the sample of interest and the control sample were measured under identical focusing conditions through the frequency sweeping method described above.

Upon completion of the measurements, the magnitude and frequency values of the control measurement were scaled by the constant factors α and β, respectively, to fit the trace of the sample of interest, as shown in Fig. 3.3. Thermal conductivity values could then be found by Eq. 3.12 for anisotropic materials or by Eq. 3.13 for isotropic materials. To demonstrate the validity of this FDTR technique, we examined an Al_2O_3 window, purchased from Thorlabs, as well as a soda-lime glass microscope slide and compared them with literature values. For the soda-lime glass (72% SiO_2, 14% Na_2O) sample we used: $\rho = 2.48\ \frac{\mathrm{g}}{\mathrm{cm}^3}$, and $\mathrm{C_p} = 0.801\ \frac{\mathrm{J}}{\mathrm{gK}}$ [48]. Soda-lime glass thermal conductivity can vary substantially based on constituent concentrations and the ratios of those constituents often vary non-negligably from batch to batch in production. Thermal conductivity values from $\kappa = 0.7-1.3\ \frac{\mathrm{W}}{\mathrm{m{\cdot}K}}$ [43, 52] are considered standard for the formulation of glass used in this study. For CaF_2 we used: $\kappa = 9.71\ \frac{\mathrm{W}}{\mathrm{m{\cdot}K}}$, $\rho = 3.18\ \frac{\mathrm{g}}{\mathrm{cm}^3}$, and $\mathrm{C_p} = 0.854\ \frac{\mathrm{J}}{\mathrm{gK}}$ [138]. Comparing with literature values for the thermal conductivity of Al_2O_3 is not as easily accomplished due to the variance in thermal transport properties arising from both the anisotropic crystal structure and the manufacturing process. Optical grade Al_2O_3 ($> 99\%$) was used in this study and while the density ($3.97\ \frac{\mathrm{g}}{\mathrm{cm}^3}$) and specific heat capacity ($0.753\ \frac{\mathrm{J}}{\mathrm{gK}}$) are well known, the thermal conductivity can vary substantially, in the range of $25-33\ \frac{\mathrm{W}}{\mathrm{m{\cdot}K}}$ [101, 138]. Further, while it is known that Al_2O_3 is anisotropic in thermal conductivity, few studies on the anisotropy of the different grades of Al_2O_3 exist.

The results of measurements taken with the TDTR system and the FDTR system developed here are shown in Table 3.1 along with literature values.

While the data found indicates that the method is indeed viable for samples of several microns

Thermal Conductivity ($\frac{W}{m \cdot K}$)		Al_2O_3	Soda-lime Glass
From Literature		25-33	0.7-1.3
From TDTR		22.1	0.9
FDTR	Isotropic Assumption		
	From Magnitude Factor (α)	42.2	1.3
	From Frequency Factor (β)	35.0	1.0
	Anisotropic $\kappa_{\perp}$	51.0	
	Anisotropic $\kappa_{\parallel}$	34.0	

Table 3.1: Measured thermal conductivity as obtained with FDTR, TDTR, and compared with literature.

(or greater) thickness, there are limitations. The materials which this system can measure are dependent upon the pump beam spot size as well as the modulation frequency. The design of the system must therefore take into account the range of expected thermal conductivity values and the thickness of the sample films, as discussed earlier.

Isotropic and anisotropic thermal conductivity measurements of Al_2O_3 and soda-lime glass were performed with an alternative FDTR method and found to be in reasonable agreement with literature and verified with a conventional time-domain thermoreflectance system. Through the application of a modulated diode-pumped solid-state laser as a heating mechanism, the measurements were performed over a frequency range from 10 Hz to 100 kHz and thermal conductivity values were extracted from observed changes in surface reflectivity. The spatial resolution of the method is larger than in TDTR, and in fact complementary to it, as film thicknesses in the range of 100 nm - 10 μm are not easily probed by bulk methods, and are not accessible to TDTR. These measurements demonstrate the viability of this system as a more economical alternative to time-domain thermoreflectance measurement systems when measuring samples of thickness on the order of 0.1 micron or larger. Future directions of this research will include using our method with different types of reflective films, such as discrete film deposition of varying island thicknesses defined by photolithography, measurements observing the decaying heat behavior at radial distances from the

pump beam center, and measurements of thinner samples using higher frequencies.

Chapter 4

Thermal Rectification Studies of Etched Silicon Nanostructures

4.1 Principles of Thermal Rectification

Thermal rectification is defined as occurring when the thermal conductance along one axis of a material is dependent on the sign of the heat flux along that axis [110]. There are many applications of such materials. Passive directing of heat flow could be used to enhance microcircuit performance, as it is often limited by thermal management, as well as potentially enabling the creation of thermal transistors, diodes, logic circuits, and thermal computation devices. In this chapter, Sections 4.1, 4.2, and 4.4 are background review while Sections 4.3, 4.5, and 4.6 present the results of this study.

The first study of thermal rectification was performed by Starr [125] where thermal rectification was observed by happenstance in a copper plate with an oxide layer while investigating the electrical rectification of the system. In this system, Starr found 30% greater heat conduction in the metal to oxide direction for a temperature difference around 20 K at an average temperature of

298 K. The cause of thermal rectification in this system is due to an interface effect between the two layers. In the metal, heat is carried primarily by electrons while in the oxide, heat is carried primarily by phonons. At the interface between the two layers, scattering occurs and the method of heat transfer is changed depending on direction. The reason for rectification at this junction is due to non-equilibrium scattering rates which lead to energy transfer from electrons to phonons being different from energy transfer from phonons to electrons [76].

Beyond the carrier mismatching observed by Starr, thermal rectification can be achieved through a variety of methods. One method is based on thermal strain, where materials of different thermal expansion coefficient are pressed together [5]. In such a case, the pressure and contact area of the junction are dependent on the sign of the temperature gradient across the junction. Another method involves mating two materials which have opposing temperature dependence in thermal conductivity [82]. Jezowski and Rafalowicz [54] experimented with such a system using graphite and quartz, in which the thermal conductivity of graphite increases with decreasing temperature while the quartz thermal conductivity decreases with decreasing temperature. This resulted in higher heat conduction in the direction of quartz to graphite.

In more recent years, nanoscale structures have presented interesting prospects for thermal rectification. The work of Terraneo [127] sparked great interest in nanostructured thermal rectification devices with his theoretical work involving non-linear 1-dimensional lattices, which proposed a factor of two difference in heat conduction due to phonon band matching that causes effective phonon frequencies to change in response to the sign of the temperature gradient. In spite of recent advances in nanomanufacturing, it has proven difficult to make physical structures in line with the theoretical work of Terraneo and other idealized systems [110].

One novel avenue of thermal rectification which has seen some experimental verification recently is based on novel properties of superconducting junctions. Theoretical work by Giazotto [39, 81] predicted thermal rectification ratios two orders of magnitude greater than what was previ-

ously demonstrated. In this case, normal metal-superconductor (NS) and superconductor-insulator-superconductor (SIS) junctions exhibited thermal rectification resulting from the strong temperature dependence of the density of states in superconductors. This dependency regulates electron current depending on temperature gradient, which consequently regulates electronic heat conduction. In such superconducting junction systems, electronic heat conduction is the dominant method of heat conduction. Giazotto then went on to demonstrate the method experimentally [80] using a NINISIN junction where rectification of 140% was observed. Though this is a great achievement in the field of thermal rectification, the practical viability of the system is very limited. The system itself was composed of 25 nm thick strips defined by electron-beam lithography and very low operating temperatures (≈ 0.5 K) as well as correspondingly small heat flux. These operating requirements functionally limit the design to extremely niche applications.

A notable discovery by Chang [21] observed thermal rectification in non-uniformly mass-loaded single-walled carbon and boron-nitride nanotubes. In Chang's work, Trimethylcyclopentadienyl platinum was deposited in an amorphous state on the nanotubes such that the greatest mass-density was on one tube end while decreasing in the direction of the opposite tube end. 2%-7% thermal rectification was observed in such structures with greater heat conduction in the direction of lesser mass-density to greater mass-density, opposite to what was expected from ballistic phonon-dominated heat conduction in such asymmetric geometries. This is particularly interesting when one considers that previous studies have found ballistic phonon heat conduction to be the dominant method in nanotube structures [23].

The primary issue with implementation of most methods of thermal rectification is the limited applicability. Specifically, most demonstrated thermal rectification methods rely on interface effects, which are by nature not scalable and hence can only provide limited rectification in materials at the macroscopic scale. Carbon, as well as boron-nitride, nanotubes and nanoribbons have garnered substantial interest in heat transport studies due to exotic heat conduction behavior stemming from

their reduced size, but building macroscopic devices from many ordered nanotubes or nanoribbons remains difficult.

In our work, we also hoped to capitalize on reduced dimensional heat conduction properties to yield thermal rectification. Here, the samples fabricated and measured were etched porous silicon wafer pieces in the shape of a lattice of dendrite structures. The etched surface was similar in shape to a forest of pine trees, but on the nanometer scale. The core motivation for expecting thermal rectification in such a structure is based on preferential ballistic phonon scattering through the structure's branches. That is, ballistic phonons traveling along one direction of the structure will easily enter into the branches and thus have a longer path of conduction (and consequently a lesser thermal conductivity) as they scatter multiple times in the branches before continuing down the central structure of the dendrite. If traveling in the opposite direction, the phonons will less preferentially enter the branch structures, causing a shorter path of conduction [134]. Figure 4.1 illustrates this rectification method. In order for heat transport to occur primarily by ballistic phonons, the branching structures must have widths less than the mean free path of the phonons, requiring nanometer scale structures when made from silicon. Though phonon mean free path lengths in silicon vary with doping, in general around 300 K silicon mean free paths are $\approx$ 100 nm [22] while increasing with decreasing temperatures to several microns around 10 K [79].

While it seems reasonable that the geometric effects of such dendrite structures would lead to thermal rectification when in a ballistic phonon conduction mode, developing a strong theoretical model to support it is difficult. Thermal conduction models of nanoscale structures have been difficult to verify experimentally [21, 24, 78, 110] and can only be analytically performed on relatively simple structures or lattices with periodic deformities. By the nature of the dendritic structures used in this study, the disorder is far too great to hope for analytical solutions, at best Monte Carlo simulations could be attempted but even in those it would be difficult to replicate the nature of these structures as the etching process is not well understood [13, 66, 86, 108] and yields

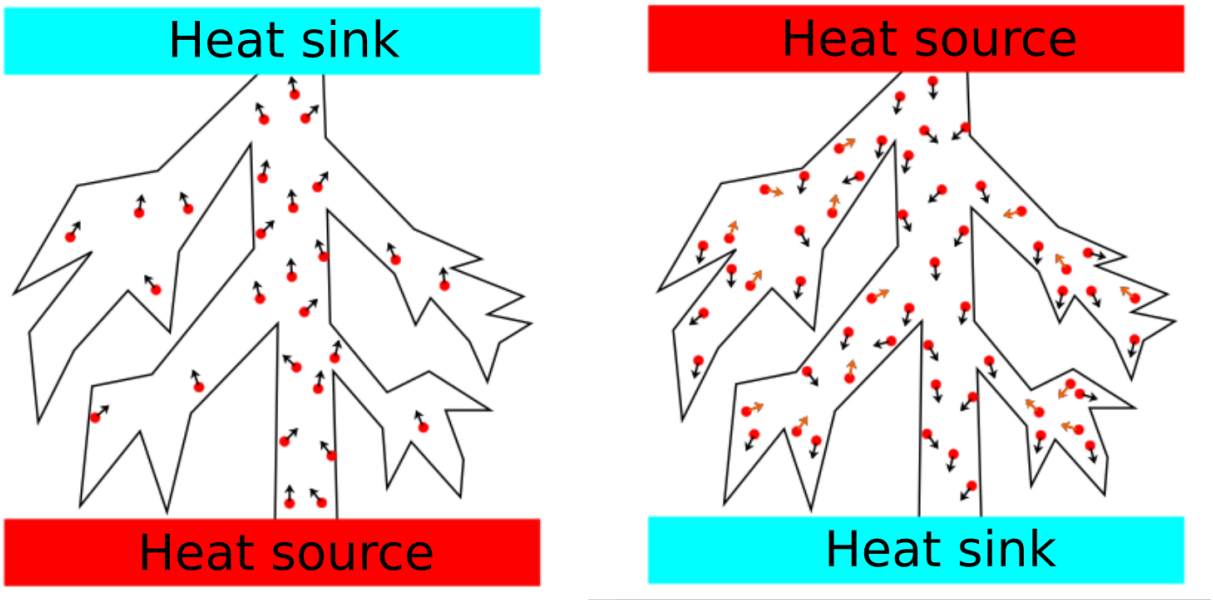

Figure 4.1: Cartoon of thermal rectification arising from preferential ballistic heat conduction. Phonons which are traveling down branches are forced to double-back (orange arrows) to ultimately reach the heat sink. The longer phonon conduction path result in lower thermal conductivity compared to the opposite orientation.

structures with a non-negligible degree of randomness.

A theoretical thermal rectification study, similar in principle to dendritic structures, was performed on sawtooth structures [133] and predicted rectification of 24% at 300 K in silicon. A similar theoretical study on sawtooth nanostructures examined effects of the average temperature and aspect ratio (total structure height divided by tooth to tooth width) on thermal rectification in sawtooth structures and found rectification was maximal for larger aspect ratios and lower average temperatures [109].

Etching silicon into these dendritic forms was accomplished by an electrochemical etching method. The etching agent was hydrofluoric acid diluted in an anhydrous solvent. The etching process required bath temperature management, continuous electrical control, and physical agitation of the bath. Subtle changes in any of these parameters can yield a great variety of porous structures,

though the etching method we employed resulted in dendrite structures with ”trunk” thicknesses around 20 nm and ”branch” thicknesses around 10 nm.

4.2 Principles of Electrochemical Etching of Silicon

The process of electrochemically etching silicon attracted a lot of interest in the 1990's due to the discovery of visible wavelength photoluminescence in porous silicon [19] arising from quantum confinement of photoexcited carriers in such structures. Though there is a multitude of different pore geometries which can be made by electrochemical etching and while the process of pore formation is still not fully understood, several guidelines have been found to be generally true and are as follows.

The etching process requires an electrolytic HF solution under external bias which causes partial dissolution of silicon as follows [7, 30, 65]:

$$Si + 6HF \rightarrow H_2SiF_6 + H_2 + 2H^+ + 2e^-$$

As hydrogen is released during this reaction, bubbles forming on the silicon surface must be managed to allow the reaction to proceed unencumbered. This is often done by stirring the solution throughout the reaction either through closed circuit pumping or, as in our case, by rocking the system. Wettability is another factor which must be managed as HF is generally produced in 49% aqueous solution and clean silicon is hydrophobic. A surfactant, most commonly ethanol, is added to enable the solution to penetrate the pores.

There are two main families of HF electrolyte solutions used to etch different porous silicon morphologies: aqueous electrolytes and organic electrolytes [33]. Aqueous electrolyte solutions contain only water, a surfactant, and HF or fluorine bearing salts. Organic electrolyte solutions contain HF, a surfactant, and an organic solvent, most commonly acetonitrile, dimethylformamide,

An increase of ... yields	Porosity	Etching rate	Critical Current
HF Concentration	Decrease	Decrease	Increase
Current Density	Increase	Increase	-
Anodization Time	Increase	Almost constant	-
Temperature	-	-	Increase
Wafer doping (p-type)	Decrease	Increase	Increase
Wafer doping (n-type)	Increase	Increase	-

Table 4.1: Etching parameter effects on porous silicon formation [8]

or dimethylsulfoxide. Aqueous electrolyte solutions posses interesting electrical behavior in that above a certain threshold, often called a PSL peak or critical current, the silicon surface will electropolish rather than etch into porous structures. Backside wafer illumination is also commonly used in n-doped wafers to provide additional electron holes, which are required in the silicon dissolution process. Wafer doping and crystalline orientation, along with electrolyte choice and water content, drive current, temperature, backside illumination intensity (if any), and current duration all determine the morphology of the etched silicon structure.

Porous structures are classified by the width of the average pore; microporous structures have pore widths less than 2 nm, mesoporous structures have pore widths between 2 nm and 50 nm, and macroporous structures have pore widths greater than 50 nm. Porosity is a common metric of porous structures which is a measure of the empty space within the structure, expressed as a fraction between 0 and 1. Porosity is found by mass measurements prior to etching (m_1), after etching (m_2), and after rapid removal of the porous structure (m_3) as (m_1-m_2)/(m_1-m_3). Table 4.1, reproduced from the excellent review by Bisi et al [8] (Reprinted from Surface Science Reports, Vol 38, O. Bisi, S. Osscini, and L. Pavesi, Porous silicon: a quantum sponge structure for silicon based optoelectronics, Page 13, Copyright 2000, with permission from Elsevier), shows how porosity is effected by HF concentration, current density, anodization time, temperature doping type, and doping level.

The choice of etching parameters for this work were based on the application on these principles experimentally, building on unpublished experiments made by our collaborators at MicroXact. In the case of the work presented here, n-doped <111> wafers were etched using an organic electrolyte containing acetonitrile without illumination to produce the desired dendrite structures. The optimal dendrite branch sizes were chosen to be on the order of the phonon mean free path in silicon, see Table 4.2, and was found to be of mesoporous scale. The choice of wafer doping, electrolyte, and current density were made based on previous works which found them to produce dendritic mesoporous structures [67].

The selection of wafer crystalline orientation defines the etch pore orientation. The Etch pores of n-doped wafers, including the dendrite structures etched by our method, develop along the [100] plane [111]. In order to achieve maximal rectification, the dendrite structures must be parallel to the heat conduction path, which is the normal axis of the substrate wafer. Consequently <111> wafers were chosen as the [100] plane of <100> wafers is parallel to the normal axis of the wafer.

4.3 Electrochemical Etching Method to Produce Dendritic Silicon Nanostructures

Six n-doped silicon <111> wafers with resistivity of 0.018-0.02 $\Omega\mathrm{cm}$, 150 mm diameter, and 525 $\mu\mathrm{m}$ thickness, were etched over the course of the work and of those, three were deemed to be of sufficient quality to be measured for thermal rectification. Refinement of the etching process, which was built upon earlier work at MicroXact, occurred over the trials until samples with the desired geometries were readily producible. In short the sample handling method was as follows: prior to etching, the sample wafer was first precleaned, then the backside electrode contact film was deposited on the wafer, and, immediately prior to submersion in the etch bath, the native oxide

layer of the wafer was removed.

Once the etch was complete, the wafer was cleaved and one piece was then installed in the thermal rectification measurement system and pumped down to vacuum, while another was taken for scanning electron microscope (SEM) imaging. As the etching process typically required a full day of work, samples were most often imaged the day following etching. If the sample was found to posses the desired dendrite structures, a full thermal rectification measurement was then initiated. Remaining wafer pieces were stored in the evaporator vacuum chamber, away from the evaporation surfaces, and kept at $\approx 1\mu$Torr to retard oxidation.

After initial etches with the system, we found the dendrite structures were being thermally damaged by the exothermic reaction that produced them. To counter this, we needed to manage the etch bath temperature over the etching period and did so with the addition of chiller lines. In order for the chiller lines to be able to withstand the harsh environment of the etch bath, they were made of a flexible, convoluted, PTFE tube. Half-pipes were cut into the chamber wall at the lid connection to allow chiller line passage. Inside the reaction chamber, the PTFE tube was secured by PTFE brackets, themselves secured by PTFE screws, around the inside perimeter, as shown in Figure 4.2 while a depiction of the fully-assembled etching system is shown in Figure 4.3.

The temperature of the etch bath solution was monitored manually by a PTFE coated dial thermometer that was inserted through a tight-fitting hole in the chamber lid. Outside of the reaction chamber, plastic tubing wrapped in an insulating foam sleeve connected the lines to the chiller. The chiller bath was a 50/50 mix of water and ethylene glycol.

Wafer precleaning was done by the RCA clean method. In the first stage, the wafers were submerged in 5 DI water : 1 NH_4OH (29%) : 1 H_2O_2 (30 %) at 75 °C for 10 min and afterwards the wafers were rinsed with DI water and blown dry. Next they were submerged in 6 DI water : 1 HCL (37 %) : 1 H_2O_2 (30 %) at 75 °C for 15 min and afterwards rinsed with DI water and

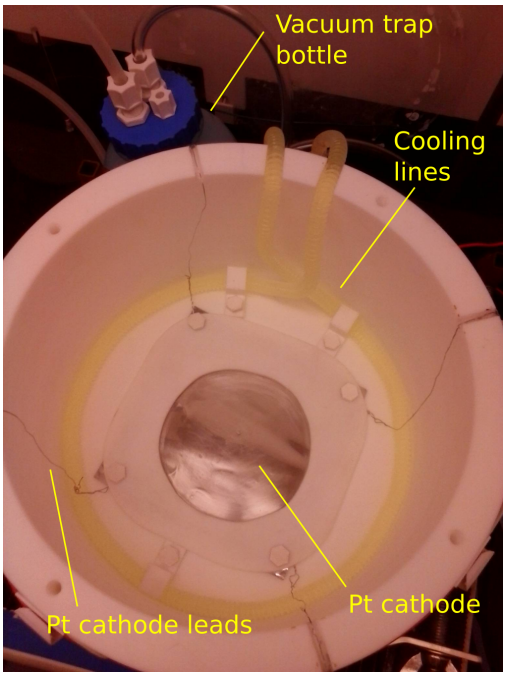

Figure 4.2: Silicon etching chamber with chiller lines.

blown dry. Immediately after this cleaning the backside electrical contact layer was deposited with e-beam evaporation on the unpolished face with 5 nm Cr followed by 50 nm Au. The prepared wafers were then stored in an appropriate wafer container for up to several weeks prior to etching.

Immediately prior to etching, the native oxide layer of the wafer was removed by submersion in 4 DI Water : 1 HF (49%) for 2 min in a PTFE wafer container. After oxide removal, the wafer was transferred immediately to the etching chamber and etching was commenced. The sample wafer was held in place by a vacuum volume between two o-rings (see Figure: 4.3). The vacuum line went from the chamber to two trap bottles and then to the building's vacuum inlet. The two trap bottles served as a redundant safety precaution. If HF were to get into the vacuum line, for instance if the sample breaks, then the trap bottles would prevent it from being pumped into the building's vacuum system. Note that all HF work was performed in the fume hood located at ICTAS II room 151, with full personal protective equipment (PPE) donned at all working times. The HF PPE consisted of closed shoes, long pants, a fully buttoned up lab coat, a Neoprene apron,

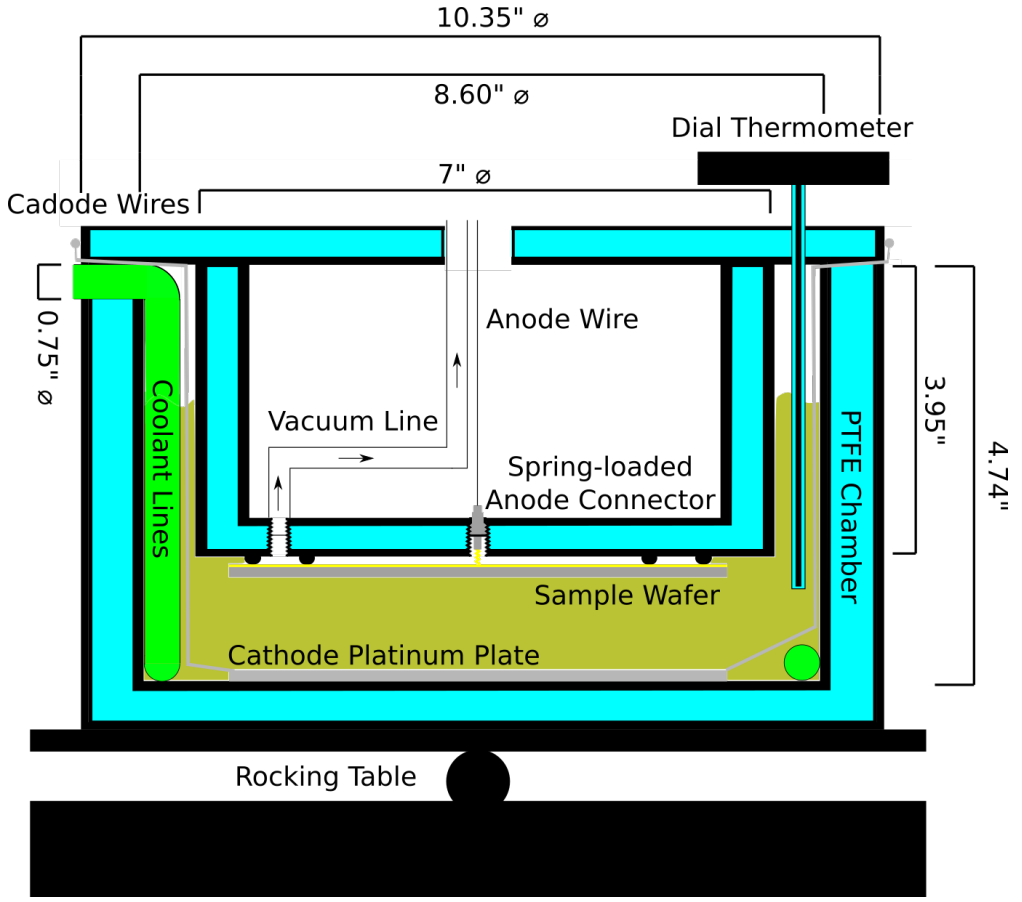

Figure 4.3: Silicon etching chamber diagram.

Nitrile gloves worn under 0.5 mm thick Nitrile long gloves, safety goggles, and a face mask. Other safety precautions included: Calcium gluconate gel kept in the first aid kit of the lab, a spill kit, and baking soda to help neutralize spills and waste.

The etch bath was composed of 600 mL acetonitrile, 60 mL ethanol, and 300 mL (49%) hydrofluoric acid mixed in that order. Acetonitrile was extracted from its sealed bottled by means of inserting two long syringes through its cap membrane, one of which was connected to a tube which ran to a large graduated beaker and the other connected to a pressurized nitrogen line. Extracting it in this manner prevented water contamination of the acetonitrile. After an etching session, the bath was recovered using a peristaltic pump with PTFE tubing and kept in a polypropylene jug which

was then chilled in a refrigerator. When stored in this matter, etch baths were found to be reusable up to two additional times without significant detriment to the etched structure. It should be noted that gold flakes would break free of the wafer in the area outside of the outermost o-ring during the etching process. When recovering the bath at the end of the etch, a small amount of those flakes would be incidentally kept in the bath, but this did not affect the process.

Once the electrolyte etch bath was added to the chamber, the chamber lid with mounted wafer was lowered into the bath and screwed in place. While under gentle rocking, the etching occurred over 2 hours with a constant current set at 0.596 A which resulted in 7.36 $\frac{\mathrm{mA}}{\mathrm{cm}^2}$ over the 4" diameter wafer. In practice however, the two power supplies that were tried in separate attempts were unable to reliably hold constant current and manual adjustments were necessary over the etching period. Bath chilling was done by setting the chiller initially to -30 °C, but once the temperature reached 0 °C resetting to -10 °C, which kept the temperature near 0 °C for the duration of the etch.

Once the etch was complete, residual etchant needed to be rapidly removed to prevent additional reactions. To do this, the sample was removed and transfered to a large polyethylene beaker filled with 150 mL of DI water and left there for 2 hr. A plastic rod mounted to a plastic disk was placed in the beaker such that the disk rested on the rim of the beaker and the rod kept the wafer submerged. The wafer was then quickly transferred to a glass beaker filled with 200 mL of isopropyl alcohol for 5 min. Next the wafer was transferred to another beaker containing 50 mL of pentane for 5 min. Finally, the wafer was rinsed with DI water, blown dry with compressed air and stored under vacuum until SEM images could be taken. Note that though this process yielded the desired structures, other groups most often simply rinse the wafer with Ethanol and blow dry after etching.

This etching method typically resulted in a surface that was etched to around 150 $\mu\mathrm{m}$ deep. The bottom third of this depth contained the most ideal dendrite structures, while as structures approached the wafer surface, the more engorged they became until merging into a seemingly amorphous structure just below the wafer surface. Electron micrographs illustrating this are shown in

Figure 4.4.

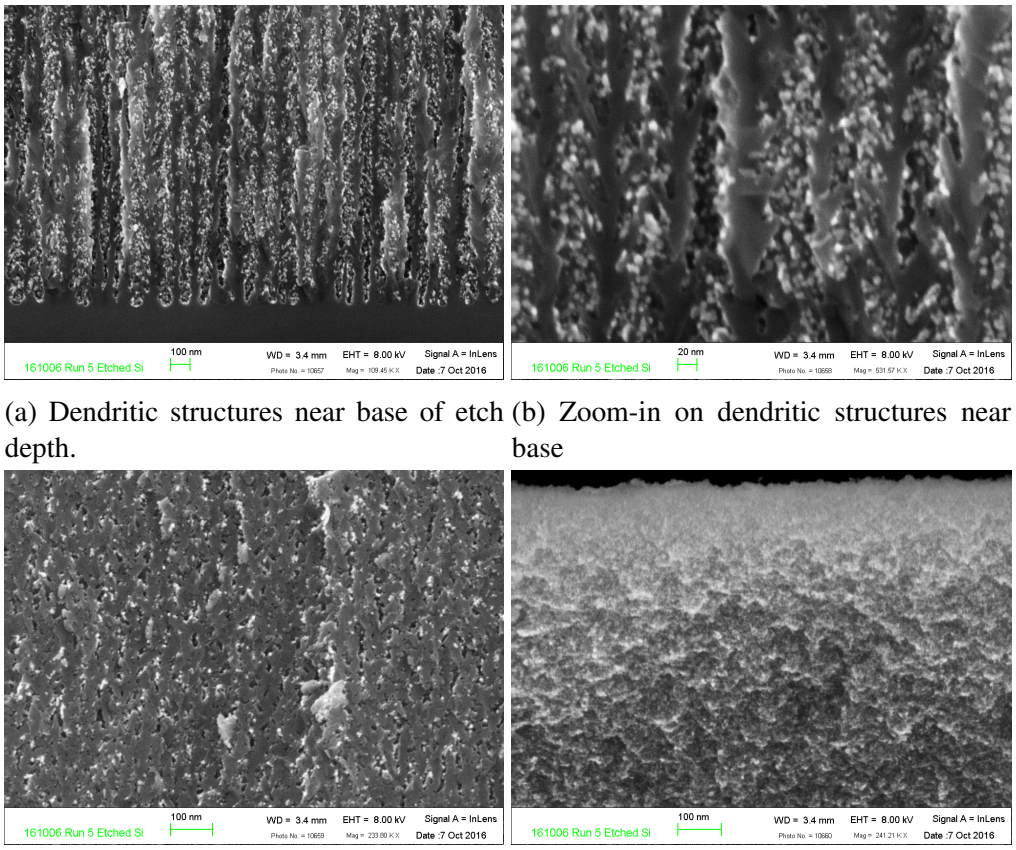

(a) Dendritic structures near base of etch depth.

(b) Zoom-in on dendritic structures near base

(c) Degraded dendritic structures near the middle of the etch depth.

(d) Amorphous-like porous Silicon at wafer surface

Figure 4.4: SEM images of etched porous Silicon dendrite structures.

4.4 Thermal Rectification Measurement System Operating Principles

Fourier heat transport theory, though very accurate at describing heat conduction of macroscopic systems such as the apparatus described below in equations (4.1)-(4.7), breaks down as system size features approach the nanoscale [22, 121]. Fourier's law (Equation (4.1)) is a diffusion based theory, but as the size of the system approaches the mean free path of its phonons, the assumption of

diffusion becomes less valid and ballistic phonon heat conduction becomes more important. Further, temperature and thermal conductivity as concepts are ill-defined in ballistic phonon regimes. Temperature is an equilibrium concept, but when heat conduction is governed primarily by non-interacting ballistic phonons, the phonons kinetically scatter off interfaces, somewhat like billiard balls, rather than thermalization through phonon-phonon and electron-phonon interactions. Temperature gradients are consequently meaningless in such regimes and thermal conductivity is not an intrinsic material property, but depends on the method of heating. For cases between totally ballistic and totally diffuse heat conduction, other theories must be considered as shown in Table 4.2 which is reproduced from Chen's work [22] (Reprinted by permission from Springer Nature: Journal of Nanoparticle Research, Particularities of heat conduction in nanostructures, Gang Chen, 2000 [22]).

Length Scale	Regimes	Photon	Electron	Phonon
Wave Regimes Coherence Length, L photon: 1 μm-1km electron 1-100 nm phonon $\sim$1-10 nm	h $<$ O(L) wave	Maxwell EM theory	Quantum mechanics	Quantum mechanics
	h $\sim$ O(L) partial coherence	Optical coherence theory	Electron coherence theory	Phonon coherence theory
Particle Regimes Mean Free Path, Λ photon: 10 nm-1km electron $\sim$100 nm phonon $\sim$100 nm	h $<$ O(Λ) ballistic	Ray tracing	Ballistic transport	Ray tracing
	h $\sim$ O(Λ) quasi-diffusive	Radiative transfer equation	Boltzman transport equation	Boltzman transport equation
	h $>$ O(Λ) diffusion	Diffusion approximation	Ohm's and Fourier's laws	Fourier's law

Table 4.2: Transport regimes for three common energy carriers: Device characteristic length (such as thickness) is h; O denotes the order-of-magnitude of a length scale; the listed MFP and coherence lengths are typical values but these values are strongly material and temperature dependent.

The fundamental principle guiding thermal rectification measurements for these dendritic structures is that though the thermal rectification properties are predicted to arise from nanoscale asymmetries, the entire wafer structure, including the substrate, structured, and amorphous regions, will manifest observable rectification. Consequently, thermal conductivity measurements of the etched wafer piece, as a whole, in opposing orientations yields an effective measurement of the degree of thermal rectification.

To quantify thermal conductivity of the samples, we must consider Fourier's law:

$$\vec{\mathrm{q}} = -\mathrm{k}\nabla\mathrm{T}. \tag{4.1}$$

Here $\vec{\mathrm{q}}$ is the heat flux density in $\frac{\mathrm{W}}{\mathrm{m}^2}$, k is the thermal conductivity in $\frac{\mathrm{W}}{\mathrm{m-K}}$, and $\nabla\mathrm{T}$ is the temperature gradient in $\frac{\mathrm{K}}{\mathrm{m}}$. In most cases, the thermal conductivity is treated as a constant and in the case of inhomogeneous, anisotropic, or multilayer materials the system is broken down into subsystems where the thermal conductivities are constant to simplify calculations. In our case, the sample is asymmetric, but homogeneous, such that the thermal conductivity is different along opposing directions. In order to measure the degree of thermal rectification of the sample, we designed a system that established a specific heat flux along the axis of rectification, then measured the resulting temperature difference, and repeated the measurement for the same heat flux magnitude in the opposite direction. From such a pair of measurements, the thermal conductivity of each orientation was obtained and then compared to determine if rectification was occurring. While this method is conceptually simple, experimental considerations required a more complex approach.

Essential to the measurement of thermal rectification is symmetry in the measurement and the maintenance of constant average sample temperature over the course of the measurement. If the system has a built-in asymmetry in thermal conductivity or heat capacity, then establishing equivalent heat flux across the sample would be difficult. One option considered was to build a system that allowed heat to flow in one direction, from a single heater through the sample to a single heat sink. The sample would then be measured in one orientation, dismounted, inverted, and remounted prior to a second measurement. Preliminary measurements taken with this configuration proved to have difficulty with measurement-to-measurement repeatability, as control measurements showed non-negligible differences in thermal conductivity between orientations for non-etched silicon. These errors likely resulted from subtle run-to-run differences in the mounting process, such as

different amounts of applied thermal grease or differences in the pressure applied by the mounting screws.

For this reason, we designed and built a symmetric setup that allows us to reverse the heat flow without remounting the sample. In this design, heater and thermometer elements were mounted on both sides of the sample and those elements where both connected by independent legs to the heat sink. This allows for equivalent heat fluxes to be established across the sample for opposite orientations provided that each leg of the system is of known thermal resistance and capacitance without needing to warm the system and remount the sample. An illustration of the configuration is shown in Figure 4.5.

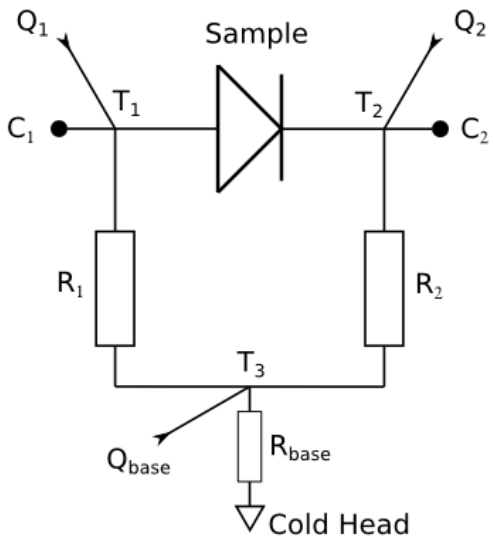

Figure 4.5: Diagram of the thermal rectification measurement apparatus. Q's represent the heat produced by resistive heating elements, T's represent the temperatures as measured by Pt resistance temperature detectors, C's represent the heat capacity of the system legs, and R's represent the legs' thermal resistance

To obtain the thermal conductivity of the sample we will need to know the heat flowing through the sample (Q_S) and the resulting temperature difference ΔT. To understand how the heat flow through the sample is obtained in this configuration, we will walk through a single measurement.

If we set each of the heaters to some values such that $Q_1 > Q_2$ and define the heat flowing through each leg as $Q_{R_{1,2}}$ then we can have that:

$$\begin{aligned} Q_1 &= Q_{R_1} + Q_S + \frac{dT_1}{dt} C_1, \\ Q_2 &= Q_{R_2} - Q_S + \frac{dT_2}{dt} C_2. \end{aligned} \tag{4.2}$$

Now, if we assume that both legs have the same heat capacity (easily feasible with appropriate machining) then we can simplify Equation (4.2) to:

$$\begin{aligned} 2Q_S &= Q_1 - Q_2 + Q_{R_2} - Q_{R_1} + \frac{dT_1}{dt} C - \frac{dT_2}{dt} C, \\ &= \Delta Q + \frac{d\Delta T}{dt} C + Q_{R_2} - Q_{R_1}. \end{aligned} \tag{4.3}$$

To proceed further with this line of thought, we need to examine the heat flowing through sample and legs individually:

$$\begin{aligned} Q_S &= R_S^{-1} \Delta T, \\ Q_{R_1} &= R_1^{-1} (T_1 - T_3), \\ Q_{R_2} &= R_2^{-1} (T_2 - T_3). \end{aligned} \tag{4.4}$$

Now if we also assume that both legs have the same thermal conductance $R_1^{-1} = R_2^{-1} = \sigma_L$, which is also a fair approximation with appropriate machining, we can take the difference of the two leg heat flows:

$$Q_{R_1} - Q_{R_2} = \sigma_L \Delta T. \tag{4.5}$$

We may also express σ_{L} through the averages of the hot and cold side temperatures and heat flows:

$$\sigma_{\mathrm{L}} = \frac{\bar{\mathrm{Q}} - \mathrm{C}\dot{\bar{\mathrm{T}}}}{\bar{\mathrm{T}} - \mathrm{T}_3}, \qquad \begin{aligned} \bar{\mathrm{Q}} &= \tfrac{\mathrm{Q}_1 + \mathrm{Q}_2}{2}, \\ \bar{\mathrm{T}} &= \tfrac{\mathrm{T}_1 + \mathrm{T}_2}{2}. \end{aligned} \tag{4.6}$$

Combining this equation with Equation (4.3) we obtain an expression for the sample thermal conductivity:

$$\begin{aligned} \sigma &= \frac{\mathrm{Q_S}}{\Delta \mathrm{T}} = \frac{1}{2}\Big(\frac{\Delta \mathrm{Q} - \mathrm{C}\Delta\dot{\mathrm{T}}}{\Delta \mathrm{T}} - \sigma_{\mathrm{L}}\Big), \\ \kappa &= \sigma\Big(\frac{\mathrm{L}}{\mathrm{A}}\Big). \end{aligned} \tag{4.7}$$

Here L is the thickness of the sample and A is the cross-sectional area of the sample.

4.5 Thermal Rectification Apparatus and Methods

As it is believed that the degree of thermal rectification for silicon dendrite structures would be greatest at cryogenic temperatures due to increasing phonon mean free path at lower temperatures and consequent promotion of ballistic phonon heat conduction, a cryostat chamber was constructed to test the samples. Cooling was supplied to the chamber by a water-cooled He compressor system (Oxford M400) and vacuum was maintained by a rough (scroll) and turbo pump station. In the lab, we had two chillers (Thermo-Neslab Merlin M75 and M150) neither of which could by itself supply sufficient cooling for sustained compressor usage. To counter this we constructed a heat exchanger to allow the cooling power of both chillers to be combined. The heat exchanger consisted of two independent copper tubing lines coiled around each other inside of a sealed bucket which was filled with water and equipped with a thermometer. The smaller chiller (M75) supplied chilled water flow through one of the coils and consequently cooling the heat exchanger bath,

while the other coil was connected such that waste heated water flowed from the compressor into the heat exchanger, and then to the larger capacity (M150) chiller before being pumped back into the compressor. This equipment configuration is illustrated in Figure 4.6.

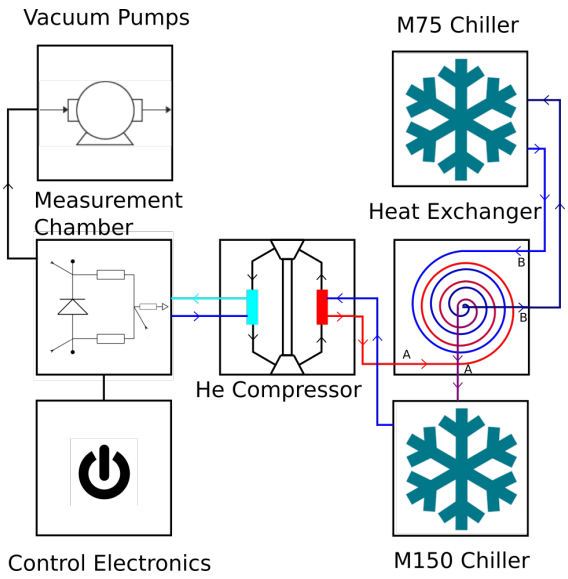

Figure 4.6: Heat, vacuum, and electronics configuration of thermal rectifiction measurement apparatus.

This configuration provided ample cooling, but the combined waste heat of the compressor and chillers overheated the room that housed the equipment. To solve this new problem, we added sufficient copper tubing to move the more powerful chiller (M150) to a larger, adjacent, teaching lab.

Once the equipment was able to operate as intended, control measurements were undertaken. Over the course of several control measurements, modifications were made to the system until ultimately arriving at the two leg bridge design described above. In the final design, the sample mount was enclosed in a heat shield made of aluminum plates which were anchored to the base (cold head) plate. This minimized parasitic heat conduction paths not accounted for in the derivation in Section 4.4. A model and image of the sample chamber is shown in Figure 4.7.

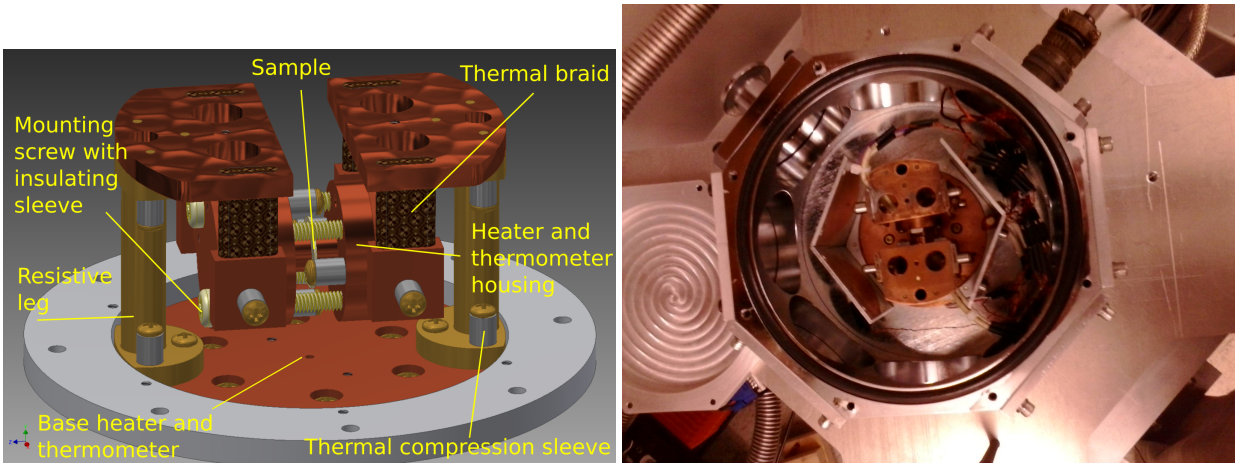

(a) Model of thermal rectification measurement apparatus

(b) Picture of the thermal rectification apparatus chamber. Heat shield partially in place

Figure 4.7: Thermal rectification measurement apparatus

The base plate of the system was made from Cu and mounted to the cold head of the He compressor with brass screws. Thermal grease (Apiezon N) was applied between the base plate and the cold head to improve heat conduction. Two resistive heating elements were epoxied inside of the base plate in symmetric positions and electrically connected in parallel. These heaters served to counter the cooling of the cold head to enable measurements at temperatures other than the base temperature of the cold head, and the pair was labeled ”Heater 3”. A Pt resistive thermometer diode (PtRTD) was installed in the base plate with thermal grease and labeled ”CH3”. The two brass legs of the system were designed to be thermal resistive elements with resistances similar to that of early (highly oxidized) samples. In order to match those resistances, the legs were made from brass tubes of specific length and thickness from which thermal resistance could then be calculated. After fabrication, the leg thermal resistances were measured and found to agree with calculations reasonably well as described below. The legs consisted of brass feet silver soldered to both ends of brass tubes. Each leg was screwed to the base plate and overhang piece with brass screws using steel sleeves. Since the thermal contraction of the steel sleeves is less than that of the brass screws, the screw connections became tighter at lower temperatures, minimizing interface

thermal resistance. Sleeve and brass screw connections were used throughout the system. Thermal grease was applied between the legs and the base plate and woods metal was used to adhere the legs to the overhang pieces.

Connecting the sample to each of the system legs with sufficient pressure to maintain good thermal contact was not straightforward in this configuration. If metal screws were directly used then the screws would provide an alternative heat flow path, rather than through the sample, which would complicate the measurement. Initial attempts to bypass this issue involved using screws of low thermal conductivity, ceramics and then Nylon. Due to the large range of temperatures that the system would operate over, thermal contraction of the system halves substantially weakened or even broke thermal contact with the sample if the halves were directly screwed together over the sample with non-metal screws. To circumvent this, some flexibility was added to the mount in the form of copper thermal braids. Each side of the sample heater/thermometer piece was connected to an overhang shelf with two such thermal braids. The braids themselves were soldered to Cu plates that enabled them to be tightly screwed to the overhang and heater/thermometer pieces, with thermal grease between such connections. After several measurements with both Nylon and ceramic sample mounting screws, we found that they both often would break regardless. Ultimately, brass screws with thermally insulating Mica shoulder sleeves proved to be a sustainable mounting solution.

The sample thermometers, also PtRTDs, were mounted in copper housings, see Figure 4.7(a), with epoxy and were referred to as ”Ch1” and ”Ch2”. Resistive heater elements were epoxied in the same pieces as the sample thermometers and referred to as ”Heater 1” and ”Heater 2” corresponding to their paired thermometers. In practice, temperatures were calculated from resistances measurements of the PtRTDs by means of established reference curve known as the temperature curve. The PtRTD temperature curves were calibrated over the system’s operational temperature range.

For the thermal rectification measurements described here, absolute accuracy of the temperature was not of the highest importance. Rather, as shown in Equation (4.7), the difference in temperature between the thermometers is what must be known. In order to obtain accurate difference measurements, the thermometers must be calibrated such that their measurements agree well when the thermometers are at the same actual temperature. To achieve this, the two heater/thermometer Cu pieces were screwed directly to the base plate with a thermal grease coating in between. The legs were removed and the system was cooled to ≈ 50 K and slowly heated back up to 300 K using heater 3 while recording the resistances of the PtRTDs. Assuming that all thermometers of the system were at the same temperature in this configuration throughout the heating, new temperature curves were made such that resistances measured in Ch2 and Ch3 were defined as corresponding to the temperature recorded by Ch1 using its factory default temperature curve. This calibration was used in all subsequent measurements.

The heat capacity and thermal resistance of each leg of the system were also measured to verify agreement with the design parameters. To measure these parameters, the system was installed and cooled as per a normal measurement, except that no sample was installed and the legs were not affixed to each other directly. In this configuration, each leg can be treated as individual 1-dimensional heat flow paths. Consequently, the temperature difference across this conduction path (between the leg's sample thermometer and the base plate thermometer) is governed by

$$\Delta T_{SB} = R(Q_S - \dot{T}_S C). \tag{4.8}$$

Here, ΔT_{SB} is the temperature difference between the sample and base plate thermometers, R and C are the leg's thermal resistance and heat capacity respectively, Q_S is the heat applied at the sample plate, $\dot{T}_S$ is the rate of temperature change of the sample plate thermometer. From this principle, we obtained each leg's thermal resistance by measuring the stabilized temperature dif-

ference resulting from constant heating. Heat capacity was obtained from fitting the non-stabilized temperature difference curve with Equation (4.8) using the resistance found from the stabilized result. Using this method, the thermal resistance of each leg of the system were measured to be 64.0 $\frac{\mathrm{K}}{\mathrm{W}}$ in the Ch1 leg and 63.0 $\frac{\mathrm{K}}{\mathrm{W}}$ in the Ch2 leg around 80 K. Leg heat capacities were measured to be 22 $\frac{\mathrm{J}}{\mathrm{K}}$ in the Ch1 leg and 18.5 $\frac{\mathrm{J}}{\mathrm{K}}$ in the Ch2 leg around 80 K. It should be noted that both thermal resistance and heat capacity are dependent on temperature and so these measurements are not applicable to the entire temperature range used in this study. However, Equation (4.7) is expressed in terms of C and not R and, further, its only C dependence is multiplied by temperature change rates. Consequently, as the system approaches stabilized temperature conditions, the thermal conductivity measurement's dependence on C approaches zero. With this principle in mind, we found that applying varying heat capacity values at different temperatures had a negligible impact on the stabilized thermal conductivity measurements and so the 80 K heat capacity measurements were used in all measurements.

The samples themselves were cleaved into shapes of approximately equal area to the sample contacts (0.5 cm^2). As the samples were most often made from Si <111>, accurate cleaving of such areas was difficult, so the sample area was often larger or smaller and in a variety of shapes. The cleaved sample were photographed with a reference ruler and the sample surface area was measured from the photographs. The sample geometry influences the thermal conductivity measurement as stated in Equation (4.7). However, the effective geometry that heat traverses is more important than the absolute geometry of the sample. In the case of samples with surface areas larger than that of the contact heads, the area of the contact heads was used as little lateral heat flow in the sample can be assumed. In instances where the sample surface area was smaller than that of the contact heads, the true sample surface area was used. In all cases, the sample was mounted with a thin layer of thermal grease on either side.

In measuring the thermal conductivity of the sample, stable, or at least slowly varying, temperature

differences across it and the legs of the system needed to be reliably established. While Equation (4.7) accounts for changing temperature differences, it does so using the heat capacity of the system, which is a measured value subject to error and temperature dependence. In the limit of a constant temperature difference, this heat capacity dependence vanishes and in doing so, reduces the uncertainty in the measurement.

Setting a heat differential across the sample using the sample heaters and allowing the resultant temperatures to stabilize would be sufficient for a single measurement, but this would yield information only on the effective thermal conductivity at that temperature which could be subject to alternate rectifying effects, such as thermal strain differences at interfaces. A property that differentiates rectification resulting from ballistic phonons in these dendritic structures, contrary to interface rectification effects, is that in ballistic heat conduction rectifiers the degree of rectification depends on the average sample temperature ($\bar{T}$) and not the magnitude of the temperature difference (ΔT), provided heat conduction remains ballistic. This is contrary to the case of rectification resulting from such an interface effect where the degree of rectification scales with ΔT. So, to be certain that observed rectification resulted from non-interfacial effects, several thermal conductivity measurements were taken at the same average sample temperature but with different values of ΔT. This was done by keeping the total heat output of the two sample heaters constant over a set of measurements at the same $\bar{T}$, but with increasing ΔT values over the individual measurements as shown in Figure 4.8. This measurement process was then repeated at different average sample temperature values, which effectively correspond to measurements at different phonon mean free path lengths and is illustrated in Figure 4.9. Recall that phonon mean free paths in silicon decrease with increasing temperature, and so rectification should be reduced as average sample temperature increases.

To be clear about the measurement language, some of the key terms are as follows. A *step* refers to the individual thermal conductivity measurement at a single temperature difference in one orienta-

tion. A *cycle* is the series of steps which occur over a single average sample temperature, but with differing ΔT values. A *run* refers to the series of cycles taken in one session generally differing in the average temperature $\bar{T}$, without venting the system. An example illustrating a single average sample temperature measurement cycle is shown in Figure 4.8 and an entire sample measurement run, without the initial cooldown period, is shown in Figure 4.9.

Prior to and upon completion of a cycle of thermal conductivity measurements, the sample heaters were set to the same heat output and sample temperatures were allowed to stabilize. These "before" and "after" measurements were compared to determine the amount of average temperature drift over the course of the measurement, which could have been caused by irregularities in the cooling or base (Ch3) heating. Differences between Ch1 and Ch2 at these steps, in which there should be no thermal gradient, were attributed to differences in heat conduction to the thermometers, likely arising from the thermometer mounting. This was corrected for by multiplying Ch2's temperature measurements by a correction factor which caused the thermometers to match at these equal temperature steps.

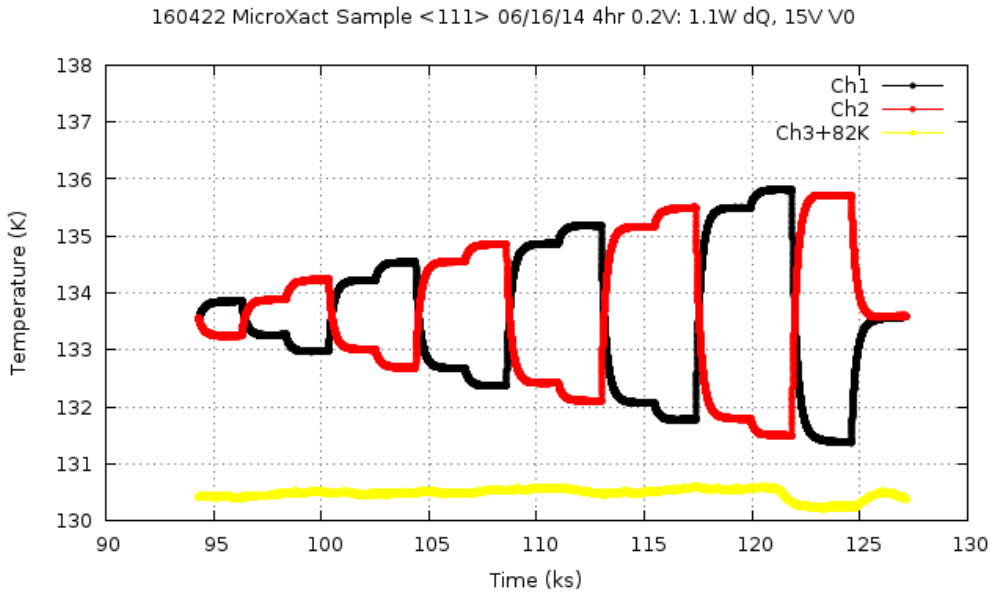

Figure 4.8: Example thermal rectification measurement cycle of a single average sample temperature

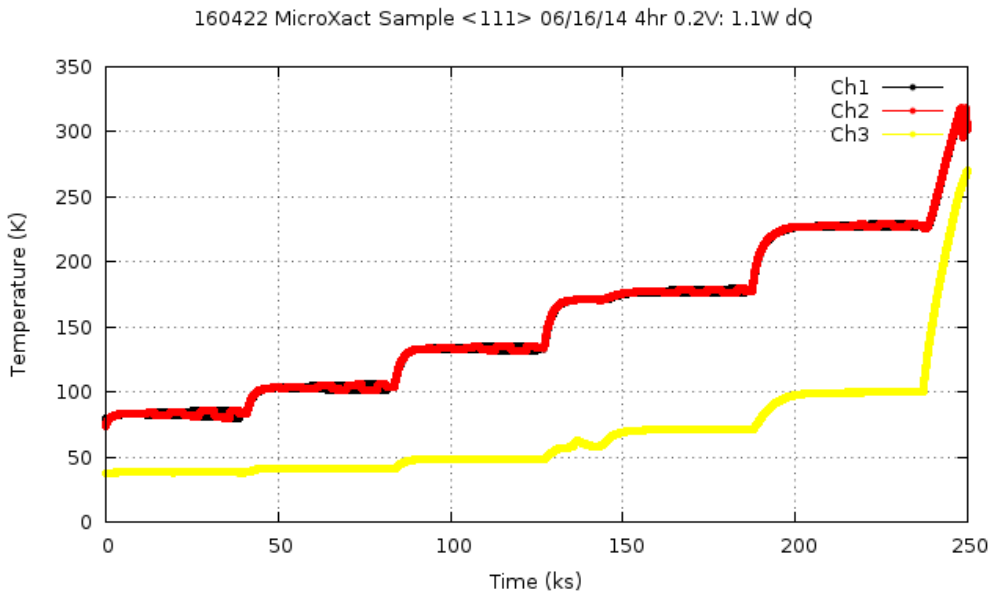

Figure 4.9: Example full run of thermal rectification measurements of a single sample

As is apparent from the timescale of Figure 4.8, a single measurement cycle at one average temperature measurements took several hours. Further, multiple measurement cycles were carried out over the course of a single run to limit the potential for thermal cycling to change the thermal conductivity of the system by means of weakening connections. This approach then required days of continuous runtime for each sample.

The direction of heat flow through the sample is not reversed after each step stabilization but rather a single orientation is allowed to stabilize and then that same orientation is continued to the next heat step before switching. This was done to reduce the runtime of the measurement cycle. Smaller temperature changes require less time to stabilize and so stepping in this manner minimizes the stabilization time while still switching the direction of heat flow once for each power difference setting.

In order to maintain reliable control over the system for long time periods, all measurement were operated by a Labview program that was updated as the work progressed to accommodate new con-

trol schemes. The Labview programs used for these measurements were the ThermalDiodeMKX.vi series, where in place of X was an integer indicating the version of the code. The final version of the series (MK21) is provided in the online supporting files. The final version of the code was able to take measurements over any number of average sample temperatures with any number of heating steps per measurement cycle, with redundant safety features that would fully shut down the system if vacuum was lost or if the temperature of any system thermometer read in excess of 100 °C. Average sample temperatures were not directly set, as this would have required feedback control systems, such as PI or PID, with tuning dependent on each sample's thermal properties. Instead, the program inputs were a baseline power supply voltage setting for each average sample temperature measurement cycle and the desired maximum power difference between the two sample heaters. The baseline voltage setting determined the average power output of the heaters, while the maximum power difference setting determined the deviations from that average that the heaters would take on individual steps such that the maximum power difference occurred on the final step of the cycle and the other steps would be of evenly distributed lesser power settings. This heating scheme is described in detail below.

Analysis of the measurements was automated by means of two Python scripts. The first script (ThermalDiodeThermometerCorrecter180626.py) converted the measured thermometer resistances into temperatures through the most recently calibrated temperature curve. This was done in post processing rather than through the RTD monitor (a SIM923) so that alternate calibrations could be applied to pre-existing datasets when appropriate. The second analysis script (ThermalConductivityCalc180626.py) calculated thermal conductivity values from measured temperatures and heating powers of each step of every measurement cycle in the run, using corrected output from the first script. To do this, the script found the average and standard deviation of temperatures measured over a period of, typically, the final 1000 s of a single heating step. Then those values were plugged into Equation (4.7) to yield thermal conductivity values for each step with errors calculated from

the standard deviations observed in the thermometer temperatures. The results were then plotted, and an example of such a plot is shown in Figure 4.10, while the full set of measurements taken for that sample over its entire measurement run are shown in Figure 4.11.

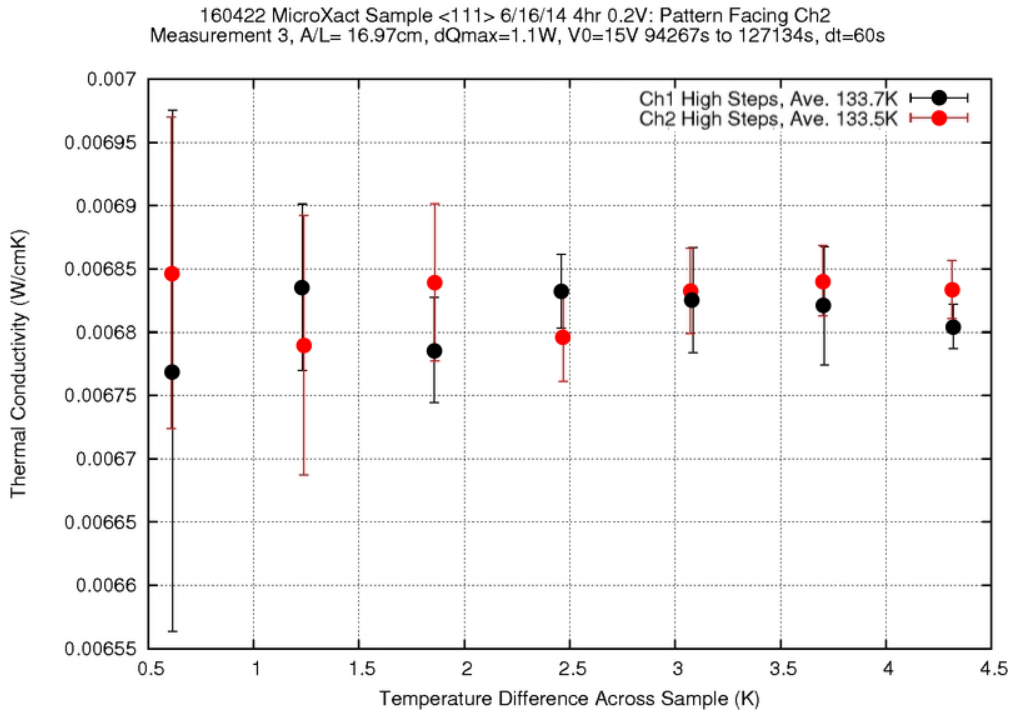

Figure 4.10: An example analyzed thermal rectification measurement at a single average sample temperature cycle

The experimental implementation of these thermal conductivity measurements through steps, cycles, and runs is not straightforward. Average sample temperatures and temperature differences were not directly set, as heat flows in the system were established through the balancing of heater outputs and the cooling power of the He compressor. Heater output was effectively controlled programically through power supply output settings. The He compressor possessed no external control and though its cooling power remained mostly stable, power fluctuations in the building sporadically varied the cooling power. The finer details of the experimental method which achieved these thermal conductivity measurements are as follows.

Sample heating was automatically started with a preset delay after cooling was begun to ensure

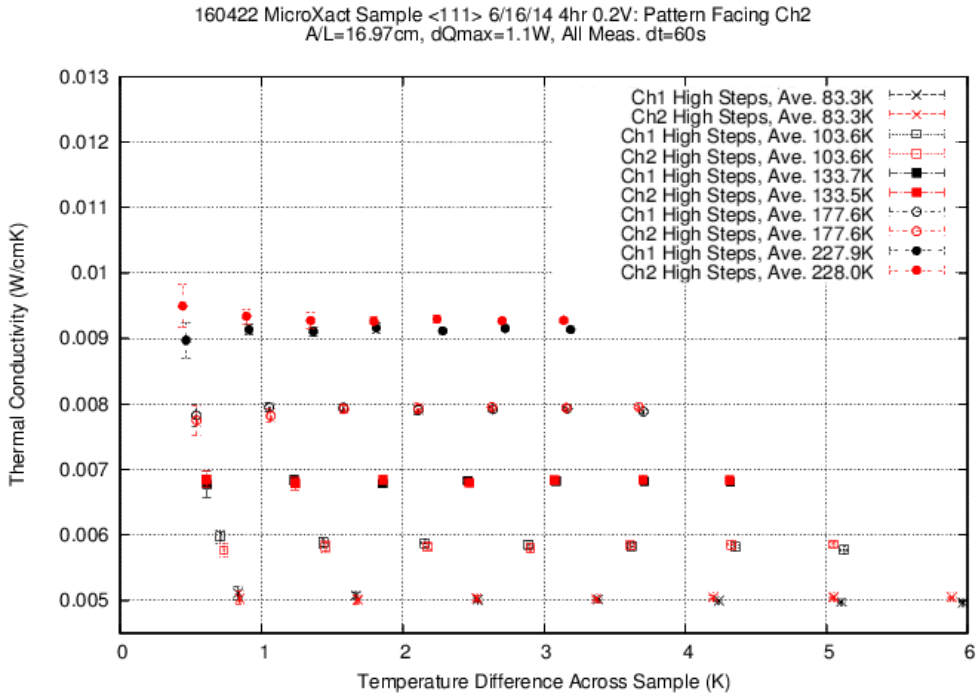

Figure 4.11: An example thermal rectification measurement compilation of a run

that the system had reached its stable base temperature. The run parameters were the maximum power difference across the sample, number of steps, baseline voltage setting of each measurement cycle, integration time, stability threshold, and switching delay. The voltage setting of the analog power supply which powered the Ch3 heaters was set manually, without direct Labview control. To enable some measure of automatic control over the analog power supply, its output was connected to the system through a relay, itself controlled by the program, which completed the circuit after the delay time had expired.

Additional choices that defined the measurements were the number of step pairs in a cycle, the temperature differences of each step, the number of cycles in the run, and the average sample temperature for each cycle. The temperature difference of each symmetric pair of steps were indirectly set through the maximum heater power difference for the cycle and the number of steps in the cycle. The maximum power difference defined the heating of the last step in a cycle while power differences for other steps were calculated based on the input number of steps per cycle and

the baseline voltage setting for the cycle, as shown in Equation (4.9):

$$
\begin{aligned}
Q_1 + Q_2 &= 2Q_0 + dQ_{max} = \text{constant}, \\
Q_0 &= \frac{dQ_{max}}{2} + \frac{V_0^2}{R}, \\
Q_1 = Q_0 + \frac{dQ_{max}}{2}\left(1 \pm \frac{i}{N}\right) \qquad & \qquad Q_2 = Q_0 + \frac{dQ_{max}}{2}\left(1 \mp \frac{i}{N}\right).
\end{aligned}
\tag{4.9}
$$

Here $Q_{1,2}$ are the sample heaters power, dQ_{max} is the maximum heater power difference, V_0 is the baseline voltage setting of the cycle, R is the resistance of the heating element (note the same make and model resistive heater was installed on each sample side), i is the active step pair iteration, and N is the total number of step pairs.

Ideally the power driving the heaters should remain constant over the heating steps and would be set by the common ”constant power” mode of the driving power supplies. The particular power supplies we used, however, could not operate in constant power mode so constant voltage mode was used instead. A constant voltage setting does not produce a constant power output in resistive heaters, as their resistance is temperature dependent and this limitation required readjustment after each step voltage setting to ensure accurate heating. So, the power drawn by the resistive heaters were measured immediately following each new voltage setting and if it varied from the intended power setting by more than 0.5%, the voltage setting was recalculated and reset until the power took on its desired value.

The temperature measurements used for thermal conductivity calculations were the temperatures recorded after both sample thermometers had stabilized. Determination of the point at which the rate of temperature change had become sufficiently low that the sample temperatures could be deemed ”stable” was somewhat subjective in principle, but programically managed. In order to make the stabilization determination, temperatures were monitored over discreet intervals of time with length set by the integration time parameter of the control program. Each thermometer tem-

perature was logged at the start of each integration period and then compared with the temperature measured at the end of the period. The difference between these two temperatures was then divided by the integration time to determine the rate of temperature drift of each thermometer and if the rate was below the stability threshold setting, the thermometers were deemed stable. For these measurements, a rate of 50 $\frac{\mu \mathrm{K}}{\mathrm{s}}$ was the usual criterion for stability as it was found to yield thermal conductivity measurements with minimal specific heat dependence (see Equation (4.7)).

Once the rate of temperature change was equal to or less than the stability threshold, measured temperatures were flagged for thermal conductivity calculation until the switching delay setting period had elapsed. If the rate of temperature change remained below the stability threshold for an amount of time greater than the switching delay, then the next heating step initiated. Though if at any point during this period the rate of temperature change exceeded the stability threshold, the timer was reset and the data flagged as to not be used. This instance occurred occasionally, most often due to sudden changes in temperature observed in the base at Ch3, which were attributed to power spikes interfering with the He compressor cycles. Typical temperature differences across the sample over a single cycle ($\Delta \mathrm{T}$) were generally between 0.3 K and 5 K.

Once the final cycle of the the run was completed, the compressor was turned off and a warming subroutine was started to reduce downtime. The warming subroutine used a PI controller to control the sample heaters until all thermometers stabilized at room temperature without additional heat input. Vacuum was maintained on the chamber until the sample was to be taken for post measurement SEM imaging.

4.6 Thermal Rectification Results

Six samples of note were etched and characterized over the course of the work. Some of the early etching runs were not measured for thermal rectification since they did not possess the desired

dendritic structure. The first sample (Run 1, see Table 4.3) was etched with a constant voltage bias, rather than the later employed constant current, and bath temperature was not directly controlled. This resulted in applied current densities decreasing from 1.4 $\frac{\mathrm{mA}}{\mathrm{cm}^2}$ to 0.7 $\frac{\mathrm{mA}}{\mathrm{cm}^2}$ as the rising bath temperature effectively decreased the current density. After etching, the sample was rinsed with DI water instead of the above mentioned post processing multi-solvent submersion method. The porous structures that developed from this were sponge-like and not dendritic.

The second etching run (Run 2) was performed with a constant applied current, though still without bath temperature control and the etch bath, was reused from the first run. A higher current density of 7.4 $\frac{\mathrm{mA}}{\mathrm{cm}^2}$ was applied throughout the run. Upon completion of the etch, the wafer was submerged in DI water for 2 hr, followed by an IPA rinse and a nitrogen blow dry. This resulted in dendritic structures at the bottom of the etch regions. The dendrite trunks and branches were of approximately equal width of $\approx 25\ \mathrm{nm}$. However, relatively little of the etch volume had these dendritic structures, and $\approx 90\%$ of the etched region was unstructured and amorphous. This was attributed to failing to remove the etchant from the wafer quickly enough after etching and prompted the implementation of the pentane submersion after etching.

The third etching run (Run 3) was performed with the same run parameters as the second but the full multi-solvent post processing method described above was implemented. The same etch bath used in runs 1 and 2 was reused again in this run. The resulting structures were dendritic at the base of the etch region with similar dimensions to those of run 2. While a larger volume of the etch region was dendritic than in run 2, the dendrites were not fully formed, i.e. many of the branches between dendrites were connected. This was attributed to the etchant becoming too dilute through its multiple reuses and prompted a new bath for the following run. Overheating was likely also contributing to the breakdown of dendritic structures and, consequently, the bath coolant system was introduced for run 4.

In the fourth etching run (Run 4) the bath was chilled and kept between 1.1 °C and -3.9 °C.

Unfortunately, the power supply that provided the bath bias behaved erratically over the run and current density fluctuated between 5.0 $\frac{\mathrm{mA}}{\mathrm{cm}^2}$ and 0.6 $\frac{\mathrm{mA}}{\mathrm{cm}^2}$. This resulted in bands of differing dendrite dimensions ranging from sizes similar to runs 2 and 3 to underdeveloped bands with few pores. The sample had relatively few dendrites of the desired dimensions though the bath cooling had indeed resulted in a larger fraction of the volume consisting of non-amorphous structures. The power supply was replaced for future runs.

The fifth run (Run 5) implemented all of the etching conditions described in the experimental methods above and yielded the closest to ideal structures as illustrated in Figure 4.4. The current density was held constant without issue at 7.4 $\frac{\mathrm{mA}}{\mathrm{cm}^2}$ and the bath temperature varied from 0° C by less than one degree. The etch bath was reused from run 4. Of the total etch depth of 165 $\mu\mathrm{m}$, the bottom 61 $\mu\mathrm{m}$ consisted of well defined dendritic structures, the middle 75 $\mu\mathrm{m}$ consisted of somewhat dendritic transitional structures, and the top 29 $\mu\mathrm{m}$ consisted of amorphous porous silicon.

In the sixth run (Run 6), a shorter etch period was used in hopes of yielding a larger percentage of the total etch volume to consist of dendritic structures. A 2 hr run period was used in run 6, half of the period used in previous runs, though all other run parameters were the same as in run 5 and the same etch bath was reused. This resulted in dendritic structures of smaller dimensions than in run 5, with trunk widths of $\approx 15\ \mathrm{nm}$ and branch widths of $\approx 12\ \mathrm{nm}$. Further, the total etch depth was 98 $\mu\mathrm{m}$ and the bottom 41 $\mu\mathrm{m}$ consisted of well defined dendritic structures.

All of the etching run results are summarized in Table 4.3. Four additional samples were measured for thermal rectification, however they were prepared by our collaborators at MicroXact more than a year prior to measurement, resulting in complete oxidation. Consequently, these samples have been omitted from the table below.

Ultimately, none of the etched porous silicon samples were found to exhibit thermal rectification.

Sample	Current Density ($\frac{\mathrm{mA}}{\mathrm{cm}^2}$)	Bath Temp. (C)	Post-etch Process	Structure	Example Cycle Ave. κ Values $\bar{\mathrm{T}}$ (K)	κ ($\frac{\mathrm{W}}{\mathrm{m-K}}$)
Run 1	1.4-0.7	Unregulated	DI rinse	Sponge-like	Not measured	
Run 2	7.4	Unregulated	DI 2 hr bath IPA rinse	Small volume of swollen dendrites	Not measured	
Run 3	7.4	Unregulated	Full multi-solvent method	Large volume of swollen dendrites	109 115 127 161	2.9 3.1 3.2 3.6
Run 4	0.6-5	-3.9-1	Full multi-solvent method	Bands of varying structures	Not measured	
Run 5	7.4	0	Full multi-solvent method	Near-ideal structures	74 101 140 187	1.1 1.3 1.5 1.7
Run 6	7.4 $\frac{1}{3}$ etch period	0	Full multi-solvent method	Smaller-scale structures	58 75 98 135	2.4 2.9 3.1 3.5

Table 4.3: Silicon etching run parameters, resulting structures, and average thermal conductivity measurements over selected measurement cycles.

While some measurements found apparent thermal rectification in some cycles, these results were not reproducible. Reproduction trials involved either measuring the sample again under the same conditions or repeating the run with the sample orientation reversed in the mount.

There are several possible explanations for the lack observed rectification, though two main concepts are likely the cause. Heat conduction in the structures we produced may not have been dominated by ballistic phonons or our measurement system may not have been sufficiently sensitive to measure the rectification. The central tenant of why nanodendritic silicon should produce thermal rectification is that so long as the phonon mean free path is longer than the branch width, ballistic heat conduction will be heavily influenced by the dendrite geometry. Phonon mean free paths in bulk crystalline silicon are on the order several microns at 10 K [79] and $\approx$ 100 nm at 300 K [22], which encompasses the temperature range used in this work (80 K to 250 K). The dendritic structures produced generally had a trunk width of $\approx$ 20 nm, branch width of $\approx$ 10 nm as measured by SEM the day following etching, which lies well within the desired scales for the temperature range of interest. It is possible, howevere that the phonon mean free path in the pro-

duced dendritic silicon samples was much shorter than that of bulk silicon. Additional concern for interface scattering was perhaps needed in these structures.

Potential causes of deviation from the ballistic phonon regime are oxidation of the silicon dendrites enlarging them beyond the desired dimensions. Another possibility was that the dendrite structures were not surviving the rectification mounting and measurement process. Both of these cases were studied by SEM imaging and found to be unlikely. Upon completion of the etching process the sample part of the wafer was immediately mounted in the measurement system and pumped down while another was saved for imaging the following day. The oxidation rate of the sample was reduced by keeping it in vacuum as long as possible, and even though the imaged wafer pieces were kept in air overnight prior to imaging, they showed the desired structures. SEM imaging of the structures after rectification measurement showed a small increase in dendrite branch volume near the base of the etch depth as shown in Figure 4.12.

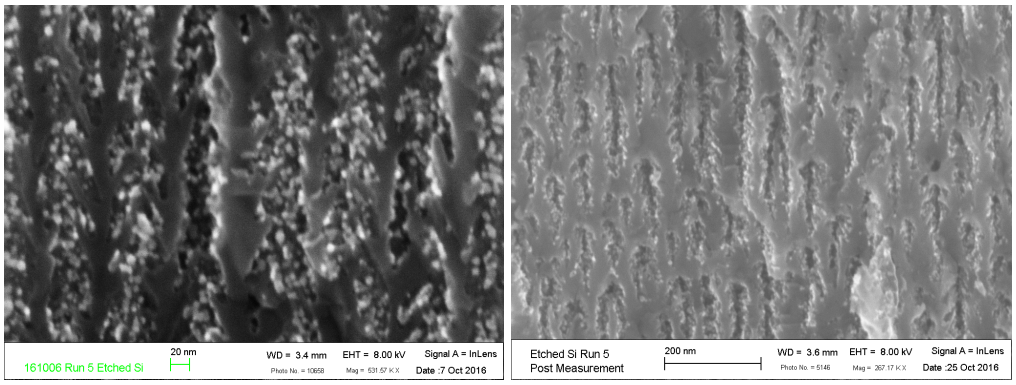

(a) Dendritic structures near base of etch depth prior to rectification measurement.

(b) Dendritic structures near base of etch depth after rectification measurement.

Figure 4.12: Comparison of dendrite oxidation effects prior to and after a measurement run.

Though some oxidation is apparent, how much of it occurred over the course of the run, versus how much occurred once removed from vacuum, is not known. Further, the lowest average sample temperature measurements, corresponding to the longest phonon mean free paths, were taken first in all runs and though oxidation should be minimized in that case, no rectification was found. Even

when oxidized, branching dendritic structures are still prevalent in the sample and rectification should occur, though longer phonon mean free paths would be required.

Deviation in our samples from ideal dendritic structures, i.e. long branches with multiple bifurcations, reduced their rectification potential. Most of the branches in our structures were on the order of 20 nm long and generally without a single bifurcation. Theoretical modeling of these inherently chaotic structures was not feasible, however sawtooth structures had been modeled as detailed above and were the basis of our dendrite size goals. Dendrites on with feature sizes similar to Run 5 matched the desired scale closely, specifically branch widths and thicknesses on the order of tens of nanometers was expected to yield ballistic phonon heat conduction and consequent rectification.

Compounding factors arising from the differences in phonon conduction between bulk and nanodendritic silicon could also have led to smaller rectification than expected. If this was the case, then measuring thermal conductivities at lower average temperatures may have revealed rectification in our samples. Another possibility is that rectification was occurring but at a smaller degree than expected and was below our detection limit, which was $\approx 1\%$.

Finally, one must consider that heat conduction on the nanoscale is not a well understood process. A prime example of this lies in the work of Chang [21] mentioned above. The results of that experiment found rectification but the greater heat conduction direction was opposite to the direction expected from ballistic-phonon dominated thermal transport. The authors postulated that solitons, non-deforming wave packets resulting from nonlinear systems, dominated heat conduction instead and could explain the results. This explanation, however, was subject to debate [110]. Ultimately, the experimental result of our work supports the result of Chang in that ballistic phonon models may not sufficiently explain heat conduction in the regimes where they are supposed to dominate.

Chapter 5

Plasmonic Enhancement in Metallic Nanospheroids

5.1 Principles of Plasmonics

When considering the electron configuration of a metal at a scale beyond the quantum level, it is often most convenient to view the metal as a free electron gas immersed in a background of stationary positive ion cores. When exposed to an oscillating electromagnetic field (i.e. light) the density of this electron gas oscillates in response though dampened by collisions. This results in a driven, dampened, harmonic oscillation of electrons and the quantum of this oscillation is known as a plasmon. In this chapter, Sections 5.1 and 5.2 are background review on plasmonics while Sections 5.3 and 5.4 present our results.

The ability of the electron gas to respond to the incident electromagnetic field is entirely dependent upon the frequency of the field. If the frequency is too high, the resulting oscillations will not be able to react fast enough to screen the field and propagation through the electron gas will occur.

The frequency at which the electron gas becomes unable to screen incident fields is known as the plasma frequency, shown in Equation (5.1). Incident light with frequencies below this value are reflected by the metal, while light with frequencies above this value propagate in the electron gas:

$$\frac{1}{\sqrt{1+\varepsilon_2}} \qquad \omega = \omega_{\mathrm{sp}} \qquad \omega_{\mathrm{p}} = \sqrt{\frac{\mathrm{n_e e}^2}{\varepsilon_0 \mathrm{m}^*}}. \tag{5.1}$$

Here, $\mathrm{n_e}$ is the electron number density, e is the electron charge, ε_0 is the vacuum permittivity, and m^* is the effective electron mass. This can be derived directly from Maxwell's equations and is done in *Plasmonics: Fundamentals and Applications* by Maier [75]. An interesting consequence of solving Maxwell's equations for traveling waves in this situation is that only transverse excitations can exist and do so only when $\varepsilon_1(\omega) = 0$ which occurs at the plasma frequency ω_{p}. The plasma frequency can also be derived from the harmonic motion resulting from an electron cloud that is longitudinally displaced, which makes the plasma frequency effectively the natural frequency of oscillation of the electron cloud. While the electron gas model is a fair approximation of metals, in real metals the transition from total extinction to total absorption spans a small band of frequencies about the plasmon frequency. In most metals, this frequency lies in the ultraviolet region. However, in some metals, interband transitions alter the permittivity and this yields the color seen in metals such as copper and gold. Note that while these principles are derived from bulk material properties and are the basis of what are known as bulk or volume plasmons, plasmons of a different sort can be generated at metal/dielectric interfaces, as well as in nanostructures.

Surface plasmons are plasmonic oscillation quanta which occur on the interface between a medium with a positive real dielectric constant and a conducting medium with a dielectric function which may be complex but whose real component is negative. The simplest example of such an interface is that of a metal surface exposed to air. These surface plasmons, also known as SPPs, comprise the electron oscillation and an associated electromagnetic field which extends into both media, with

an exponential decay in magnitude. The dispersion relation governing SPPs propagating along the interface is given by

$$\mathrm{k_x} = \frac{\omega}{\mathrm{c}} \sqrt{\frac{\varepsilon_1 \varepsilon_2}{\varepsilon_1 + \varepsilon_2}}. \tag{5.2}$$

Here, $\mathrm{k_x}$ is the SPP wave vector, ω is the oscillation frequency, c is the speed of light, and ε_1 and ε_2 are the dielectric functions of the metal and air respectively. The surface plasmons also are associated with a specific plasmon frequency (ω_{sp}), occurring when $\varepsilon_1 + \varepsilon_2$ is minimized. ω_{sp} dependent upon the bulk plasmon frequency and is given by

$$\omega_{\mathrm{sp}} = \frac{\omega_{\mathrm{p}}}{\sqrt{1 + \varepsilon_2}}. \tag{5.3}$$

In the case of a metal and air interface, this simplifies to $\omega_{\mathrm{sp}} = \omega_{\mathrm{p}}/\sqrt{2}$. The dispersion relations of bulk and surface plasmon dispersion relations are illustrated in Figure 5.1.

SPPs always exhibit TM polarization. On a flat surface, SPPs cannot be directly excited by incident light, due to the dispersion relation lying entirely to the right of the light line, that is $\mathrm{k_x} > \omega/\mathrm{c}$. Consequently, in order to excite surface plasmons the photon momentum ($\hbar\omega/\mathrm{c}$) of the incident wave must be increased. This can be accomplished either by adding a grating coupler [104] or working with a three layer system involving a thin metal film and two dielectric media of different dielectric constants [61, 94].

In the case of the grating coupler, consider light at angle θ incident to a periodically corrugated surface with grating constant a. The component of the wave along the surface can have a wave vector component of $\mathrm{k_x} = \frac{\omega}{\mathrm{c}}\sin\theta \pm \frac{2\pi \mathrm{N}}{\mathrm{a}}$ for integer N. Setting this wave vector equation equal to the dispersion relation (Equation (5.2)) one can then adjust the angle of incidence and/or grating constant to cause surface plasmon excitation. This effect can be generalized for any surface

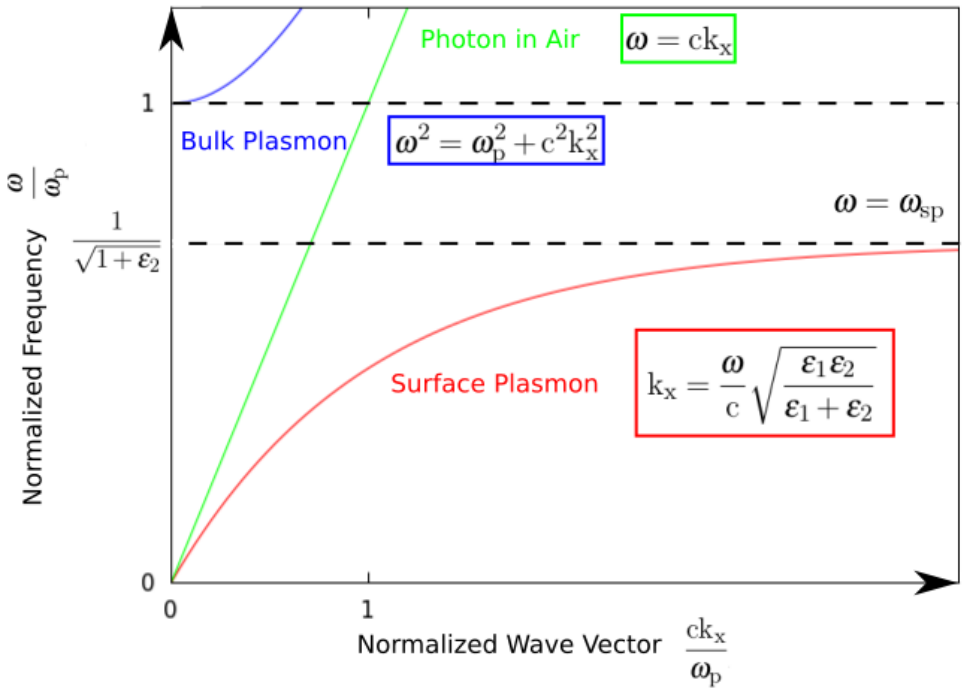

Figure 5.1: Bulk and surface plasmon dispersion relations, normalized by plasmon frequency.

of roughness, such as the silver nanosphereoid films used in this work, and is most commonly expressed as in Equation (5.4):

$$k_x = \frac{\omega}{c}\sin\theta \pm \Delta k_x = \frac{\omega}{c}\sqrt{\frac{\varepsilon_1\varepsilon_2}{\varepsilon_1+\varepsilon_2}}. \tag{5.4}$$

Here Δk_x is a generalized perturbation factor due to roughness. Experimentally, surface plasmon excitation is detected by finding a sharp drop in reflected light intensity while adjusting angle of incidence. A diagram depicting such a coupler is shown in Figure 5.2.

In the case of the three-layer system, the simplest method of producing surface plasmons is to coat the base of a prism in a thin metal film and direct light through the prism, reflecting off of the film. As the beam propagates through the prism, and is reflected off the metal it will project an in-plane wave vector on the metal of $k_x' = \frac{\omega}{c}\sqrt{\varepsilon}\sin\theta$ which couples to a surface plasmon on

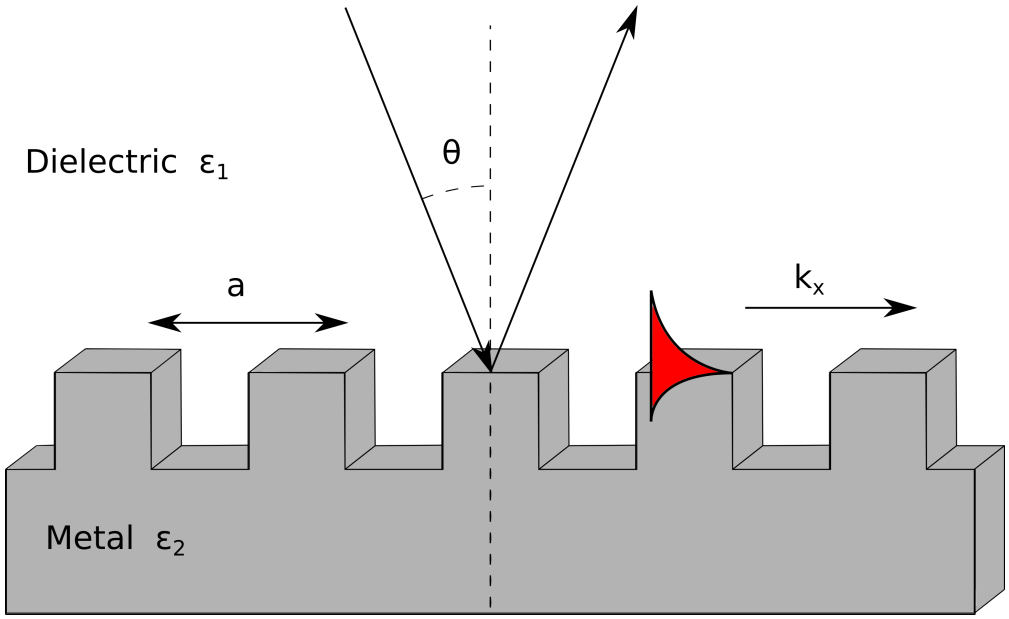

Figure 5.2: Grating coupling method of surface plasmon polariton generation.

the metal film/air interface. The increase in k_x' due to the dielectric constant $\varepsilon > 1$ of the prims makes it possible to match this wave vector to the wave vector k_x of a SPP propagating on the other side of the metal film. This coupling scheme is known as the Kretschmann configuration. In an alternative scheme, known as the Otto configuration, a metal film is deposited on a surface while the prism through which light is directed sits above an air gap. Here, so long as the air gap is of size $\approx \lambda$ field tunneling can occur to excite plasmons at the metal/air interface as in the Kretschmann configuration. Example diagrams of the two configurations are shown in Figure 5.3.

The final genre of plasmonic excitation are known as localized surface plasmons. Unlike SPP excitations, localized surface plasmons encompass the entire structure they are generated on and do not propagate. The most commonly encountered case of localized surface plasmon resonance is in metallic nanoparticles, surrounded by a dielectric, excited by the visible spectrum. If the diameter of the nanoparticles is much smaller than the wavelength of incident light, then one can approximate the scenario as a solid metal sphere exposed to a uniform electric field that undergoes harmonic oscillation. This problem can then be solved by separating the field's time-dependence

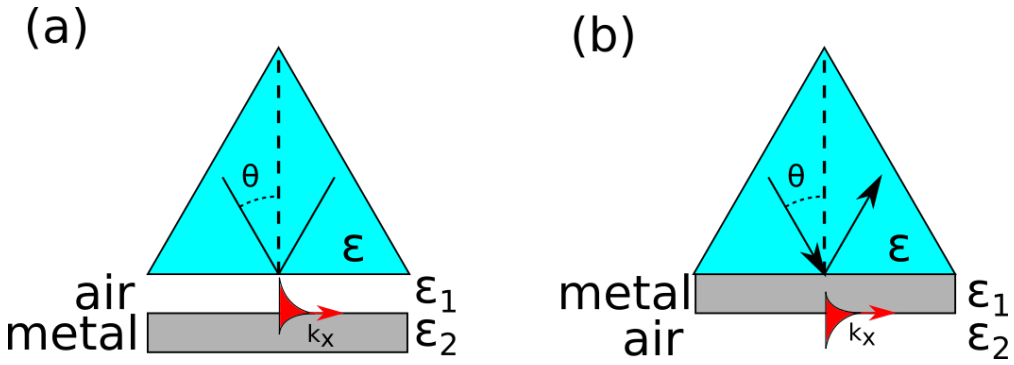

Figure 5.3: Prism coupling methods of surface plasmon polariton generation. (a) Otto configuration. (b) Kretschmann configuration. In both configurations, surface plasmons are generated on the metal/air interface.

and solving for the electrostatic case. Ultimately, the sphere acts as an electric dipole with a dipole moment given by

$$\mathrm{p} = 4\pi\varepsilon_0\varepsilon_2\frac{\varepsilon_1-\varepsilon_2}{\varepsilon_1+2\varepsilon_2}\mathrm{a}^3\mathrm{E}_0. \tag{5.5}$$

Here, a is the nanoparticle radius, E_0 is the time-independent electric field, and ε_1 and ε_2 are the permittivities of the metal and dielectric respectively. As in the other plasmon instances, the permittivity of the metal is complex and frequency-dependent. The condition for localized surface plasmon resonance is met when $\varepsilon_1 + 2\varepsilon_2$ is at a minimum, which occurs in the visible spectrum for gold and silver nanoparticles. Key to this solution is the approximation of the uniform electric field, which is generally true if the nanoparticle size is much less than the wavelength of light exciting it. A more general solution is found through the implementation of Mie theory [84] and involves an infinite series expansion of vector spherical harmonics. From Mie theory, the absorption and scattering efficiencies of LSP decays for nanospheres can be calculated [51] for non-magnetic media are given by

$$
\begin{aligned}
Q_{ext} &= \frac{2}{x^2}\sum_{n=1}^{\infty}(2n+1)\mathrm{Re}(a_n+b_n),\\
Q_{sca} &= \frac{2}{x^2}\sum_{n=1}^{\infty}(2n+1)\mathrm{Re}(|a_n|^2+|b_n|^2),\\
Q_{abs} &= Q_{ext}-Q_{sca},\\
a_n &= \frac{m\psi_n(mx)\psi_n'(x)-\psi_n(x)\psi_n'(mx)}{m\psi_n(mx)\xi_n'(x)-\xi_n(x)\psi_n'(mx)},\\
b_n &= \frac{\psi_n(mx)\psi_n'(x)-m\psi_n(x)\psi_n'(mx)}{\psi_n(mx)\xi_n'(x)-m\xi_n(x)\psi_n'(mx)}.
\end{aligned}
\tag{5.6}
$$

Here, Q_{ext}, Q_{sca}, and Q_{abs} are the extinction, scattering, and absorption efficiencies, ψ and ξ are Riccati-Bessel functions, m is the ratio of the refractive index of the sphere to surrounding medium (n_m), and x is a dimensionless size parameter equal to $\frac{2\pi n_m R}{\lambda}$ for sphere radius R. In Jao's doctoral dissertation [53], Equation 5.6 was employed in comparison of extinction measurements, taken by spectroscopy, of gold nanospheres and agreement with simulations was found using dielectric functions taken from Johnson and Christy's work [103] over the first 12 multipoles ($n = 1$ to $n = 12$).

As plasmons are excited states, they are transient and decay. Depending on the type of plasmon, the structures on which it exists, and the energy of the plasmon, different decay mechanisms can occur. There are two categories of plasmon decay: radiative and non-radiative. In radiative plasmon decay, the excitation is transferred to a propagating photon, and is essentially the reverse of the plasmon excitation process. In general, radiative plasmon decay is dominant in larger systems while non-radiative decay becomes more prevalent in at decreasing sizes [136]. However, the particular plasmon mode , which is largely defined by the medium's geometry, also strongly influence the decay mode. In non-radiative plasmon decay, the plasmon gives up energy though excitation of electron-hole pairs through Landau damping that, in turn, decay through a variety of mechanisms.

Thermalization is a highly probable non-radiative decay method of plasmons [71]. In thermalization the plasmon decays into a carrier, such as an electron, and excites it above the ambient thermal excitations of other electrons. The electron then scatters through other electron-electron interactions which result in multiple lower-energy excited carrier states. These states, in turn, scatter through electron-phonon interactions with the supporting lattice finally yielding a heating of the entire structure. These electron-hole excitations are often referred to as "hot" because their energies are substantially larger than excitations caused by ambient thermal conditions [11]. If receptor states in adjacent structures are available, the hot electrons or holes can also transfer to these sites in a process known as hot carrier injection [10]. It is also possible that plasmons can decay directly into adsorbates on or near the surface metal resulting in electron excitation in the adsorbate through a process known as chemical interface damping [55]. These two non-radiative plasmon decay mechanisms are key to this work, where adsorbate catalysis will be employed on nanosphereoid surfaces through plasmon decay.

The rate at which these decay processes occur depends on the structure and media involved, however the order of magnitude of time required for each decay step can be roughly estimated in the general case. Recall that if a plasmon is to decay by thermalization, it first must decay into and consequently excite a carrier, then the excited carrier scatters into other carriers which in turn scatter into phonons. If we say that plasmon excitation occurs at $\mathrm{t} = 0$ and is destined to decay by thermalization then Landau damping of plasmon to excited carrier occurs at 1-100 fs. Next, excited carrier to non-excited carrier scattering occurs as 100 fs to 1 ps. Finally, carrier to phonon scattering occurs at 100 ps to 10 ns [10]. Hot carrier injection also begins with Landau damping, but then the hot carrier then transfers to the nearby available receptor state prior to scattering with other carriers, and generally occurs within 1 ps [10]. Chemical interface damping, on the other hand, is much faster as the plasmon decays directly into the absorbate within ≈ 5 fs [55]. Again, these time-frames vary substantially depending on the geometries and mediums involved.

The goal of the plasmonic work presented here is to explore a plasmon-induced method of selective gold nanosphere to silver nanospheroid adsorption that could be used in photolithography, in which gold nanosphere receptor groups can be activated or deactivated through light exposure. In this method, a photocleavable ligand attached to silver nanospheroids is used such that, when cleaved by ultraviolet exposure, it is receptive to gold nanosphere conjugation. While this property alone enables photolithographic patterning with gold nanospheres, the ligand, when attached to a silver nanospheroid, has also been observed to become non-receptive to gold nanosphere adsorption when exposed to green light. This deactivation effect is likely plasmonic in nature the green light used is capable of plasmon excitation in the silver nanospheroids and the effect occurs with far less efficiency when the ligand is attached instead to continuous silver films, where plasmon excitation does not occur. Chemical interface dampening likely triggers a chemical reaction in the surface ligand that inhibits gold nanosphere adsorption. This technique makes image reversal patterning of nanospheres feasible and can enable creation of new superstructures previously not able to be produced by mass production techniques.

5.2 Chemical Materials: Lip3, Gold Nanospheres, and Silver Nanospheroid Films

The photocleavable ligand which was attached to nanostructures and films in this work was 1-(6-Nitrobenzo[d][1,3]dioxol-5-yl)ethyl(4-(1,2-Dithiolan-3-yl)butyl) carbamate. This compound (here denoted Lip3) uncages an amine when exposed to UV light as illustrated in Figure 5.4 below.

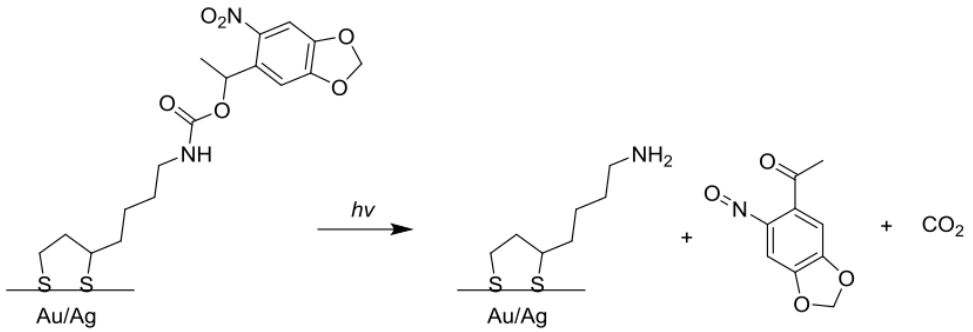

Figure 5.4: Photocleavable ligand 1-(6-Nitrobenzo[d][1,3]dioxol-5-yl)ethyl(4-(1,2-Dithiolan-3-yl)butyl) (Lip3) photouncaging by UV exposure.

Previous works by Daengngam [26] and See [118] have studied, at length, the binding properties of Lip3 to gold and silver surfaces as well as the adsorption of gold nanospheres to uncaged Lip3. In short, when a metal film is submerged in a 1 mM ethanolic solution of Lip3, a self-assembled monolayer of Lip3 forms as the disulfide group bonds to the metal. UV exposures of 1 $\frac{\text{J}}{\text{cm}^2}$ or greater result in the uncaging of the amine group, which becomes positively charged at low pH. As our gold nanospheres in suspension at pH 4-6 are negatively charged, they can therefore bind to the expanded amine group. When uncaged Lip3, attached to a silver nanospheroid film, is exposed to ≈ 2 $\frac{\text{J}}{\text{cm}^2}$ of green light, a poorly understood process occurs that negated the ability of the ligand to adsorb gold nanospheres, as illustrated in Figure 5.5. See [118] also observed that green light exposure prior to photocleaving did not inhibit nanosphere adsorption, and consequently enabled greater selective adsorption as the green light negated groups that were unintentionally cleaved prior to UV exposure.

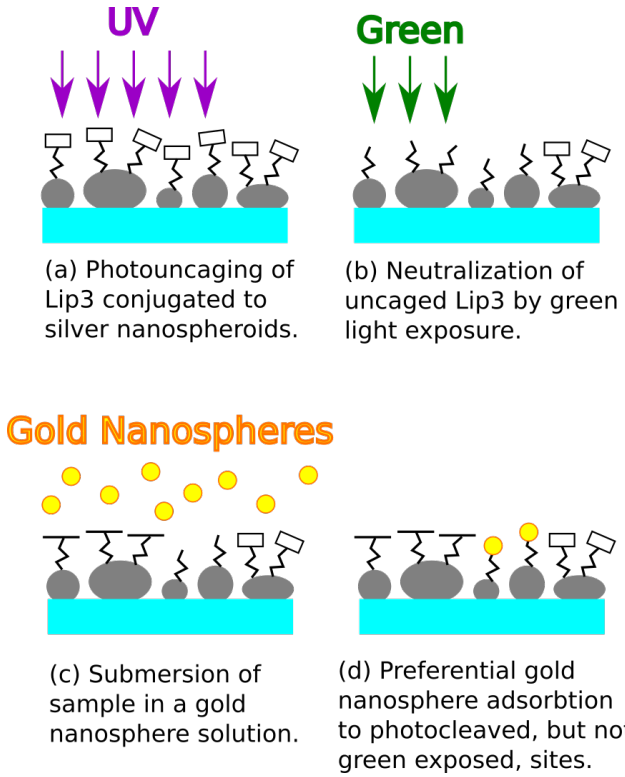

Figure 5.5: Green light exposure-induced inhibition of gold nanosphere adsorbtion to photocleaved Lip3.

In this work, photolithographic techniques were employed to enable high resolution nanosphere patterning in order to expand on See's findings and attempt to elucidate the mechanism behind it. As the green light effect is plasmonic in nature, it should have a greatly reduced effect on continuous silver films when compared with silver nanospheroids. To test this, photolithographically defined regions of continuous silver films adjacent to silver nanosphereoid films were produced and conjugated with Lip3. Next, a UV exposure of a "VT" logo pattern that straddled the film/-nanospheroid border was performed followed by green light exposure of the bottom half of the "VT" logo region. After exposure, gold nanospheres where then adsorbed onto the sample and the resultant pattern was imaged by scanning electron microscopy (SEM) and X-ray photoelectron spectroscopy (XPS) in order to measure gold nanosphere adsorbtion rates. This process is described in more detail below and illustrated in Figure 5.6. Separate IR-spectroscopy measure-

ments were also performed in which live spectra were taken throughout UV and green exposures of Lip3. The goal of these spectroscopy measurements was to determine if the chemical structure of photouncaged amine group was being altered by the light exposures.

In all of the chemical processes in this study, borosilicate glassware was used. The gold nanospheres were synthesized by the Turkevich method [35]. Monodisperse gold nanospheres of $\approx 10-20$ nm diameter where made by this method as follows: 100 mL of 1 mM aqueous $HAuCl_4$ was brought to a boil in a covered 125 mL Erlenmeyer flask. Next 10 mL of 38.8 mM trisodium citrate were added under rapid stirring, typically ≈ 500 rpm, turning the solution dark blue. The solution was then kept boiling and under rapid stirring for 20 min, though the solution turned a vibrant red typically within the first minute. After allowing the solution to cool, the vessel containing it was sealed in Parafilm, wrapped in Al foil, and kept refrigerated. Note that the glassware and stir bar used were always precleaned by immersion for 20 min in aqua regia, followed by thorough rinsing with DI water and blow drying with dry argon or nitrogen gas. The diameter of the gold nanospheres produced in each batch was initially measured by dynamic light scattering, though the system used was often found to yield inaccurate results and was viewed as a quick means of approximation. Scanning electron microscope measurements were later used on the final post patterned samples to determine actual sphere size.

The silver nanospheroid films used in this work were produced by the Tollens method as follows. To minimize disruption to the pre-patterned sample surfaces, the samples themselves were precleaned by brief sonication in acetone followed by isopropyl alcohol, then a DI water rinse. Samples were blown dry with Ar gas. 3 mL of 0.1 M (aqueous) $AgNO_3$ was prepared in a dedicated glass vial containing a stir bar. This vial was rarely acid cleaned, instead only triple rinsed with DI water after synthesis and sealed while full of DI water between syntheses. While stirring at $\approx$ 60 rpm, diluted NH_4OH (1 NH_4OH : 2 H_2O) was added drop-wise to the $AgNO_3$ solution. This caused the solution to initially turn cloudy and brown. Additional drops were carefully added

until the solution turned clear, effectively raising the pH. Next, 1.5 mL of 0.8 M (aqueous) KOH was added, turning the solution black. Additional drops of diluted NH_4OH were then added until the solution turned clear once more. Next 0.5 mL of the solution was added to a small centrifuge tube containing 0.5 mL 0.5 M (aqueous) D(+) glucose and then shaken vigorously for $\approx$ 2 s before drop casting onto the cleaned sample surface. The incubation time on the glass determined the silver nanospheroid average diameter, with longer times trending toward larger average diameters until ultimately forming an unbroken film. A 75 s incubation time was most commonly used and resulted in an average silver nanospheroid diameter of $\approx$ 50 nm. To halt the reaction, the sample was sequentially submerged in two beakers of DI water and blown dry with Ar gas.

5.3 Lithographic Patterning and Spectroscopic Analysis Methods

5.3.1 Lithographic Patterning of Gold Nanospheres on Silver Nanospheroid Films

The main goals of the experiments on the green light effect involved testing the viability of image reversal by green light exposure, green light dosage dependence of gold nanosphere adsorption, and plasmonic enhancement of the effect. In order to test these properties, measurements were needed of samples on continuous films as well as silver nanospheroids at different green light doses. While the Tollens method readily produces silver nanospheroid films, the growth mechanism is not easily controllable and therefore the average nanospheroid diameter can vary substantially from batch to batch. As plasmon resonance is highly dependent on the size of the nanostructure, direct comparison of samples from different Tollens batches is difficult. To circumvent this issue, comparative measurements were performed on samples that were lithographically

pre-patterned to have multiple regions containing boundaries between nanospheroid film and continuous so that a single Tollens batch could yield multiple measurable sample regions. The process of producing the final gold nanosphere patterned surfaces is illustrated in Figure 5.6.

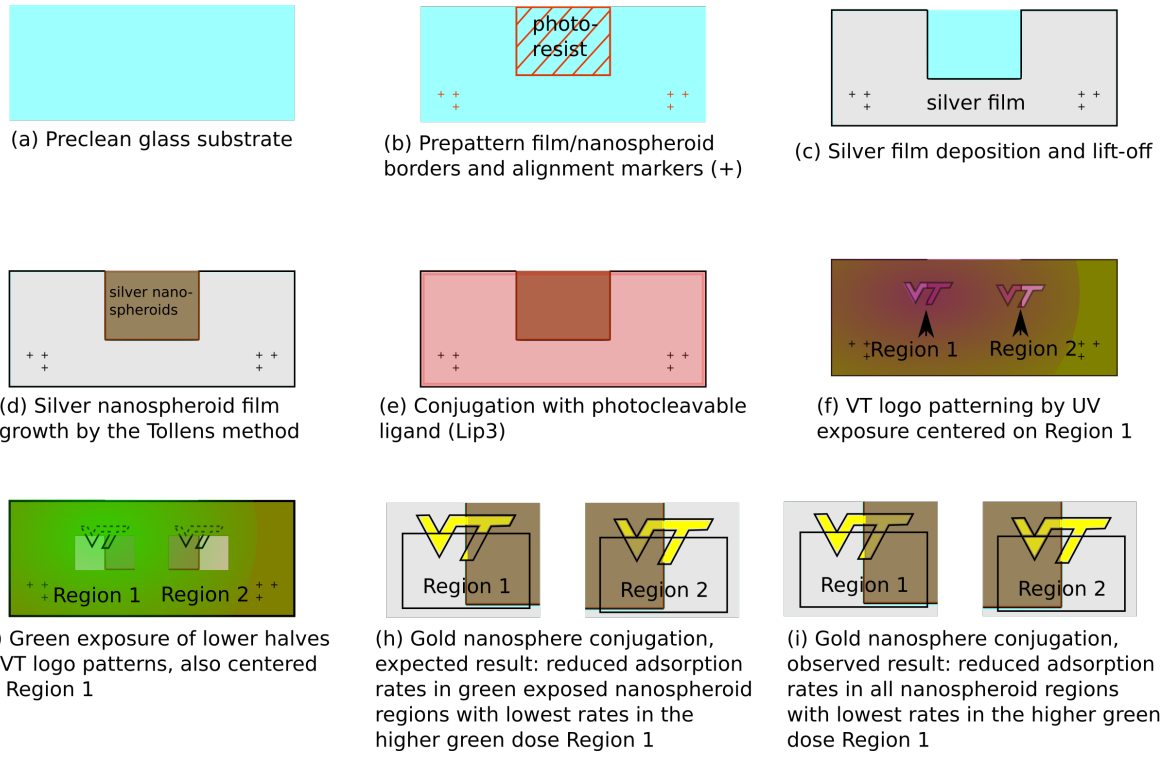

(a) Preclean glass substrate

(b) Prepattern film/nanospheroid borders and alignment markers (+)

(c) Silver film deposition and lift-off

(d) Silver nanospheroid film growth by the Tollens method

(e) Conjugation with photocleavable ligand (Lip3)

(f) VT logo patterning by UV exposure centered on Region 1

(g) Green exposure of lower halves of VT logo patterns, also centered on Region 1

(h) Gold nanosphere conjugation, expected result: reduced adsorption rates in green exposed nanospheroid regions with lowest rates in the higher green dose Region 1

(i) Gold nanosphere conjugation, observed result: reduced adsorption rates in all nanospheroid regions with lowest rates in the higher green dose Region 1

Figure 5.6: Process of lithographic patterning of gold nanospheres on silver films and silver nanospheroid films with the green light inhibition effect.

In short, the patterning process included substrate precleaning, traditional photolithography for alignment marks and glass/metal boundary area definitions, evaporation of silver onto the the patterned slides followed by lift-off, development of a silver nanospheroid film on the sample by the Tollens method, Lip3 conjugation, photouncaging of Lip3 by UV patterning, green light exposure to deactivate the uncaged Lip3 in a different pattern, and finally gold nanosphere adsorption to the remaining active uncaged Lip3.

Soda-lime glass microscope slides were used as the substrates in this work, due to good adhesion of Tollens films as well as compatibility with conventional photolithography techniques. Care

was always taken when handling samples. A single wafer tweezer was used in handling samples and it was regularly cleaned with 30 minute acetone and isopropyl alcohol baths. When not in use the tweezers were stored in a sealed glass vial. When not in active processing, samples were stored and transported in Parafilm-sealed, vertical, Coplin-jar containers which made contact only at small areas on the edges of the sample.

Prior to the pre-patterning, samples were cleaved from soda-lime glass microscope slides and then cleaned in piranha solution for 30 minutes (Figure 5.6 (a)). Following a thorough DI water rinse, samples were then taken to the MicrON clean room for pre-patterning. Typically, 3 to 4 samples were pre-patterned in the same clean room visit. All samples were pre-patterned with alignment marks and continuous metal areas on which the Tollens method would not form nanospheroids but rather thicken the film (Figure 5.6 (b)). The transitions between these metal and glass areas were sharply defined and allowed observations of the effect of nanospheroids, where plasmonic enhancement should occur, versus continuous films, where plasmonic enhancement should not occur.

Pre-patterning of alignment markers and glass/metal area definitions was performed using image reversal photolithography. AZ nLOF 2020 reversible photoresist was spun onto the samples in two stages: first at 500 RPM for 15 s and then 3000 RPM for 40 s. Next the sample was pre-baked by setting it in a preheated oven set to 100 °C for 1 minute. Prior to mounting the ”LRIR MASK” photomask, see Figure 5.7, in the MA-6 mask aligner, the mask was always precleaned by rinsing with acetone, followed by isopropyl alcohol, followed by DI water and nitrogen blow dry. Once the mask and sample were mounted in the mask aligner, the box with crenelations pattern was aligned on the sample. Exposure doses were 66 $\frac{\mathrm{mJ}}{\mathrm{cm}^2}$. A post-exposure bake followed in a preheated oven set to 130 °C for 180 s. The sample was then developed in 300 AZ MIF developer by submersion and gentle shaking for 120 s. Immediately after developing, the sample was submerged in DI water and then blown dry. To further improve pattern quality, the sample was then descummed by the

plasma asher for 30 s at 600 W.

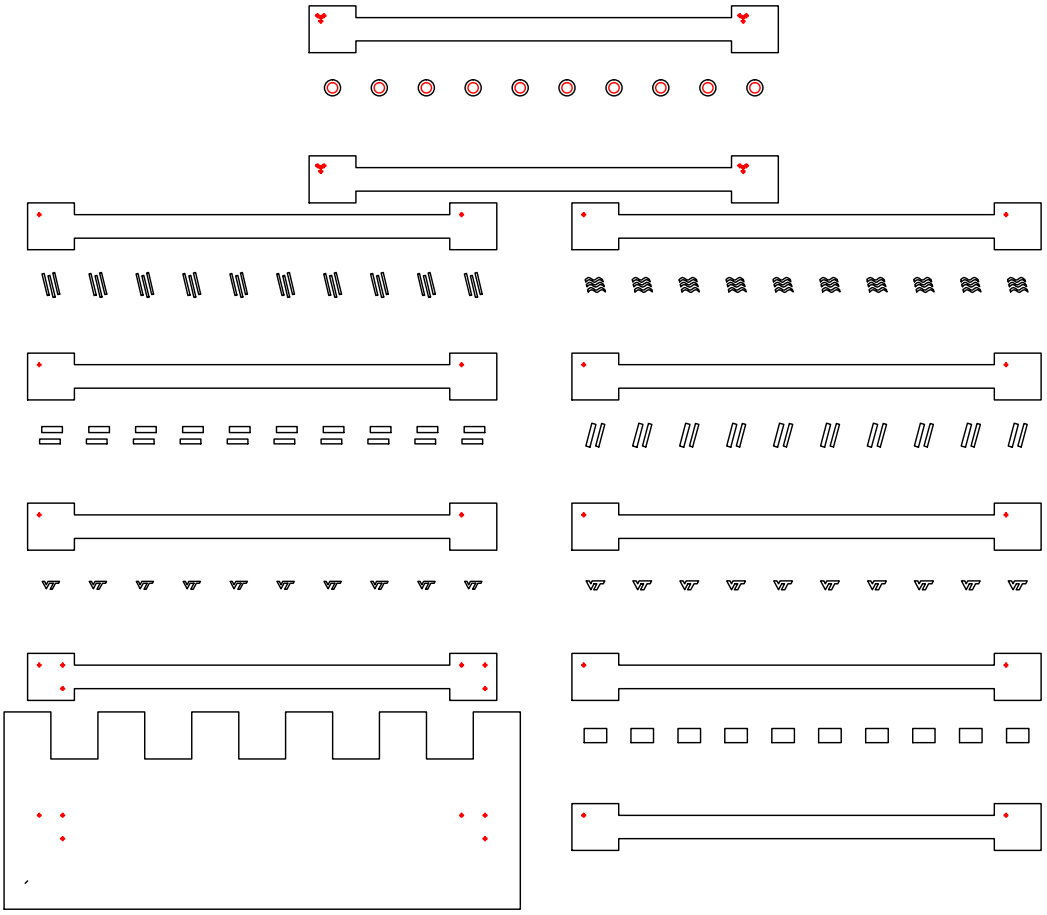

Figure 5.7: 4" Photomask used for patterning and pre-patterning of samples for use with plasmonic enhancement-driven reverse lithography

E-beam evaporation was used to deposit the silver film which, after lift-off, made the alignment markers and well defined silver film/glass boundaries (Figure 5.6 (c)). Chromium was first evapo-

rated as an adhesion layer with a thickness of 5 nm, then silver was evaporated with a thickness of 30 nm.

Silver film lift-off was accomplished by using AZ 400T Photoresist Stripper. Nominal stripping procedure involves heating two beakers to 70 °C - 80 °C on a hot plate and submerging the sample in one beaker for several minutes to remove the bulk of the resist, and then transferring to the second beaker for several minutes to remove residuals. Often ≈ 15 minutes in the first bath and ≈ 5 minutes in the second bath was found to be sufficient. Samples were then submerged in DI water and blown dry with an inert gas before storage in a clean container.

Once pre-patterning was completed, a Tollens silver surface was applied to the sample (Figure 5.6 (d)) as outlined above, immediately followed by Lip3 conjugation (Figure 5.6 (e)). As the Tollens method produces nanospheroid films by aggregate growth, glass substrate areas developed nanospheroid films while patterned silver film areas only grew slightly in thickness. Due to the photosensitivity of Lip3 to visible wavelengths, all work involving the direct handling of Lip3 was performed in dark room conditions with limited red light illumination. Lip3 was usually provided in 2 mM, 20 mL vials and was diluted by adding equal amounts of ethanol to bring the molarity down to 1 mM, most commonly with 5 mL Lip3 solution and 5 mL ethanol in a 40 mL beaker. Next the beaker was purged with argon by covering the opening with Parafilm, lifting a corner up, and blowing argon in through the opening for ≈ 3 minutes. Once purged, the beaker was resealed with Parafilm, wrapped in aluminum foil, and placed in a dark box for ≈ 36 hours. The sample was then rinsed in ethanol, blown dry with argon and put back in a dark space for 5 hours of air exposure prior to all light exposures.

UV and green light exposures were performed (Figure 5.6 (f) and (g)) on the Lip3 bonded samples in our in-house lithography system, which was a modified version of the kHz frequency-domain thermoreflectance system, and shown in Figure 5.8.

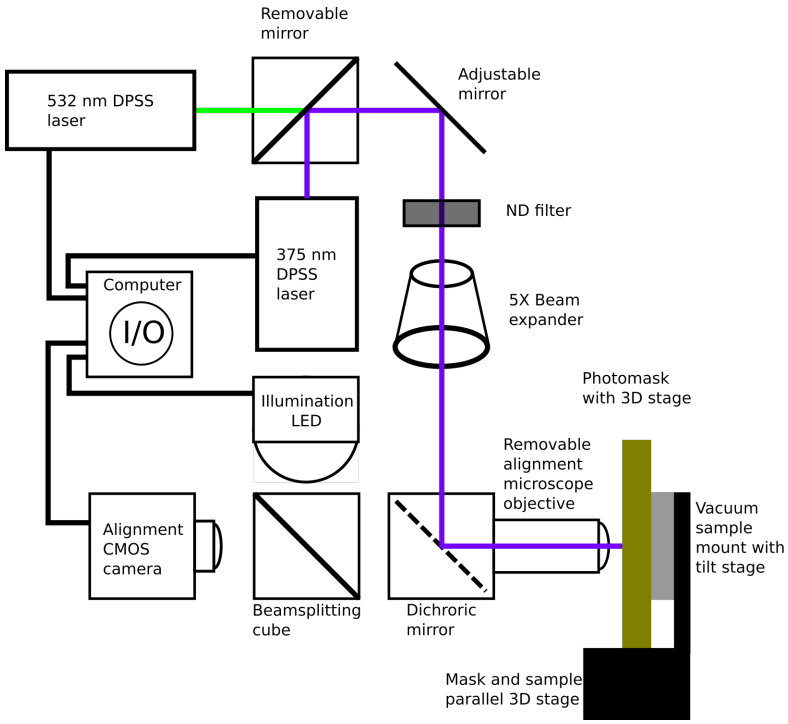

Figure 5.8: Plasmonic enhancement driven reverse lithography system diagram

Alignment of this system not only involved aligning both beams to the sample exposure area, but also aligning the photomask to the pre-patterned areas on the sample. Both alignments were performed by using a CMOS camera that viewed the sample through a microscope objective, with illumination provided by a white LED.

Beam spot centers in the alignment camera's view were found prior to sample installation by bringing a blank sample into focus and activating the beams. The location of the beam spots were then marked in the live camera feed program, after which beam emissions were deactivated prior to sample mounting. The sample was mounted on a vacuum stage that was capable of tilt in order to keep the sample face plane parallel to the mask plane. The mask was mounted on a 3-dimensional translation stage system that enabled alignment of the mask to the sample by means of the prepatterned guide marks on the sample. Once the sample and photomask guide markers were aligned when in contact, the mask and sample parallel movement stages were used to

center the region of interest at the beam spot center without disturbing the mask-sample alignment. When fully aligned, the illumination LED was turned off, the alignment microscope objective was removed, and the exposure stages were begun.

Over the course of the exposure process the room was kept dark with the only active monitor set to a red display mode. The white light source used to illuminate the sample for the CMOS camera passed through the longpass (567 nm cutoff) dichroic mirror, prior to sample incidence, effectively filtering out green wavelengths. Regardless of this filtering, sample illumination time and intensity during the alignment process was minimized to limit unintentional exposure.

The lasers used in this system were a 375 nm UV laser and 532 nm green laser that were both Gaussian (TEM_{00}) diode-pumped solid state lasers of similar design and operation, though the UV laser had a maximum power setting of 60 mW and the green laser had a maximum of 40 mW. In order to ensure good alignment between the photouncaging UV exposure and the neutralizing green exposure, the lasers were mounted and aligned such that they shared the same beam path. This was accomplished by means of a removable mirror on a magnetic stage.

A beam expander was put in place to widen the beam spots on the photomask, with an expanded diameter of 0.64 cm for the green beam and 1.27 cm for the UV. An optical density 0.6 filter was also added to the beam expander to bring the beam intensities at the sample to 31.6 $\frac{\mathrm{mW}}{\mathrm{cm}^2}$ for the green beam at 40 mW setting and 7.16 $\frac{\mathrm{mW}}{\mathrm{cm}^2}$ for the UV at 60 mW setting. Recall that the microscope objective in this system is used only for alignment purposes and these intensities are those at the sample surface after alignment and removal of the objective.

In the first stage of exposure, Lip3 was photocleaved in the desired pattern. The most effective photocleaving dose was found to be 3 $\frac{\mathrm{J}}{\mathrm{cm}^2}$ from the UV laser and was carried out by setting the laser output power to 60 mW and the exposure time to 419 s. Following UV exposure, the microscope objective was reinstalled and the pattern that deactivated photocleaved areas was aligned

as above. Once aligned, both the microscope objective and the removable mirror were removed which enabled the green laser to expose the sample. A 2 $\frac{\mathrm{J}}{\mathrm{cm}^2}$ green light dose was found to yield the reversal effect and this was achieved by setting the laser output to 2 mW and exposure time to 1266 s. Light exposures were managed by the UVGreenExposerMK1.vi program in Labview, which enabled laser power setting, exposure time, and beam alignment through an actuator controlled mirror. Immediately following green light exposure and while still in the dark, the sample was removed from the system conjugated with gold nanospheres by submersion for 1 hr (Figure 5.6 (i)). After conjugation, the sample was rinsed with DI water, and blown dry with argon before being subjected to imaging and analysis.

5.3.2 In-situ Infrared Spectroscopy

While the lithography experiments tested the applications of the green light Lip3 negation effect, it was a phenomenological approach and could not elucidate the fundamental cause of the effect. To probe what is occurring throughout green light exposure, at the molecular level, spectroscopic techniques were employed. Reflection-mode IR-spectroscopy was performed live over the course of UV and green exposures in order to monitor changes to Lip3. Gold substrates were required in reflection mode IR spectroscopy and this constraint necessitated a different Lip3 conjugation process than what was used for the photolithography experiments. Spectroscopy of silver nanospheroids on top of a gold substrate was not possible as application of the Tollens method to a gold surface results in a gold/silver continuous surface, rather than a film of silver nanospheroids. However, gold nanospheres of diameter 10-30 nm have a similar absorption peak to green wavelengths as the Tollens produced silver nanospheroids, enabling an analogous test of the plasmonic enhancement effect on Lip3 in spectroscopy.

Conjugation of gold nanospheres to Lip3 was not as straightforward as in Tollens conjugation.

The reason for this is that Lip3 is an ethanolic solution and ethanol removes citrates from gold nanospheres in solution, which decreases their charge and causes aggregation. To circumnavigate this problem, gold nanospheres were mixed with much larger diameter diamond dust and then conjugated with Lip3. This resulted in Lip3 conjugated gold nanospheres aggregating onto the diamond dust particles which were then able to be redispersed and deposited onto a gold slide that was then measured by IR spectroscopy. A sample produced by this method is illustrated in Figure 5.9.

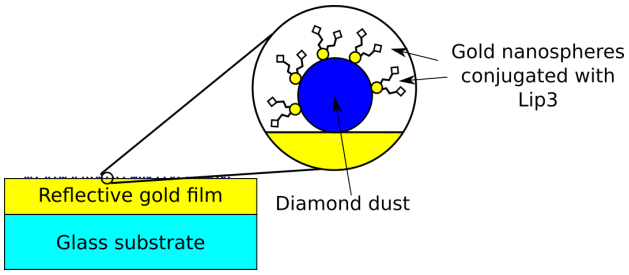

Figure 5.9: Typical IR spectroscopy sample: Lip3 conjugated gold nanospheres on diamond dust deposited on a reflective gold film.

In order to produce these samples, centrifugation techniques were employed. Prior to Lip3 conjugation, 20 mL of 19 nm diameter gold nanospheres were centrifuged at 15 kRCF for 30 min over two 50 mL vials and the supernatant was removed. Next, 5 mL of 1:1 DI water:ethanol, 5 mL 2 mM Lip3, and 3 mg of 1.1x10^{12} $\frac{\text{g}}{\text{mol}}$ diamond dust (0.5 μm average diameter) were added to the precipitate and briefly vortex mixed before being sealed under argon and allowed to conjugate and settle. This resulted in a precipitate of Lip3 conjugated gold nanospheres aggregated onto diamond dust. To remove excess Lip3, this precipitate was washed three times by redispersing in 1:1 DI water:ethanol and centrifuging at 500 RCF for 30 min. After washing, $\approx$ 2 mL of precipitate remained which was redispersed in 1:1 DI water:ethanol and allowed to settle overnight. Prior to spectroscopy measurement, the gold nanosphere coated diamond dust precipitate was drop cast onto gold coated slides for 1 hr followed by a gentle DI water rinse and blow dry.

In these spectroscopy trials, the UV and green doses were replicated at a lower intensity to allow for ≈ 20 spectra to be taken over each exposure period. The IR spectroscopy exposure system is illustrated in Figure 5.10.

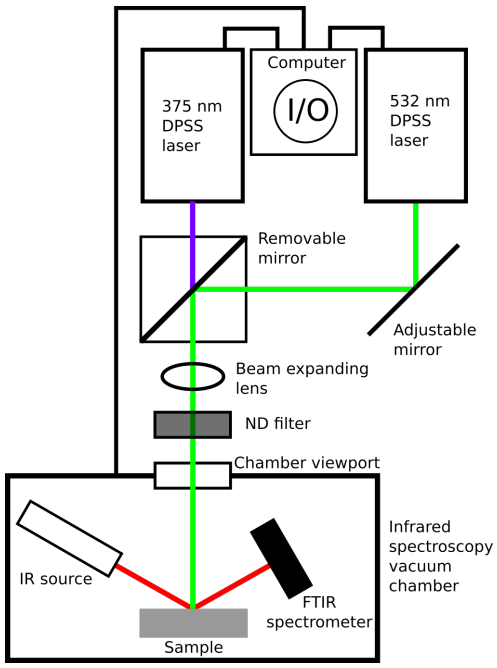

Figure 5.10: In-situ IR spectroscopy system that measures Lip3 spectra throughout photouncaging and neutralization.

The same lasers used in photolithography were remounted outside of a glass window of the vacuum spectroscopy system, again using a removable mirror to enable shared beam paths. In this case, however, fine alignment was not necessary and so only a single lens, to enlarge the spot area, and a removable filter were added to the beam path. At the sample surface, the UV laser spot diameter was 2 cm while the green spot diameter was 1.75 cm. For UV exposures of 3 $\frac{\mathrm{J}}{\mathrm{cm}^3}$ over 20 min, the filter was removed and the laser output power was set to 17 mW. To get a 2 $\frac{\mathrm{J}}{\mathrm{cm}^3}$ green dose over a 20 min exposure, the neutral density 0.6 filter was installed and the laser output power was set to 16 mW. Samples were first measured in absence of light to establish a background, followed by green, UV, and green exposures in that order.

5.4 Patterning and Spectroscopy Results

5.4.1 Patterning Results

To demonstrate that the deactivation effect was plasmonic in nature, lithographically defined Virginia Tech ”VT” logo patterns were exposed with UV light and centered on the interface areas between silver films and Tollens surfaces and UV exposed. Next, an open rectangular pattern was aligned such that the bottom half of the ”VT” was exposed to green light while the top half was not (see Figure 5.6 (g)). After incubation with gold nanospheres, the samples were analyzed by SEM and XPS in a mapping mode to produce images of gold patterned areas contrasted against the non-gold substrate. The expected result of this patterning (Figure 5.6 (h)) was based on anticipated plasmonic enhancement in the Tollens nanospheroid film areas and lack of plasmonic enhancement in the continuous film areas.

In the continuous silver film areas that had been exposed to UV, no significant difference in gold nanosphere adsorption rates was expected between the green exposed and non-green exposed areas, as no plasmonic enhancement should occur in the continuous silver films. In the nanospheroid film areas that had been exposed to UV, high adsorption rates were expected in the areas without green light exposure while low adsorption rates were expected in the green exposed areas. In regions off of beam-center, lower green light dosages were expected to result in higher adsorption rates in green exposed Tollens areas than in the respective beam-center regions. Fewer plasmons were expected to be excited in lower intensity regions and consequently a reduction in the nullification effect was expected. The results, as illustrated in Figure 5.11, were unexpected though found to be repeatable across multiple samples.

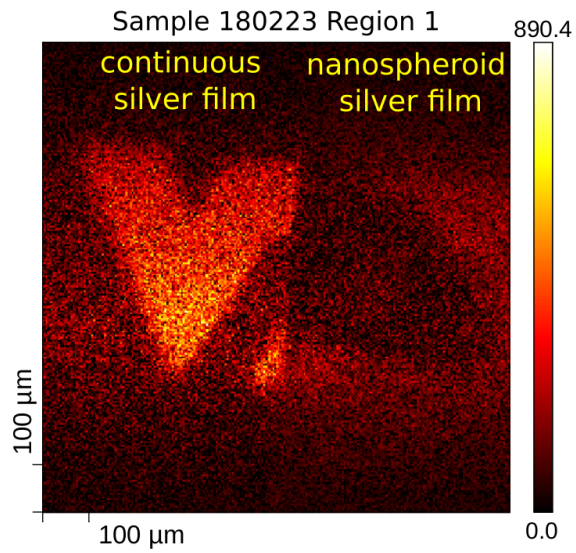

(a) XPS gold density map of beam center (Region 1) exposure area.

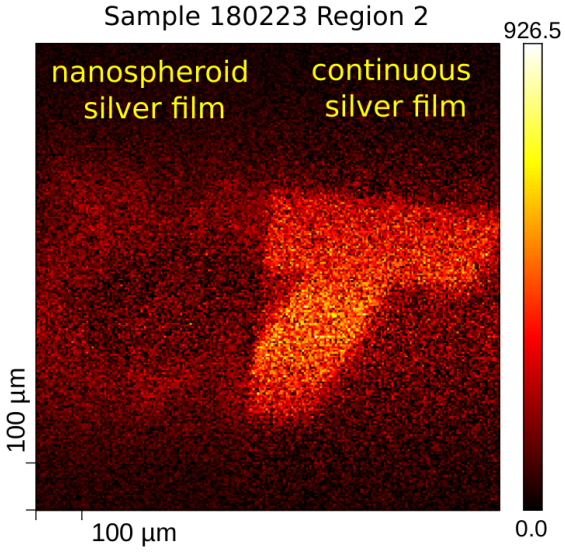

(b) XPS gold density map of off beam center (Region 2) exposure area.

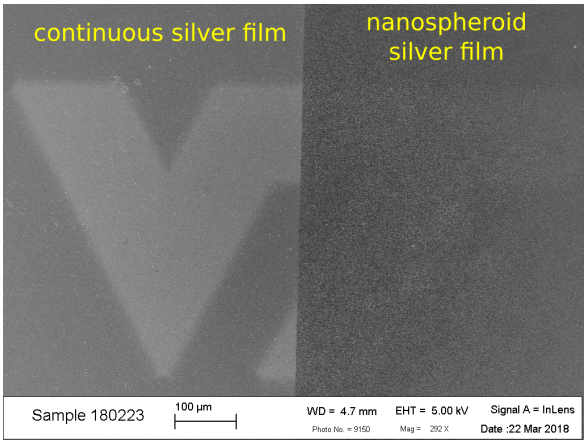

(c) SEM micrograph of beam center exposure (Region 1) area.

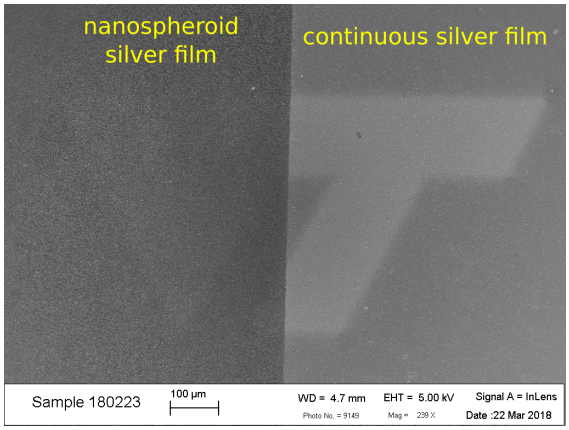

(d) SEM micrograph of off beam center exposure (Region 2) area.

Figure 5.11: Reverse patterned gold nanospheres on on silver surfaces by a photocleavable ligand. Two locations on a single sample, beam center exposure area: Region 1 (a) and (c) versus off-beam center exposure area: Region 2 (b) and (d).

In the case of the Figure 5.11 sample, the UV and green beam spots were centered on silver film/Tollens intersection line of Region 1, while the Region 2 line lies 2.5 mm off of the beam centers, consequently receiving smaller doses. In Region 1, the ”T” on Tollens surface is all but invisible while the ”V” on the Tollens surface of Region 2 is faint but visible. Further, there is

no clear distinction between the top and bottom halves in either region despite that the only the bottom halves having been exposed to green light. The significance of this is that the effect which deactivates the photocleaved functional group is dependent on the green light dose but does not appear to require direct light exposure and has no effect on the silver film substrate regions.

The deactivation effect is not the sole cause of discrepancy of adsorption rates between the continuous silver film and silver nanospheroid film regions, as the two regions intrinsically have different binding site availability. The silver nanospheroid film produced by the Tollens method did not yield a continuous film of nanosphereoids, but rather a layer of discrete silver nanospheroids. Gold nanospheres will not adsorb in the gaps between silver nanospheroids so a lower density of gold nanospheres is to be expected in these regions. High magnification electron micrographs of the above sample illustrate this in Figure 5.12.

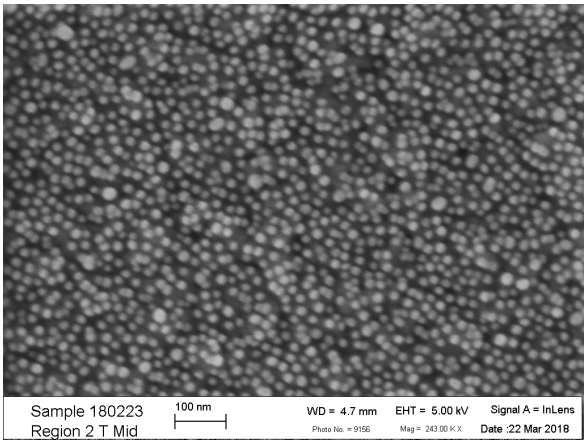

(a) Center of patterned T area of Region 2, continuous silver film area.

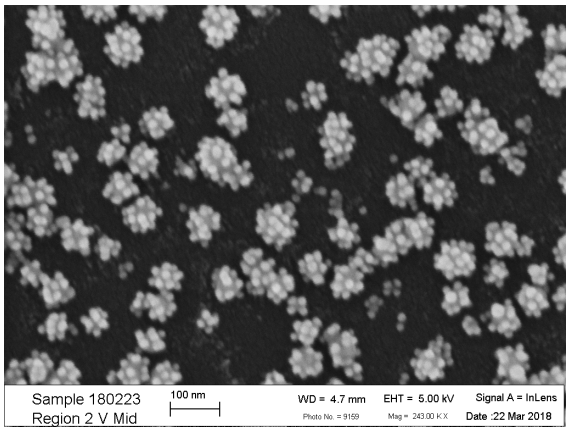

(b) Center of patterned V area of Region 2, nanospheroid film area.

Figure 5.12: Higher magnification electron micrographs demonstrating differences of binding site availability between continuous silver film and silver nanospheroid film areas. The smaller spheres are gold nanospheres adsorbed onto the silver.

Different exposure conditions as well as silver nanospheroid average sizes were tried out over the course of the work. The absorption peak of green light in silver nanospheroids is size dependent, red shifting with increasing nanospheroid diameter. Different silver nanospheroid diameter films

were consequently expected to yield different green light negation efficiencies. To test this, different silver nanospheroid diameter films were exposed to varying green light dosages and gold nanospheroid adsorption rates were compared. Over all sample exposure conditions, more gold nanosphere adsorption was observed in regions with lower green light exposure. Further, exposing the Lip3 conjugated films to green light prior to UV photouncaging resulted in deactivation of incidentally cleaved groups. Consequently, pre-exposing samples with green light was expected to effectively increase the lithographic quality of the method while decreasing the over all number of adsorbed gold nanospheres. Typically, green light pre-exposure resulted in an ≈ 50 % reduction in gold nanospheres adsorbed to silver nanospheres in regions that were not exposed to UV.

It is difficult to determine the total binding site availability from SEM analysis in the Tollens regions as the nanospheroids are not of uniform shape and their form is obscured by adsorbed gold nanospheres. To quantify the deactivation effect, it is consequently more illuminating to compare the gold nanosphere adsorption rates per silver nanospheroid in the Tollens surface areas rather than adsorption rates between silver film and Tollens surface areas. A central assumption of comparing adsorption rates per silver nanospheroid between different regions is that the average silver nanospheroid area per total image area, and consequent binding site availability, should remain constant for sufficiently large numbers of silver nanospheroids. SEM imaging and analysis of the silver nanospheroid areas verified this assumption, though the average silver nanospheroid size varied across separate samples as the Tollens method does not enable fine control over nanospheroid size when repeated. In the case of the results presented here, a single SEM image at 243kX magnification showed typically 50 to 90 silver nanospheroids an area of $\approx 0.26\ \mu\mathrm{m}^2$. ImageJ, an image processing program, was used to aid in manual gold nanosphere and silver nanospheroid counting as well as area determination from the SEM images. In order to obtain reasonable statistics on gold nanosphere adsorption rates, manual counting was performed over six such SEM images for each exposure region. No significant difference in gold nanosphere adsorption rates were found in UV

exposed areas that were exposed directly to green light and those that were shielded from direct green exposure (see Figure 5.6 (i)). This observation was unanticipated and is not easily explained. One possible explanation of this effect is that some green light could have reflected off of the sample mount and exposed the shielded regions. However, the sample mount was black and any green reflection would yield a very small dosage compared to the directly exposed ares. The results of SEM imaging analysis comparing gold nanosphere adsorption rates in silver nanospheroid regions under different silver nanospheroid size and exposure conditions are presented in Table 5.1.

Sample	Average AgNSD ≈ Diameter (nm)	Exposure Doses ($\frac{J}{cm^2}$)			AuNS Adsorbed per AgNSD	
		Initial Green	Uncaging UV	Negating Green	Region 1	Region 2
180223	55	0.0	3.0	2.0	8.7±0.6	10.0±0.6
180330	49	4.0	3.0	2.0	7.4±0.3	8.1±0.4
180423	43	4.0	3.0	4.0	6.0±0.4	6.3±0.3

Table 5.1: Gold nanosphere (AuNS) adsorption rates on silver nanospheroids (AgNSD) in beam center exposure areas (Region 1) and off beam center exposure areas (Region 2) with different exposure conditions and AgNSD sizes.

The primary conclusion of Table 5.1 is that higher gold nanosphere adsorption rates occurred in previously UV patterned areas which were off of beam center areas in all exposure and silver nanospheroid size conditions. This supports the XPS mapping and visual comparison of Figure 5.11 in that the deactivation effect is dependent on green exposure dose. However, the sample with the greatest negation green dose (180423) showed the smallest difference in gold nanosphere adsorption rates, indicating that this effect saturates at sufficently high light dose. The smaller adsorption rate difference is likely compounded by the smaller silver nanosphere size in this sample, as green light is absorbed less efficiently in smaller nanospheroids.

5.4.2 Spectroscopy Results

IR spectroscopy measurements were performed simultaneously during light exposures to determine if the green light effect was altering the chemical structure of the uncaged gold nanosphere receptor groups. Prior to light exposures, the sample was measured in darkness to provide a baseline for comparison with exposure trials. A pre-exposure sample spectrum of Lip3-conjugated gold nanospheres on diamond dust is shown in Figure 5.13.

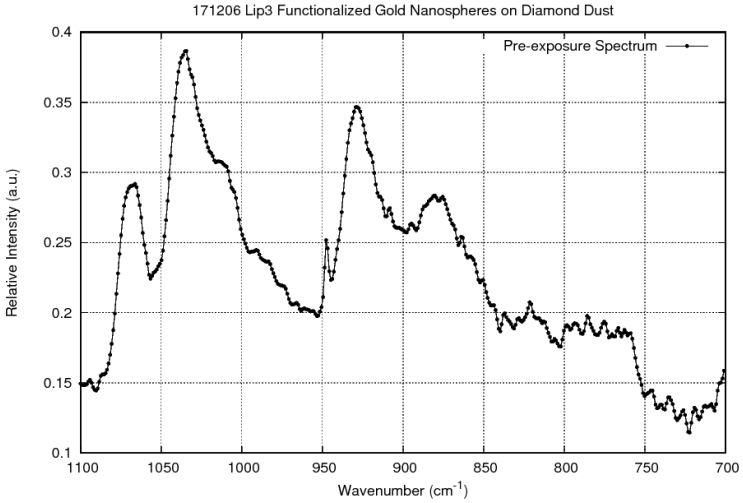

Figure 5.13: Pre-exposure spectrum of Lip3 conjugated gold nanospheres on diamond dust.

Following the unexposed spectrum measurement, the sample was exposed to green light, followed by UV, and then followed by green again as outlined in the methods section above. The initial green light exposure was expected to neutralize the few groups that were photocleaved by happenstance during the production process, the UV exposure photocleaved the vast majority of uncaged Lip3, and then the final green exposure neutralized the cleaved Lip3 groups. Direct comparison of spectra throughout the exposure periods are difficult as the traces naturally evolve over time as the ambient water content in the spectroscopy chamber condenses on the chilled detector. Further, the changes to the spectra resulting from photocleaving are relatively small compared to the baseline, so a difference measurement demonstrates the effects more clearly. In the difference measurement,

the logarithmic ratio of the initial spectrum measurements for each wavelength ($I_0(\lambda)$) and spectrum measurements at the end of the exposure ($I_f(\lambda)$) are plotted as $-\log_{10}(\frac{I_f(\lambda)}{I_0(\lambda)})$. Figure 5.14 plot results from the difference measurement, with arbitrary offsetting to separate the traces, as performed on the same sample as in Figure 5.13.

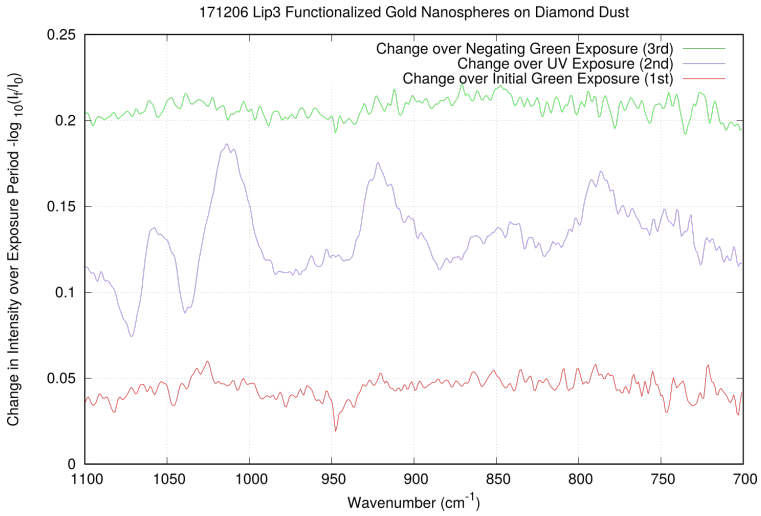

Figure 5.14: Change over exposure spectra of Lip3 conjugated gold nanospheres on diamond dust.

As Figure 5.14 illustrates, the photouncaging and revealing of gold nanosphere receptor groups resulting UV exposure is clearly visible, while green light exposures yielded no remarkable change. Additional control measurements of Lip3 conjugated directly to gold films yielded the same result, though no plasmonic enhancement was anticipated to occur in that case. Consequently, IR spectroscopy measurements yielded little insight into this effect, though it implies that ambient atmospheric conditions, presumably making oxygen and/or water available, may be required in order for the effect to occur.

5.4.3 Conclusion

Though ultimately the mechanism behind gold nanosphere adsorption inhibition remains elusive, this work has revealed some additional interesting properties of the process. Experiments were

performed on varying silver nanospheroid sizes and light exposure conditions, which were then measured by XPS mapping and SEM imaging. Gold nanosphere adsorption rates were found to be decrease with increasing green light dosage, though a saturation of the effect can occur beyond which further adsorption inhibition is limited. Decreasing silver nanospheroid size was also found to correlate with decreasing gold nanospheroid adsorption rates. This supports the idea that plasmonic enhancement is behind the effect, as smaller sliver nanospheroids were expected to have smaller plasmonic enhancement at the green wavelength used. Also supporting this idea is that no negation was observed on continuous silver films, where no plasmonic enhancement occurs.

In-situ IR spectroscopy measurements were performed on gold nanospheres conjugated with Lip3 over UV and green exposures. The photouncaging of Lip3 was clearly observed over the UV exposure, but green light exposures produced no observable change. One possible explanation for the effect was that green light exposure promoted interlinking between Lip3 functional groups, or substrate bonding. However, from the IR spectroscopy studies we may conclude that the green light exposure either does not alter the functional Lip3 group or else requires the presence of oxygen or humidity to do so. Perhaps the most intriguing property of this process is that direct light exposure was not necessary to inhibit adsorption, though higher green light doses inhibited adsorption more so than lower doses up to a saturation point. To better understand the green light negation effect and to refine it into a reliable image reversal process, additional characterization efforts are needed. Exploration of atmospheric effects as well as variations in silver nanospheroid size would likely yield a better understanding of this process.

References

[1] Hilaal Alam and Seeram Ramakrishna. A review on the enhancement of figure of merit from bulk to nano-thermoelectric materials. *Nano Energy*, 2:190–212, 2013.

[2] E. Altenkirch. Uber den nutzeffekt der thermos äulen. *Physikalische Zeitschrift*, 10:560–580, 1909.

[3] E. Altenkirch. Elektrothermische kälteerzeugung und re versible elektrische heizung. *Physikalische Zeitschrift*, 12:920–924, 1911.

[4] H.A. Atwater and A. Polman. Plasmonics for improved photovoltaic devices. *Nature Materials*, 9:205–213, 2010.

[5] Martin Barzelay, Kin Nee Tong, and George Holloway. Effects of pressure on thermal conductance of contact joints technical report. *National Advisory Committee for Aeronautics*, 3295, 1955.

[6] Marcus Bäumer and Hans-Joachim Freund. Metal deposits on well-ordered oxide films. *Progress in Surface Science*, 61:127–198, 1999.

[7] M.I.J. Beale, J.D. Benjamin, M.J. Uren, N.G. Chew, and A.G. Cullis. An experimental and theoretical study of the formation and microstructure of porous silicon. *Journal of Crystal Growth*, 73:622–636, 1985.

[8] O. Bisi, S. Osscini, and L. Pavesi. Porous silicon: a quantum sponge structure for silicon based optoelectronics. *Surface Science Reports*, 38:1–126, 2000.

[9] A. Boyer and E. Cisse. Properties of thin film thermoelectric materials: application to sensors using the seebeck effect. *Materials Science and Engineering: B*, 13:103–111, 1992.

[10] M.L. Brongersma, N.J. Halas, and P. Nordlander. Plasmon-induced hot carrier science and technology. *Nature Nanotechnology*, 10:25–34, 2015.

[11] A.M. Brown, R. Sundararaman, P. Narang, W.A. Goddard, and H. A. Atwater. Nonradiative plasmon decay and hot carrier dynamics: Effects of phonons, surfaces, and geometry. *American Chemical Society Nano*, 10:957–966, 2016.

[12] Edited by D.M. Rowe. Crc handbook of thermoelectrics. CRC Press, Boca Raton, FL, 1994.

[13] Edited by L. Canham. Handbook of porous silicon. Springer International Publishing, Zug, Switzerland, 2014.

[14] David Cahill. Thermal conductivity measurement from 30 to 750 k: the 3ω method. *Review of Scientific Instruments*, 61:802–808, 1990.

[15] David Cahill. Analysis of heat flow in layered structures for time-domain thermoreflectance. *Review of Scientific Instruments*, 75:5119–5122, 2004.

[16] David Cahill, Kenneth Goodson, and Arunava Majumdar. Thermometry and thermal transport in micro/nanoscale solid-state devices and structures. *Journal of Heat Transfer*, 124: 223–241, 2001.

[17] David Cahill, Wayne Ford, Kenneth Goodson, Gerald Mahan, Arun Majumdar, Humphrey Maris, Roberto Merlin, and Simon Phillpot. Nanoscale thermal transport. *Journal of Applied Physics*, 93:793–818, 2003.

[18] David Cahill, Paul Braun, Gang Chen, David Clarke, Shanhui Fan, Kenneth Goodson, Pawel Keblinski, William King, Gerald Mahan, Arun Majumdar, Humphrey Maris, Simon Phillpot, Eric Pop, and Li Shi. Nanoscale thermal transport. II. 2003-2012. *Applied Physics Reviews*, 1:011305, 2014.

[19] L.T. Canham. Silicon quantum wire array fabrication by electrochemical and chemical dissolution of wafers. *Applied Physics Letters*, 57:1046–1048, 1990.

[20] C. W. Chang, D. Okawa, H. Garcia, A. Majumdar, and A. Zettl. Breakdown of Fourier's law in nanotube thermal conductors. *Physical Review Letters*, 101:075903, 2008.

[21] C.W. Chang et al. Solid-state thermal rectifier. *Science*, 314:1121–1124, 2006.

[22] Gang Chen. Particularities of heat conduction in nanostructures. *Journal of Nanoparticle Research*, 2:199–204, 2000.

[23] H.-Y. Chiu et al. Ballistic phonon thermal transport in multiwalled carbon nanotubes. *Physical Review Letters*, 95:226101–1–226101–4, 2005.

[24] Jae Dong Chung and Massoud Kaviany. Effects of phonon pore scattering and pore randomness on effective conductivity of porous silicon. *International Journal of Heat and Mass Transfer*, 43:521–538, 2000.

[25] Ruxandra Costescu, Marcel Wall, and David Cahill. Thermal conductance of epitaxial interfaces. *Physical Review B*, 67:054302, 2003.

[26] Chalongrat Daengngam. *Second-Order Nonlinear Optical Responses in Tapered Optical Fibers with Self-Assembled Organic Multilayers*. PhD thesis, Virginia Polytechnic Institute and State University, 2012.

[27] Francis DiSalvo. Thermoelectric cooling and power generation. *Science*, 285:703–706, 1999.

[28] Rowe D.M. Crc handbook of thermoelectrics, chapter 35, miniature semiconductor thermoelectric devices. CRC Press, Boca Raton, FL, 1994.

[29] M.S. Dresselhaus. New directions for low-dimensional thermoelectric materials. *Advanced Materials*, 19:1043–1053, 2007.

[30] M.J. Eddowes. Anodic dissolution of p- and n-type silicon: Kinetic study of the chemical mechanism. *Journal of Electroanalytical Chemistry and Interfacial Electrochemistry*, 280: 297–311, 1990.

[31] V.E. Ferry, M.A. Verschuuren, H.B.T. Li, R.E.I. Schropp, H.A. Atwater, and A. Polman. Improved red-response in thin film a-si:h solar cells with soft-imprinted plasmonic back reflectors. *Applied Physics Letters*, 95:183503, 2009.

[32] M. Fleischmann, P.J. Hendra, and A.J. McQuillan. Raman spectra of pyridine adsorbed at a silver electrode. *Chemical Physics Letters*, 26:163–166, 1974.

[33] H. Föll, M. Chrisophersen, J. Cartensen, and G. Hasse. Formation and application of porous silicon. *Materials Science and Engineering: R: Reports*, 39:93–141, 2002.

[34] J. B. J. Fourier. *Théorie Analytique de la Chaleur*. F. Didot, 1822.

[35] G. Frens. Controlled nucleation for the regulation of the particle size in monodisperse gold suspensions. *Nature Physical Science*, 241:20–22, 1973.

[36] Casati G. et al. Increasing thermoelectric efficiency: A dynamical systems approach. *Physical Review Letters*, 101:016601, 2008.

[37] Zhenbin Ge, David Cahill, and Paul Braun. Thermal conductance of hydrophilic and hydrophobic interfaces. *Physical Review Letters*, 96:186101, 2006.

[38] S. George. Atomic layer deposition: An overview. *Chemical Reviews*, 110:111–131, 2010.

[39] F. Giazotto and F.S. Bergeret. Thermal rectification of electrons in hybrid normal metal-superconductor nanojunctions. *Applied Physics Letters*, 103:242602–1–242602–5, 2013.

[40] K. Gloos, C. Mitschka, F. Pobell, and P. Smeibidi. Thermal conductivity of normal and superconducting metals. *Cryogenics*, 30:14–18, 1990.

[41] B. Gregory and J. Stickney. Electrochemical atomic layer epitaxy (ECALE). *Journal of Electroanalytical Chemistry*, 300:543–561, 1991.

[42] James A. Harrington, Don A. Gregory, and William F. Otto. Infrared absorption in chemical laser window materials. *Applied Optics*, 15:1953–1959, 1976.

[43] W.M. Haynes. *CRC Handbook of Chemistry and Physics*. CRC Press, Boca Raton, FL, 2016.

[44] L.D. Hicks and M.S. Dresselhaus. Thermoelectric figure of merit of a one-dimensional conductor. *Physical Review B*, 47:631–634, 1993.

[45] L.D. Hicks and M.S. Dresselhaus. Effect of quantum-well structures on thermoelectric figure of merit. *Physical Review B*, 47:727–731, 1993.

[46] L.D. Hicks and M.S. Dresselhaus. Experimental study of quantum-well structures on the thermoelectric figure of merit. *Physical Review B*, 53:493–496, 1996.

[47] L.D. Hicks, T.C. Harman, and M.S. Dresselhaus. Use of quantum well superlattices to obtain a high figure of merit from nonconventional thermoelectric materials. *Applied Physics Letters*, 63:3231–3230, 1993.

[48] Thomas P. Seward III. *High temperature glass melt property database for process modeling*. The American Ceramic Society, Westerville, OH, 2005.

[49] Abram Fedorovich Ioffe. Semiconductors in the modern physics. Publishing House of the Academy of Sciences USSR, Moscow-Leningrad, 1954.

[50] A.F. Ioffe and others. On an increasing of efficiency of semiconductor thermocouples. *The Reports of Academy of Sciences USSR*, 106:981, 1956.

[51] P. Jain, K. Lee, I. El-Sayed, and M. El-Sayed. Calculated absorption and scattering properties of gold nanoparticles of different size, shape, and composition: Applications in biological imaging and biomedicine. *The Journal of Physical Chemistry B*, 110:7238–7248, 2006.

[52] L.P.B.M. Janssen and M.M.C.G. Warmoeskerken. *Transport phenomena data companion*. Leeghwaterstraat, Delft, The Netherlands, 2006.

[53] Chih-Yu Jao. *Sensing applications of gold and silver nanoparticles*. PhD thesis, Virginia Polytechnic Institute and State University, 2012.

[54] A. Jezowski and J. Rafalowicz. Heat flow asymmetry on a junction of quartz with graphite. *Physica Status Solidi A*, 47:229–232, 1978.

[55] M.J. Kale, T. Avanesian, and P. Christopher. Direct photocatalysis by plasmonic nanostructures. *American Chemical Society Catalysis*, 4:116–128, 2014.

[56] E.-K. Kim, S.-I. Kwun, S.-M. Lee, H. Seo, and J.-G. Yoon. Thermal boundary resistance at $ge_2sb_2te_5$/zns:sio_2 interface. *Applied Physics Letters*, 76:3864–3866, 2000.

[57] J. H. Kim, D. Seong, G. H. Ihm, and C. Rhee. Measurement of thermal conductivity of si and gaas wafers using the photothermal displacement technique. *International Journal of Thermophysics*, 19:281–290, 1998.

[58] S. Kim, Z. Gibbs, Y. Tang, H. Wang, and G. J. Snyder. Characterization of lorenz number with seebeck coefficient measurement. *APL Materials*, 3:041506, 2015.

[59] K. Kneipp, H. Kneipp, I. Itzan, R. Dasari, and M. Feld. Surface-enhanced raman scattering and biophysics. *Journal of Physics: Condensed Matter*, 14:R597–R624, 2002.

[60] Yee Kan Koh, Suzanne Singer, Woochul Kim, Joshua Zide, Hong Lu, David Cahill, Arun Majumdar, and Arthur Gossard. Comparison of the 3 ω method and time-domain thermoreflectance for measurements of the cross-plane thermal conductivity of epitaxial semiconductors. *Journal of Applied Physics*, 105:05303, 2009.

[61] E. Kretschmann. Die bestimmung optischer konstanten von metallen durch anregung von oberflächenplasmaschwingungen. *Zeitschrift für Physik*, 241:313–324, 1971.

[62] G. Landsberg and L. Mandelstam. A novel effect of light scattering in crystals. *Naturwissenschaften*, 16:577, 1928.

[63] Daniel Langley, G. Giusti, C. Mayousse, C. Celle, D. Bellet, and JP Simonato. Flexible transparent conductive materials based on silver nanowire networks: a review. *Nanotechnology*, 24:452001, 2013.

[64] S. Lee et al. Anomalously low electronic thermal conductivity in metallic vanadium dioxide. *Science*, 335:371–374, 2017.

[65] V. Lehmann and H. Föll. Formation mechanism and properties of electrochemically etched trenches in n-type silicon. *Journal of The Electrochemical Society*, 137:653–659, 1990.

[66] V. Lehmann and U. Gosele. Porous silicon formation: A quantum wire effect. *Applied Physics Letters*, 58:856–858, 1991.

[67] V. Lehmann, R. Stengl, and A. Luigart. On the morphology and the electrochemical formation mechanism of mesoporous silicon. *Materials Science and Engineering B*, 11:69–70, 2000.

[68] F. Lepoutre, D. Balageas, Ph. Forge, S. Hirschi, J. L. Jouland, D. Rochais, and F. C. Chen. Micron-scale thermal characterizations of interfaces parallel or perpendicular to the surface. *Journal of Applied Physics*, 78:2208–2223, 1995.

[69] Bincheng Li, J. P. Roger, L. Pottier, and D. Fournier. Complete thermal characterization of film-on-substrate system by modulated thermoreflectance microscopy and multiparameter fitting. *Journal of Applied Physics*, 86:5314–5316, 1999.

[70] Jing-Feng Li et al. High-performance nanostructured thermoelectric materials. *NPG Asia Materials*, 2:152–158, 2010.

[71] S. Link and M.A. El-Sayed. Spectral properties and relaxation dynamics of surface plasmon electronic oscillations in gold and silver nanodots and nanorods. *Journal of Physical Chemistry B*, 103:8410–8426, 1999.

[72] L. Lu, W. Y., and D. L. Zhang. A 3 omega method for specific heat and thermal conductivity measurements. *Review of Scientific Instruments*, 72:2996–3003, 2001.

[73] Ho-Ki Lyeo and David Cahill. Thermal conductance of interfaces between highly dissimilar materials. *Physical Review B*, 73:144301, 2006.

[74] S.A. Maier and H.A. Atwater. Plasmonics: Localization and guiding of electromagnetic energy in metal/dielectric structures. *Journal of Applied Physics*, 98:011101, 2005.

[75] Stefan A. Maier. Plasmonics: Fundamentals and applications. Springer US, New York, NY, 2007.

[76] Arum Majumdar. Role of electron-phonon coupling in thermal conductance of metal-nonmetal interfaces. *Applied Physics Letters*, 84:4768–4770, 2004.

[77] R. R. Mammei. *Thin Films for the Transport of Polarized Ultracold Neutrons for Fundamental Symmetry Study*. PhD thesis, Virginia Polytechnic Institute and State University, 2010.

[78] Amy Marconnet et al. From the casimir limit to phononic crystals: 20 years of phonon transport studies using silicon-on-insulator technology. *Journal of Heat Transfer*, 135:061601–1–061601–10, 2013.

[79] J. Marie, R. Anufriev, and M. Nomura. Ballistic thermal transport in silicon nanowires. *Science Reports*, 7:41794, 2017.

[80] Maria Jose Martinez-Perez, Antonio Fornieri, and Francesco Giazotto. Rectification of electronic heat current by a hybrid thermal diode. *Nature*, 10:303–307, 2014.

[81] M.J. Martinez-Perez and F. Giazotto. Efficient phase-tunable josephson thermal rectifier. *Applied Physics Letters*, 102:182602–1–182602–5, 2013.

[82] Cz. Marucha, J. Mucha, and J. Rafalowicz. Heat flow rectification in inhomogeneous gaas. *Physica Status Solidi A*, 31:269–273, 1975.

[83] A. Melikyan, L. Alloatti, A. Muslija, D. Hillerkuss, P. C. Schindler, J. Li, R. Palmer, D. Korn, S. Muehlbrandt, D. Van Thourhout, B. Chen, R. Dinu, M. Sommer, C. Koos, M. Kohl, W. Freude, and J. Leuthold. High-speed plasmonic phase modulators. *Nature Photonics Letters*, pages 1–5, 2014.

[84] Gustav Mie. Beiträge zur optik trüber medien, speziell kolloidaler metallösungen. *Annalen der Physik*, 330:377–445, 1908.

[85] A. J. Minnich, M. S. Dresselhaus, Z. F. Ren, and G. Chen. Bulk nanostructured thermoelectric materials: current research and future prospects. *Energy and Environmental Science*, 2: 466–479, 2009.

[86] David Monk and David Soane. A review of the chemical reaction mechanism and kinetics for hydrofluoric acid etching of silicon dioxide for surface micromachining applications. *Thin Solid Films*, 232:1–12, 1993.

[87] Michael Morgen, E. Todd Ryan, Jie-Hua Zhao, Chuan Hu, Taiheui Cho, and Paul S. Ho. Low dielectric constant materials for ulsi interconnects. *Annual Review of Materials Science*, 30:645–680, 2000.

[88] W. Namura, M. Ohtsu, and T. Yatsui. Nanodot coupler with a surface plasmon polariton condenser for optical far/near-field conversion. *Applied Physics Letters*, 86:181108, 2005.

[89] S. Nie and S. Emory. Probing single molecules and single nanoparticles by surface-enhanced raman scattering. *Science*, 21:1102–1106, 1997.

[90] G. Nolas, G. Slack, and S. Schujman. Semiconductor clathrates: A phonon-glass electron-crystal material with potential for thermoelectric applications. *Semiconductors and semimetals*, 69:255–300, 2000.

[91] G.S. Nolas et al. Skutterudites: A phonon-glass-electron crystal approach to advanced thermoelectric energy conversion applications. *Annu. Rev. Mater. Sci.*, 28:89–116, 1999.

[92] Marjorie Olmstead and Nabil Amer. A new probe of optical properties of surfaces. *Journal of Vacuum Science & Technology B*, 1:751–755, 1983.

[93] Jon Opsal, Allen Rosencwaig, and David Willenborg. Thermal-wave detection and thin-film thickness measurements with laser beam deflection. *Journal of Applied Optics*, 22: 3169–3176, 1983.

[94] A. Otto. Excitation of nonradiative surface plasma waves in silver by the method of frustrated total reflection. *Zeitschrift für Physik*, 216:398–410, 1968.

[95] E. Ozbay. Plasmonics: Merging photonics and electronics at nanoscale dimensions. *Science*, 311:189–193, 2006.

[96] Carolyn Paddock and Gary Eesley. Transient thermoreflectance from thin metal films. *Journal of Applied Physics*, 60:285–290, 1986.

[97] Y. Pei and Y. Liu. Electrical and thermal transport properties of pb-based chalcogenides: Pbte, pbse, and pbs. *Journal of Alloys and Compounds*, 514:40–44, 2012.

[98] J.C. Peltier. Nouvelles expériences sur la caloricité des courants électrique. *Annales de Chimie et de Physique*, 56:371–386, 1834.

[99] Paothep Pichanusakorn and Prabhakar Bandaru. Nanostructured thermoelectrics. *Materials Science and Engineering R*, 67:19–63, 2010.

[100] D. Pines and D. Bohm. A collective description of electron interations: Ii. collective vs individual particle aspects of the interactions. *Physical Review*, 85:338–353, 1952.

[101] V. Pishchik, L. A. Lytvynov, , and E. R. Dobrovinskaya. *Sapphire Materials, Manufacturing, Applications*, pages 110–111. Springer Berlin Heidelberg, Berlin, Heidelberg, 2009. ISBN 978-0-387-85694-0.

[102] V. Pishchik, L. A. Lytvynov, , and E. R. Dobrovinskaya. *Sapphire Materials, Manufacturing, Applications*, page 170. Springer Berlin Heidelberg, Berlin, Heidelberg, 2009. ISBN 978-0-387-85695-7-2.

[103] P.Johnson and R. Christy. Optical constants of the noble metals. *Physical Review B*, 6: 4370–4379, 1972.

[104] Heinz Raether. Surface plasmons on smooth and rough surfaces and on gratings. Springer-Verlag Berlin Heidelberg, 1988.

[105] C.V. Raman and K.S. Krishnan. The optical analog of the compton effect. *Nature*, 121:711, 1928.

[106] B.P. Rand, P. Peumans, and S. R. Forrest. Long-range absorption enhancement in organic tandem thin-film solar cells containing silver nanoclusters. *Journal of Applied Physics*, 96: 7519–7526, 2004.

[107] Majid Rashidi-Huyeh and Bruno Palpant. Counterintuitive thermo-optical response of metal-dielectric nanocomposite materials as a result of local electromagnetic field enhancement. *Physical Review B*, 74:075405, 2006.

[108] Melissa Rieger and Paul Kohl. Mechanism of (111) silicon etching in hf - acetonitrile. *Journal of the Electrochemical Society*, 142:1490–1495, 1995.

[109] N.A. Roberts and D.G. Walker. Phonon lateral confinement enables thermal rectification in asymmetric single-material nanostructures. *Nano Letters*, 2011.

[110] N.A. Roberts and D.G. Walker. A review of thermal rectification observations and models in solid materials. *International Journal of Thermal Science*, 50:648–662, 2011.

[111] S. Rönnebeck, J. Carstensen, S. Otto, and H. Föll. Crystal orientation dependence of macropore growth in n-type silicon. *Electrochemical and Solid-State Letters*, 2:126–128, 1999.

[112] Allen Rosencwaig, Jon Opsal, and D. L. Willenborg. Detection of thermal waves through optical reflectance. *Applied Physics Letters*, 46:1013–1015, 1985.

[113] M. Rubin. Optical properties of soda lime silica glasses. *Solar Energy Materials*, 12:275–278, 1985.

[114] David Sands. Pulsed laser heating and melting. INTECH Open Access Publisher, 2011.

[115] D.M. Schaat, B. Feng, and E.T. Yu. Enhanced semiconductor optical absorption via surface plasmon excitation in metal nanoparticles. *Applied Physics Letters*, 86:063106, 2005.

[116] Aaron J. Schmidt, R. Cheaito, and M. Chiesa. A frequency-domain thermoreflectance method for the characterization of thermal properties. *Review of Scientific Instruments*, 80:094901, 2009.

[117] Aaron J. Schmidt, Ramez Cheaito, and Matteo Chiesa. Characterization of thin metal films via frequency-domain thermoreflectance. *Journal of Applied Physics*, 107:024908, 2010.

[118] Erich See. *Plasmon Directed Chemical Reactivity and Nanoparticle Self-Assembly*. PhD thesis, Virginia Polytechnic Institute and State University, 2017.

[119] T.J. Seebeck. Ueber die magnetische polarisation der metalle und erze durch temperatur-differenz. *Ann. Phys*, 82:130–160, 1826.

[120] Manu Shamsa, W. L. Liu, A. A. Balandin, C. Casiraghi, W. I. Milne, and A. C. Ferrari. Thermal conductivity of diamond-like carbon films. *Applied Physics Letters*, 89:161921, 2006.

[121] Subhash L. Shinde and Gyaneshwar P. Srivastava. Length-scale dependent phonon interactions. Springer US, New York, New York, 2014.

[122] G. Jeffery Snyder and Eric S. Toberer. Complex thermoelectric materials. *Nature Materials*, 7:105–114, 2008.

[123] G.J. Snyder and E.S. Toberer. Complex thermoelectric materials. *Nature Materials*, 7: 105–114, 2008.

[124] Sasha Stankovich, Dimitri Dikin, Geoffrey Dommett, Kevin Kohlhaas, Eric Zimmney, Erich Stach, Richard Piner, SonBinh Nguyen, and Rodney Ruoff. Graphene-based composite materials. *Nature*, 442:282–286, 2006.

[125] Chauncey Starr. The copper oxide rectifier. *Physics*, 7:15–19, 1936.

[126] John L. Stickney. Atomic layer deposition by electrochemistry. *The Electrochemical Society Interface*, 20:28–30, 2011.

[127] M. Terraneo, M. Peyrard, and G. Casati. Controlling the energy flow in non-linear lattices: a model for a thermal rectifier. *Physical Review Letters*, 88:4302.1–4302.4, 2002.

[128] W. Thomson. On a mechanical theory of thermoelectric currents. *Proceedings of the Royal Society of Edinburgh*, 3:91–98, 1851.

[129] Terry Tritt. *Recent trends in thermoelectric materials research, part two*, volume 70. Academic Press, 2000.

[130] Kikuo Ujihara. Reflectivities of metals at high temperatures. *Journal of Applied Physics*, 43:2376–2383, 1972.

[131] R. Vaidyanathan et al. Preliminary studies in the electrodeposition of PbSe/PbTe superlattice thin films via electrochemial atomic layer deposition (ALD). *Langmuir*, 22:10590–10595, 2006.

[132] Rama Venkatasubramanian, Edward Siivola, Thomas Colpitts, and Brooks O'Quinn. Thin-film thermoelectric devices with high room-temperature figures of merit. *Nature*, 413:597–602, 2001.

[133] Y. Wang, A. Vallabhaneni, J. Hu, B. Qiu, Y. Chen, and X. Phonon transport in asymmetric sawtooth nanowires. *ASME Conference Proceedings*, 14:592–596, 2014.

[134] Yan Wang, Ajit Vallabhaneni, Jiuning Hu, Bo Qiu, Yong P. Chen, and Xiulin Ruan. Phonon lateral confinement enables thermal rectification in asymmetric single-material nanostructures. *Nano Letters*, 14:592–596, 2014.

[135] R. J. Wells. Rapid approximation to the voigt/faddeeva function and its derivatives. *Journal of Quantitative Spectroscopy and Radiative Transfer*, 62:29–48, 1999.

[136] A. Wokaun, J.P. Gordon, and P.F. Liao. Radiation damping in surface-enhanced raman scattering. *Physical Review Letters*, 48:957, 1982.

[137] R.W. Wood. On a remarkable case of uneven distribution of light in a diffraction grating spectrum. *Proceedings of the Physical Society*, 18:269–275, 1902.

[138] P.R. Yoder, Jr. *Optomechanical Systems Design, 2nd Ed.* Marcel Dekker, New York, 1993.

[139] D. A. Young, C. Thomsen, H. T. Grahn, H. J. Maris, and J. Tauc. *Heat Flow in Glasses on a Picosecond Timescale*, pages 49–51. Springer Berlin Heidelberg, Berlin, Heidelberg, 1986. ISBN 978-3-642-82912-3. doi: 10.1007/978-3-642-82912-3.

[140] S. Zastrow et al. Thermoelectric transport and hall measurements of low defect Sb2Te3 thin films grown by atomic layer deposition. *Semiconductor Science and Technology*, 28:1–6, 2013.

[141] Jie Zhu, Dawei Tang, Wei Wang, Jun Liu, Kristopher Holub, and Ronggui Yang. Ultrafast thermoreflectance techniques for measuring thermal conductivity and interface thermal conductance of thin films. *Journal of Applied Physics*, 108:094315, 2010.